OPEN ACCESS
Functional Materials Letters
Vol. 15, Nos. 7 & 8 (2022) 2240002 (42 pages)
© The Author(s)
DOI: 10.1142/S1793604722400021

World Scientific
www.worldscientific.com

Lithium phosphosulfide electrolytes for solid-state batteries: Part II

Xin Lu[*,†,**], Chih-Long Tsai[*], Shicheng Yu[*], Hongying He[‡], Osmane Camara[*],
Hermann Tempel[*], Zigeng Liu[*], Anna Windmüller[*], Evgeny V. Alekseev[*],
Simone Köcher[*], Shibabrata Basak[*,§], Li Lu[¶], Rüdiger A. Eichel[*,†,||] and Hans Kungl[*]

[*]*Institut für Energie-und Klimaforschung (IEK-9: Grundlagen der Elektrochemie)*
Forschungszentrum Jülich, D-52425 Jülich, Germany

[†]*Institut für Materialien und Prozesse für elektrochemische Energiespeicher-und wandler*
RWTH Aachen University, D-52074 Aachen, Germany

[‡]*School of Mechanical and Aerospace Engineering, Nanyang Technological University*
Singapore 639798

[§]*Ernst Ruska-Centre for Microscopy and Spectroscopy with Electrons and*
Peter Grünberg Institute, Forschungszentrum Jülich, D-52425 Jülich, Germany

[¶]*Department of Mechanical Engineering, National University of Singapore*
Singapore 117575

[||]*Institut für Energie-und Klimaforschung (IEK-12: Helmholtz-Institute*
Münster Ionics in Energy Storage), Forschungszentrum Jülich
D-48149 Münster, Germany

[**]*x.lu@fz-juelich.de*

Received 6 September 2022; Revised 31 October 2022; Accepted 2 November 2022; Published 21 December 2022

Among the electrolytes designed for all solid-state batteries, the phosphosulfide electrolytes stand out with respect to their very high Li-ion conductivities. However, when in contact with metallic lithium anodes, there are remaining challenges to ensure long-term operation stability. Both issues, the Li-ion conductivity and the electrochemical stability vs. metallic lithium, are the subject of this review. After introducing the background for developing all solid-state Li-ion batteries with metallic lithium anode and providing a brief overview on four types of phosphosulfide electrolytes, in Part I of the review a compound treatment on the Li–P–S and the LiSICon type electrolytes had been given. Part II of the review will continue following the same schedule by discussing the chemistry, structure, processing and Li-ion conductivity of the LGPS and the Argyrodite-type phosphosulfides. Emphasis is put on the treatise of the chemistries supported by the consideration of specific phase diagrams and intra-type comparisons of the Li-ion conductivities at ambient temperature. In a summarizing section, inter-type comparisons among selected compositions of the Li–P–S type, the LiSICon-type, the LGPS-type and the Argyrodite-type phosphosulfides are addressed for the two main issues for electrolytes in all solid-state batteries, the Li-ion conductivities and the electrochemical stability vs. metallic lithium. The review is concluded with remarks on the status and the perspectives of the research on Li-ion conducting phosphosulfide electrolytes.

Keywords: Lithium sulfide; LGPS; argyrodite; sulfide electrolytes; solid-state electrolytes.

1. Introduction

Among the four types of crystalline phosphosulfide electrolytes, the Li–P–S- and the LiSICon-type materials go back to the past century.[1–5] LGPS-type and Argyrodite electrolytes are the results of recent developments, with first reports on Li-ion conducting Argyrodites dating back to 2008[6] and on LGPS in 2011.[7] The Li–P–S type electrolytes, characterized by their chemical composition exclusively containing lithium, phosphorus and sulfur encompass a wide scope of structures and anion sublattice frameworks. Among them, Li_3PS_4, $Li_{9.6}P_3S_{12}$ and Li_7PS_6 are Li–P–S archetype electrolytes of the other, LiSICon, LGPS and Argyrodite types, respectively.[8–10] Structural features and typical anionic frameworks are critical features for LiSICon-, LGPS- and Argyrodite-type

---

[**]Corresponding author.

electrolytes. Most typically, constituent components in the LiSICon and LGPS types are metals or semimetals (semi/metal in this text denotes semimetal and/or metal) and halogens in the Argyrodite-type phosphosulfides. Within each of these types, a wide scope of materials have been developed by modifying the base materials with iso– and aliovalent cations, anions other than sulfur, both along with charge compensating changes in their lithium content.[11–13] The scope for processing routes spans from preparation to the melt and solid-state routes to liquid-phase processing.[14–16]

Part I of this review presented the application background for the development of Li-ion conductive solid-state electrolytes for designing all solid-state Li-ion batteries with metallic lithium anodes and a brief overview on the four types of phosphosulfide electrolytes, the Li–P–S type, the LiSICon type, the LGPS type and the Argyrodite type. Two of them, the Li–P–S-type and the LiSICon-type electrolytes, were the subject of detailed descriptions along with the wide variety of compositions there.

Part II of this review on phosphosulfide electrolytes starts with a detailed treatment of the LGPS and the Argyrodite type, while maintaining the conceptual framework following that of Part I. According to this concept, first the chemistry of the materials in context with phase diagrams specific to these compositions are considered. Subsequently, the phosphosulfide electrolytes within both types are analyzed considering their structural characteristics, the options for the processing and compared with respect to their Li-ion conductivities at ambient temperature. A summarizing section encompasses an inter-type comparison of the Li-ion conductivities for selected Li–P–S-, LiSICon-, LGPS- and Argyrodite-type electrolytes and a treatment related to the electrochemical stability of the phosphosulfides. The latter contains sections on theory, on experimental work on electrochemical stability and interphase formation and, as a perspective, on the design of electrochemically stable artificial interlayers. Part II will be concluded with an assessment of the status and perspectives for future research on phosphosulfide electrolytes.

2. LGPS — Type Electrolyte Materials

A breakthrough in the performance of Li-ion conduction was achieved in 2011 when Kamaya *et al*. reported a superionic conductor $Li_{10}GeP_2S_{12}$ (LGPS) with an ambient temperature Li-ion conductivity of 1.2×10^{-2} S/cm.[7] The building blocks for the structure are PS_4^{3-} and GeS_4^{2-} tetrahedra, the space group of this electrolyte material is tetragonal (*P4₂/nmc*). Subsequently, the label "LGPS-type superionic conductor" was coined by the inventors for Li-conducting phosphosulfide electrolytes with this space group regardless of the semi/metal species in the composition. So far, tin and silicon have been proven to be low-cost substitutes for germanium within the LGPS-type superionic conductors.[17]

Since 2011, six lines of development (Fig. 1) for further improvement of conductivity and stability of the $Li_{10}GeP_2S_{12}$ have been pursued: (i) modifications of the stoichiometry in Ge-based electrolytes, (ii) the substitution of Ge by Sn or Si along with stoichiometry variations, (iii) the use of binary semi/metallic or metallic components, (iv) the elimination of the semi/metal component via Li–P–S materials, (v) the substitution of part of the sulfur by halogens and (vi) the partial substitution of sulfur by oxygen. While the first three aimed to achieve a high Li-ion conductivity along with sustainable educts, the main objective of the latter three approaches is to improve the electrochemical stability while maintaining a high Li-ion conductivity.

Modifications of the original $Li_{10}GeP_2S_{12}$ composition followed in particular the $Li_{10+d}Ge_{1+d}P_{2-d}S_{12}$ stoichiometry.[18,19] Maintaining a constant ratio of S:(Ge+P) of 4:1 is a precondition for an anion framework consisting exclusively of isolated PS_4^{3-} and GeS_4^{2-} tetrahedra, thus for preserving the original anionic building blocks $Li_{10}GeP_2S_{12}$ structure. The scope for the variation in d ranges from $d = 0$ to $d = 0.5$ in the $Li_{10+d}Ge_{1+d}P_{2-d}S_{12}$ solid solution series $Li_{10.35}Ge_{1.35}P_{1.65}S_{12}$ provides slightly enhanced performance compared to $Li_{10}GeP_2S_{12}$.

The substitution of germanium with less expensive materials such as tin or silicon was a precondition in order to open up the perspective for a widespread application of the LGPS-type electrolytes. Investigation of $Li_{10}SnP_2S_{12}$ as tin analogous material of the prototype LGPS electrolyte provided

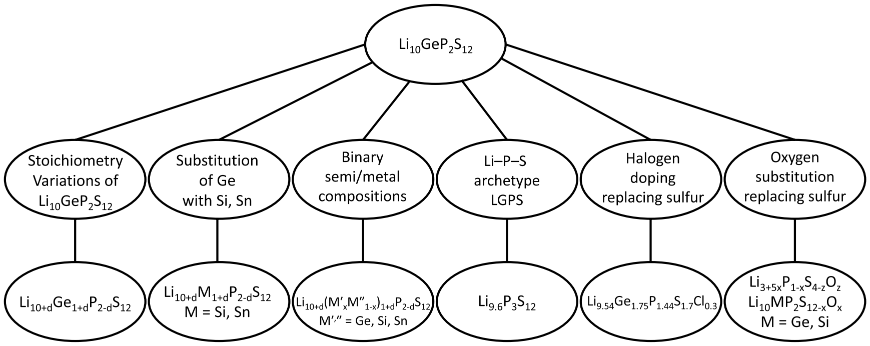

Fig. 1. Lines of development emerging from the prototype $Li_{10}GeP_2S_{12}$ electrolyte material.

a proof of concept, that an affordable Li-ion conductor using Sn as a metal component for high Li-ion conductivity might be feasible.[20] Exploring the range of solid solutions in $Li_{10+d}M_{1+d}P_{2-d}S_{12}$ stoichiometry for the Si and Sn systems provided insight, that on the one hand for Sn as well as for Si LGPS-type electrolytes with $P4_2/nmc$ symmetry were realized over a certain compositional range, on the other hand for all of them the performance was by a factor of 3–4 less than for the original $Li_{10}GeP_2S_{12}$.[21]

LGPS-type materials with binary semi/metal component by partial substitution of the Ge by Sn or Si resulted in solid solutions with space group $P4_2/nmc$ for, both, $Li_{10}(Ge_{1-x}Si_x)P_2S_{12}$ and $Li_{10}(Ge_{1-x}Sn_x)P_2S_{12}$ in the complete range $0 \le x \le 1.0$.[22] A maximum Li-ion conductivity at ambient temperature (0.86×10^{-2} S/cm) within the $Li_{10}(Ge_{1-x}Sn_x)P_2S_{12}$ series was achieved with a minor silicon content ($x = 0.05$) in $Li_{10}(Ge_{9.95}Si_{0.05})P_2S_{12}$, thus the approach did not lead to a drastic increase in sustainability. Binary compositions with Sn and Si semi/metal components $Li_{10+d}(Sn_ySi_{1-y})_{1+d}P_{2-d}S_{12}$ were largely monophasic in the composition range ($-0.1 \le d \le 0.5$ and $0 \le y \le 1$).[23] The performance of the best material in this series, $Li_{10.35}(Sn_{x0.27}Si_{1.08})P_{1.65}S_{12}$, was almost at the same level as for the original $Li_{10}GeP_2S_{12}$ thus providing a sustainable material with extremely high conductivity.

Although in the exclusively semi/metal-based LGPS, extremely high Li-ion conductivities were realized, a critical issue for application in all solid-state batteries with Li-anode is the electrochemical stability that is particularly close to the Li/Li^+ electrochemical potential. In particular, the semi/metal components Ge, Sn or Si are possibly reduced.[17] Thus, further modifications of the materials were addressed with the main objective to stabilize the LGPS-type electrolytes.

The most straightforward approach to prevent the reduction of the semi/metal is to eliminate this component from the composition. Within the Li–P–S system, lithium-doped modifications of the thio-LiSICon structured host material Li_3PS_4, in which the generation of lithium interstitials by substituting 5 Li^+ for P^{5+} according to $Li_{3+5x}P_{1-x}S_4$, had shown relatively high conductivity in particular for $Li_{3.325}P_{0.935}S_4$ ($x = 0.065$).[24] Research work on compositions in the vicinity of these materials resulted in development of $Li_{9.6}P_3S_{12}$.[9,17] This material is considered to form a stable interphase along with cycling in batteries with metallic lithium anode, however, its Li-ion conductivity is roughly an order of magnitude less than for the high performance semi/metal-based LGPS-type superionic conductors.[9] Moreover, its structure, which was considered to be $P4_2/nmc$ in 2016, is still under discussion.[9]

An alternative approach to stabilize the electrochemical stability is to substitute part of the sulfur with halogens, along with further adjustments of the stoichiometry. Specifically, chlorine was applied in the development of Si-based LGPS-type materials in this direction, which resulted in the invention of the $P4_2/nmc$ structured high Li-ion conductivity $Li_{9.54}Si_{1.74}P_{1.44}S_{11.7}Cl_{0.3}$ electrolyte.[9]

Most recent work in order to stabilize the LGPS electrolytes under battery operation conditions slanted toward partial substitution of sulfur by oxygen. Specifically, oxygen incorporation in LGPS-type electrolytes has been realized for $Li_{10}GeP_2S_{12}$ according to $Li_{10}GeP_2S_{12-x}O_x$ ($0.3 \le x \le 0.6$),[25] for silicon-based LGPS-type materials $Li_{9.42}Si_{1.02}P_{2.1}S_{9.96}O_{2.04}$,[26] as well a $Li_{10}SiP_2S_{12-x}O_x$ ($0 \le x \le 1.75$),[27] and for electrolytes from the $Li_{3+5x}P_{1-x}S_{4-z}SO_z$ ($0.03 \le x \le 0.08$, $0.4 \le z \le 0.8$) and $Li_{9+d}P_{3+d'}S_{12-k}O_k$ systems.[28,29]

2.1. *Chemistry and phase relations of LGPS-type electrolytes*

The positions of the prototype material $Li_{10}GeP_2S_{12}$ and isostructural variations thereof consisting of lithium, semi/metals like Ge, Sn or Si, phosphorus and sulfur are displayed in a ternary $Li_2S–P_2S_5–Z$ diagram with Z = GeS_2, SnS_2 or SiS_2 (Fig. 2). The prototype composition $Li_{10}GeP_2S_{12}$ contains the components Li_2S:P_2S_5:GeS_2 in 5:1:1 ratio, or normalized to $\sum c_i = 1$, the ratio of these components is given by 0.714:0.142:0.142. For most of the materials, the contents in Li_2S are between 0.7 and 0.8 while the amounts of P_2S_5 and GeS_2 range between 0.1 and 0.2.

The presence of compositions $Li_{10}GeP_2S_{12}$, Li_7GePS_8 and $Li_{3.25}Ge_{0.25}P_{0.75}S_4$ in the germanium-containing materials indicates that there is a certain range within the $P4_2/nmc$ structure type that allows for moderate changes in stoichiometry. In a notation normalized to S_{12}, $Li_{3.25}Ge_{0.25}P_{0.75}S_4$ and Li_7GePS_8 correspond to compositions $Li_{10.35}Ge_{1.35}P_{1.65}S_{12}$ and $Li_{10.5}Ge_{1.5}P_{1.5}S_{12}$, respectively. Thus, these materials can be assigned to a single compositional series $Li_{10+d}Ge_{1+d}P_{2-d}S_{12}$.[18] It originates from the approach to substitute germanium in the form of GeS_2 by phosphorus in form of ½P_2S_5 while compensating the resulting difference charge by concomitant addition of ½Li_2S, which corresponds to the dopant approach applied in the thio-LiSICon materials.[30]

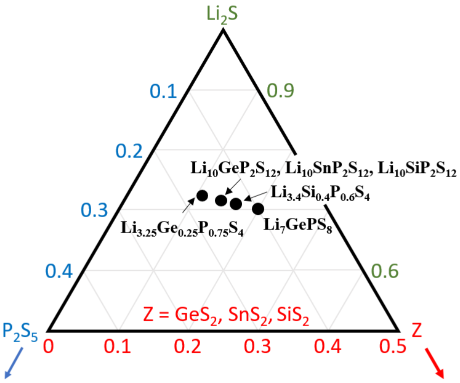

Fig. 2. LGPS-type electrolytes with in a ternary $Li_2S–P_2S_5–Z$ phase diagram with component Z = GeS_2, SiS_2 or SnS_2.

In the original reports on LGSP-type materials of this series, there are four different approaches and notations for the formal description of identical materials within this series, whereby the different notations used for the same materials reflect different aspects considering the material composition. This includes (i) a notation focusing on modifications of the prototype material $Li_{10}GeP_2S_{12}$, (ii) a notation oriented toward the historical development of thio-LiSICon, (iii) a notation that gives the structural formulae for the compositions in terms corresponding to the least common integers and (iv) a notation taking structural aspects into account is employed.

Taking the prototype material $Li_{10}GeP_2S_{12}$ as a starting point for the considerations, the d in the notation $Li_{10+d}Ge_{1+d}P_{2-d}S_{12}$ indicates in the first instance substitution between phosphorus and germanium related to the prototype $Li_{10}GeP_2S_{12}$ electrolyte. Increasing d increases Ge content and specifies, how much Ge is added along with the substitutions and compensations defining this series to the $Li_{10}GeP_2S_{12}$. In contrast, k in $Li_{4-k}M_{1-k}P_kS_4$ indicates how much phosphorus is substituted for Ge in Li_4GeS_4.

When given in explicit figures, the formulae $Li_{10+d}M_{1+d}P_{2-d}S_{12}$ vs. $Li_{4-k}M_{1-k}P_kS_4$ differs only in normalization to S_{12} or S_4 which can be easily transformed by applying a factor of 3 ($Li_{10}GeP_2S_{12}$ corresponds to $Li_{3.333}Ge_{0.333}P_{0.667}S_4$). When referring to the formal description of the materials series, however, notation as $Li_{10+d}M_{1+d}P_{2-d}S_{12}$ vs. $Li_{4-k}M_{1-k}P_kS_4$ have qualitatively inverse and quantitatively different relations concerning the parameters d and k as descriptors for the compositions. The quantitative relation between d and k is given by $k = (2 - d)/3$ or $d = 2 - 3k$.

Keeping to the notation of conventional chemistry to quantify the amounts in the structural formulae in terms of the least common integers of the constituents, some of the materials from the $Li_{10+d}Ge_{1+d}P_{2-d}S_{12}$ series, such as $Li_{10.5}Ge_{1.5}P_{1.5}S_{12}$ are described as Li_7GePS_8. A further, less widespread notation of this system is to write the formulae for the materials composition in form of $Li_{11-y}(Ge_{2-y}P_y)PS_{12}$ $(0 \leq y \leq 2)$.[31] In this approach, the formula distinguishes between phosphorus species according to their Wyckoff positions, the formal description for the Li-coefficient has to be adjusted accordingly. Actually, for $y = 1$, $Li_{10}(GeP)PS_{12}$ corresponds to $Li_{10}GeP_2S_{12}$, while for $x = 0.5$ $Li_{10.5}(Ge_{1.5}P_{0.5})PS_{12}$ describes the $Li_{10.5}Ge_{1.5}P_{1.5}S_{12}$ ($= Li_{3.5}Ge_{0.5}P_{0.5}S_{12} = Li_7GePS_8$) composition.

2.1.1. *Ge-based LGPS stoichiometry variations*

Introducing Li_3PS_4 and Li_4GeS_4 into the ternary Li_2S–P_2S_5–GeS_2 phase diagram (Fig. 3) demonstrates that the prototype material $Li_{10}GeP_2S_{12}$ as well as the complete series $Li_{10+d}Ge_{1+d}P_{2-d}S_{12}$ lie on the tie line between these compounds.

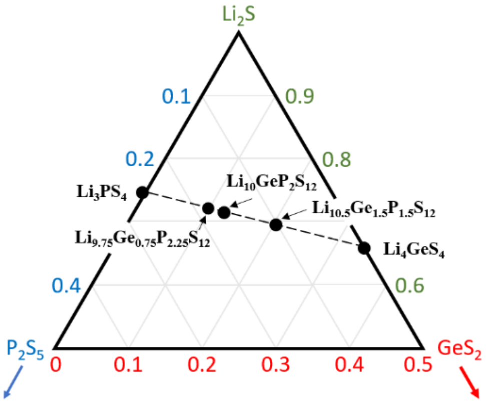

Fig. 3. Position of the $Li_{10}GeP_2S_{12}$ (LGPS) electrolyte and the $Li_{10+d}Ge_{1+d}P_{2-d}S_{12}$ series in the ternary phase diagram Li_2S–P_2S_5–GeS_2.

Along this Li_4GeS_4–Li_3PS_4 tie line, the binary phase diagram was investigated in a temperature range up to 900°C.[19] The solidus line decreases from 840°C on the Li_4GeS_4 side to 650°C and further to 570°C toward the Li_4GeS_4 and the Li_3PS_4 side of the $Li_{10}GeP_2S_{12}$ single-phase region, respectively. For higher content of Li_3PS_4, it stabilizes up to $k = 0.05$. For temperatures below 600°C, there are three single-phase regions that extend for Li_4GeS_4 (β') from $k = 0.0$ to 0.2, for $Li_{10}GeP_2S_{12}$ (G) from $k = 0.45$ to 0.6 Li_3PS_4, while for Li_3PS_4 (β), there is an almost vanishing range of solid solution. While the structures of both components Li_4GeS_4 (β') and Li_3PS_4 (β) are the same (*Pnma*), the structure of $Li_{10}GeP_2S_{12}$ (G) ($P4_2/nmc$) is completely different from these two. These relationships are demonstrated in Fig. 4.

2.1.2. *Si- and Sn-based LGPS with stoichiometry variations*

As for $Li_{10+d}Ge_{1+d}P_{2-d}S_{12}$ in the corresponding phase diagrams Li_2S–P_2S_5–MS_2 (M = Ge, Sn or Si), all $Li_{10+d}M_{1+d}P_{2-d}S_{12}$ compositions of the LGPS-type electrolytes are on the tie line Li_4MS_4–Li_3PS_4. The ranges for dominant monophasic

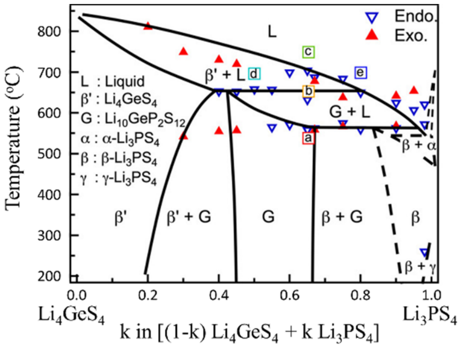

Fig. 4. Binary Li_4GeS_4–Li_3PS_4 phase diagram containing the $Li_{10+d}Ge_{1+d}P_{2-d}S_{12}$, k is used as parameter to describe the $Li_{10+d}Ge_{1+d}P_{2-d}S_{12}$ materials according to the notation $Li_{4-k}Ge_{1-k}P_kS_4$ or $(1 - k)Li_4GeS_4$–kLi_3PS_4. Reprinted with permission from Hori *et al*. © 2015 The American Ceramic Society.[19]

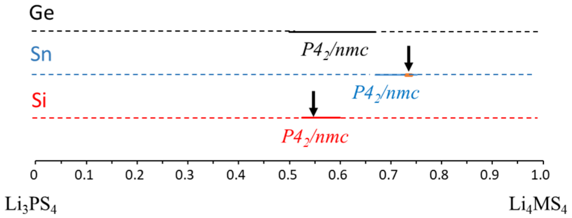

Fig. 5. Stability regions for dominant monophasic *P4$_2$/nmc*-structured $Li_{10+d}M_{1+d}P_{2-d}S_{12}$ (M = Ge, Sn, Si) displayed in a binary Li_4MS_4–Li_3PS_4 diagram (calculated according to data in Hori *et al.*).[21] Full lines indicate ranges of solid solutions with *P4$_2$/nmc* structure. Black, blue and red for M = Ge, Sn and Si, respectively. Arrows indicate regions of high LGPS phase purity.

$Li_{10+d}M_{1+d}P_{2-d}S_{12}$ are different for M = Ge, Sn or Si. The dominant monophasic region for the Ge-based electrolytes is $0 \le d \le 0.35$, the single-phase regions are $0.2 \le d \le 0.43$ for Si and $-0.25 \le d \le -0.01$ for Sn.[21] The corresponding fractions of Li_4MS_4 and Li_3PS_4 are defined on the Li_3PS_4–Li_4MS_4 tie line (Fig. 5).

2.1.3. *LGPS with binary semi/metal components*

Integrating two different semi/metal elements into the LGPS-type electrolyte materials was approached by investigating the series of $Li_{10+d}[Sn_ySi_{1-y}]_{1+d}P_{2-d}S_{12}$ materials and of the $Li_{10}[Ge_yM_{1-y}]P_2S_{12}$ series.[22,23] In both series, the y:(1 − y) ratios indicate the mixing of the respective semi/metal components, in the former the (1 + d):(2 − d) corresponds to the semi/metal vs. phosphorus content.

Materials with mixed semi/metal cations containing five elements cannot in general be displayed in a ternary phase diagram, however, the material's specific compositions are limiting the variations of the elements related by the parameter d, thus the LGPS-type materials can be represented in a phase diagram with components Li_3PS_4–Li_4SnS_4–Li_4SiS_4. This type of diagram is most useful to enlighten the stability range of the monophasic *P4$_2$/nmc* structure (Fig. 6). For the tin-rich materials, the stability range is at higher Li_3PS_4 contents, while for the silicon-rich materials, it is at slightly lower Li_3PS_4 contents. This trend continues for both the upper and lower bounds of stability.

Along each tie line Li_3PS_4–$Li_4Sn_ySi_{1-y}S_4$, the Sn/Si (= y/(1 − y) ratio is fixed, thus a corresponding representation of an individual tie line can be given in a ternary Li_2S–P_2S_5–$Li_4Sn_{0.4}Si_{0.6}S_4$ phase diagram (Fig. 7). Most importantly, the combination of Sn and Si widens the range of stable monophasic *P4$_2$/nmc* compositions for each $y \ne 0$ compared to the electrolytes containing either Sn or Si only. The combination of semi/metals component with ionic radius smaller ($r(Si^{4+}) = 0.26$ Å) and larger ($r(Sn^{4+}) = 0.55$ Å) than the ionic radius of Ge^{4+} ($r(Ge^{4+}) = 0.39$ Å) seems to stabilize the *P4$_2$/nmc* structure.[21]

The $Li_{10}[Ge_yM_{1-y}]P_2S_{12}$ series can be represented in similar Li_3PS_4–Li_4GeS_4–Li_4MS_4 (M = Si, Sn) phase diagram as well.

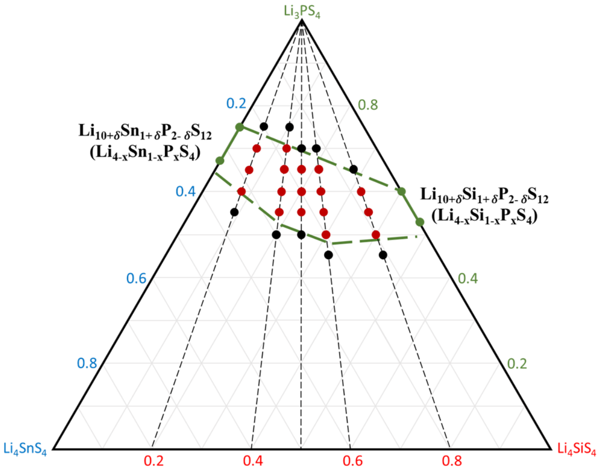

Fig. 6. Ternary phase diagram Li_3PS_4–Li_4SnS_4–Li_4SiS_4 indicating positions of $Li_{10+d}[Sn_ySi_{1-y}]_{1+d}P_{2-d}S_{12}$ and the stability range for *P4$_2$/nmc* phase materials denoted in red within the green dotted lines.

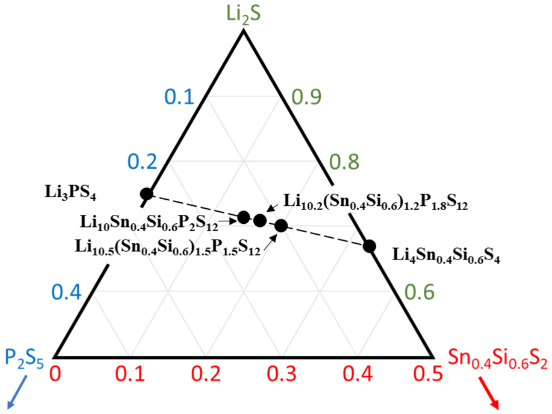

Fig. 7. Li_2S–P_2S_5–$Sn_{0.4}Si_{0.6}S_2$ phase diagram referring to different $Li_{10+d}[Sn_{0.4}Si_{0.6}]_{1+d}P_{2-d}S_{12}$ on the Li_3PS_4–$Li_4Sn_{0.4}Si_{0.6}S_4$ tie line.

These compositions lie on tie lines $Li_{10}GeP_2S_{12}$–$Li_{10}SiP_2S_{12}$ and $Li_{10}GeP_2S_{12}$–$Li_{10}SnP_2S_{12}$, respectively (Fig. 8). As there is no variation in neither the lithium content nor the total semi/metal content in this series, all materials are displayed on a line parallel to the Li_4GeS_4–Li_4MS_4 axis. Solid solutions are formed for lower amounts of Si or Sn substitution in the $Li_{10}GeP_2S_{12}$ base material, whereas at higher contents of Si or Sn Li_3PS_4-type secondary phase is detected.

2.1.4. *Li–P–S archetype LGPS*

An LGPS-type *P4$_2$/nmc*-structured electrolyte containing exclusively lithium, phosphorus and sulfur as chemical components with $Li_{9.6}P_3S_{12}$ composition was developed in 2016.[9] Taking prototype LGPS $Li_{10}GeP_2S_{12}$ as a starting point for analyzing the stoichiometry of $Li_{9.6}P_3S_{12}$ provides some insights in the design concept for this material.

A full substitution of the germanium by phosphorus, with concomitant charge compensating decrease in lithium

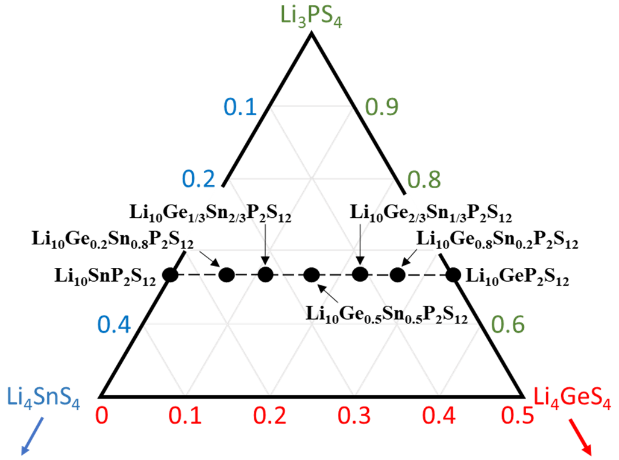

Fig. 8. Ternary phase diagram Li_3PS_4–Li_4GeS_4–Li_4MS_4 (M = Si, Sn) indicating the positions of $Li_{10}[Ge_yM_{1-y}]P_2S_{12}$ (M = Si, Sn) on the $Li_{10}GeP_2S_{12}$–$Li_{10}MP_2S_{12}$ tie line.[21]

content according to $Ge^{4+}+Li^{+} \rightarrow P^{5+}$ would result in $Li_9P_3S_{12}$ stoichiometry. Thus, the $Li_{9.6}P_3S_{12}$ can be considered as a LGPS with complete substitution of its Ge by P along with Li-excess. The P/S ratio matches 1/4, so the conditions for the arrangement of all sulfur in PS_4^{3-} tetrahedra are met. Considering its formula normalized to S_4, i.e. $Li_{3.2}PS_4$, and recalling the Li_3PS_4 is a "Li_2S–P_2S_5 tie-line composition", the lithium off-stoichiometry of $Li_{9.6}P_3S_{12}$ may also explain why it was not found in early investigations that were focusing on compositions synthesized from Li_2S and P_2S_5 only, and a systematic material search was necessary to discover this electrolyte.

2.1.5. *Halogen-doped LGPS*

The first halogen containing *$P4_2/nmc$*-structured LGPS-type electrolyte $Li_{9.54}Si_{1.74}P_{1.44}S_{11.7}Cl_{0.3}$ was developed in 2016.[9] It can be considered as derived from Si-based LGPS by chlorine doping, replacing small part of the sulfur by chlorine. The additional (negative) charges introduced by the chlorine are compensated to some part by a higher total Si+P content than in standard $Li_{10+d}M_{1+d}P_{2-d}S_{12}$ and by an adjustment in Li-content. In standard $Li_{10+d}M_{1+d}P_{2-d}S_{12}$, such as $Li_{10.35}Si_{1.35}P_{1.65}S_{12}$, the S+P content sums up to 3, whereas in the $Li_{9.54}Si_{1.74}P_{1.44}S_{11.7}Cl_{0.3}$, both silicon and phosphorus content are substantially higher in chlorine free Si-based LGPS. Thus, in $Li_{9.54}Si_{1.74}P_{1.44}S_{11.7}Cl_{0.3}$ neither the (Si+P)/S = 3.18/11.7 nor the (Si+P)/(S+Cl) = 3.18/12 ratio of the $Li_{9.54}Si_{1.74}P_{1.44}S_{11.7}Cl_{0.3}$ electrolyte matches the 1/4 ratio that is required for forming exclusively PS_4^{3-} and SiS_4^{2-} polyanions that were considered as a characteristic for the LGPS structure.

Detailed investigations of structure, microstructure and processing procedures will be necessary to clarify how the electrolyte nominal stoichiometry transforms to form *$P4_2/nmc$* structured LGPS. Core-shell morphology with Si- and Cl-rich compositions in the outer shell and small amounts of Argyrodite secondary phase are launched as tentative explanations.[17] Applying the same stoichiometry, $Li_{9.54}Si_{1.74}P_{1.44}S_{11.7}X_{0.3}$ for other halogens (X = F, Cl, Br, I) was reported to result in LGPS-type electrolytes as well.[32] Fluorine-doped tin-based electrolyte with nominal composition $Li_{9.95}SnP_2S_{11.95}F_{0.05}$ shows *$P4_2/nmc$* structure as the main component and ca. 5% Li_2SnS_3 secondary phase.[33] Considering the nominal composition, the (Sn+P)/(S+F) ratio matches 1/4, however, taking into account the secondary phase with Sn/S = 1/3, the actual (Sn+P)/(S+F) for the *$P4_2/nmc$* is slightly higher than 1/4 also for this material.

Most recent attempts to synthesize halogen-doped LGPS-type electrolyte are directed toward semi/metal free compositions in the system $(1 - x - y)$ Li_2S–xP_2S_5–yLiX focusing on arrange of Li_2S/P_2S_5 ratios around 75/25 with halogen substitution X (X = Br, I) of less than 10% related to sulfur.[34] A systematic material search was exploring the compositional range $0.15 < x < 0.25$ and $0.05 < y < 0.20$ with synthesis conditions kept in a narrow temperature window between 200°C and 220°C, as amorphous material below and β-Li_3PS_4 above these temperature boundaries is produced. On synthesis of the compositions of bromine- and iodine-doped materials $Li_{10}P_3S_{12}Br$ and $Li_{10.25}P_3S_{12.25}I_{0.75}$, at 210°C and 205°C, respectively, *$P4_2/nmc$*-structured phosphosulfide electrolytes are formed.[34]

Considering phase compositions at synthesis temperatures 220°C and 200°C for the Br- and I-doped materials, the structures of $Li_{10}P_3S_{12}Br$ and $Li_{10.25}P_3S_{12.25}I_{0.75}$ were not clearly identified. At these temperatures, products of the synthesis compositions with higher Li_2S content yield residual Li_2S starting material as the main phase component. Deviation of the $Li_{10}P_3S_{12}Br$ and $Li_{10.25}P_3S_{12.25}I_{0.75}$ stoichiometry results in LiX, β-Li_3PS_4, Li_6PS_5X or phase mixtures thereof depending on the fractions of Li_2S, P_2S_5 and LiX in the educts (Fig. 9).

2.1.6. *Oxygen-substituted LGPS*

Oxygen substitution for sulfur in LGPS-type electrolytes has been attempted in Ge-based, Si-based, as well as in semimetal-free Li–P–S form LGPS and Si–Cl co-doped LGPS.[35] The substitution of oxygen for sulfur is isovalent, thus the modification in this component *per se* does not require further adjustments of stoichiometry.

In Ge-based LGPS, stable solid solutions when partially substituting sulfur by oxygen according to $Li_{10}GeP_2S_{12-x}O_x$ were found in the solid solution range from $0 < x < 0.9$.[25] Higher oxygen contents resulted in the formation of Li_3PO_4. The largest part of the oxygen is integrated in mixed $P/(S/O)_4^{3-}$ tetrahedra, smaller part of it also substitutes sulfur in

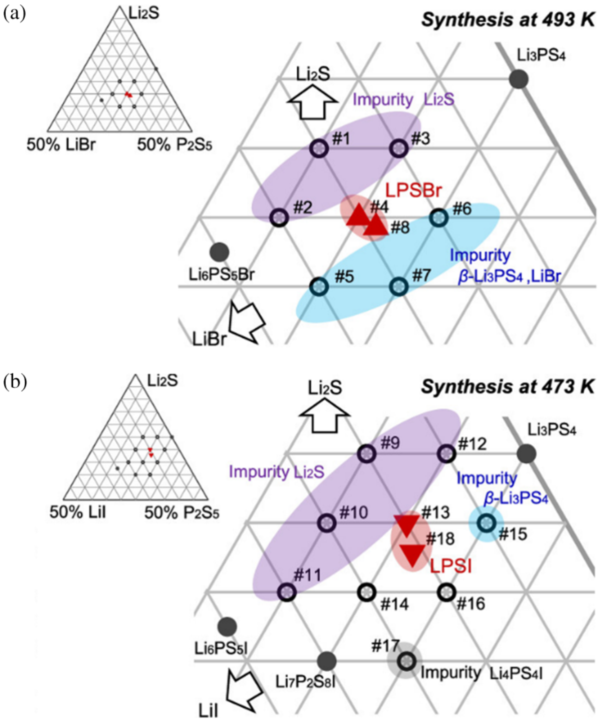

Fig. 9. Quasi-ternary systems Li_2S–P_2S_5–LiX and magnified views around the sample compositions showing the product phases obtained at synthesis temperatures of 493 K and 473 K for (a) X = Br and (b) X = I. Reprinted with permission from Ref. 34. Copyright © 2022 American Chemical Society.

$Ge/(S/O)_4^{2-}$. The limited solubility of oxygen is attributed in part to the large difference in the ionic radii between oxygen (1.84 A) and sulfur (1.38 A).[25]

Oxygen incorporation works in silicon-based LGPS as well.[26] LGPS-type electrolyte $Li_{9.42}Si_{1.02}P_{2.1}S_{9.96}O_{2.04}$ and $Li_{9.6}Si_{1.02}P_{2.064}S_{9.96}O_{2.04}$ were successfully synthesized applying quenching. Remarkably, the oxygen content in these Si-based electrolyte is much higher for the oxygen-substituted Ge-based LGPS. However, the (P+Si)/(S+O) ratio has to be shifted to fractions higher than 1/4. Attempts to synthesize pure phase *P4₂/nmc* structured electrolyte applying stoichiometries corresponding to the tie line Li_3PS_4–$Li_4Si_2O_2$ compositions in a Li_2S–P_2S_2–SiO_2 phase diagram did not provide phase pure *P4₂/nmc* electrolytes.

Exploring a wide compositional range of oxygen-substituted Li–P–S–O materials $Li_{9+15x}P_{3-3x}S_{12-3z}O_{3z}$ with x and z ranging from $0.03 \le x \le 0.08$ and $0 \le z \le 1$, respectively, in some of the electrolytes among this scope LGPS-type *P4₂/nmc* structure was identified as majority phase.[28] The subseries of $Li_{9+15x}P_{3-3x}S_{12-3z}O_{3z}$ with $x = 0$ can be considered as a Li_3PS_4–Li_3PO_4 binary material. For a more general overview on the stoichiometries, the materials can be represented in a ternary Li_2S–P_2S_5–P_2O_5 phase diagram (Fig. 10). In such diagram, the materials realized in the $Li_9PS_{12-3z}O_{3z}$ ($Li_3PS_{4-z}O_z$) subseries with $0 \le z \le 1$ covers the first quarter of Li_3PS_4–Li_3PO_4 tie line toward its Li_3PS_4 side. All other materials subseries with constant Li and P contents (i.e. x constant but nonzero) lie along lines parallel to the Li_3PS_4–Li_3PO_4 tie line.

The phase compositions are subject to changes along with increasing oxygen content. Specifically, for the $Li_{10.15}P_{2.79}S_{12-3z}O_{3z}$ ($Li_{3.35}P_{0.93}S_{4-z}O_z$) ($x = 0.07$) materials subseries, three regions can be distinguished. With oxygen contents up to $z = 0.3$, mostly γ-Li_3PS_4 along with Li_7PS_6 minority phase is identified in the materials. The region with *P4₂/nmc*-structured LGPS-type majority phase extends from oxygen contents $z = 0.4$–0.6 ($Li_{10.15}P_{2.79}S_{10.8}O_{1.2}$ to $Li_{10.15}P_{2.79}S_{10.2}O_{1.8}$). With the presence of a higher oxygen content, the appearance of a phase hitherto not identified is observed. More general, considering the complete range of compositions, the LGPS-type electrolytes exist in the range over $x = 0.03$–0.08 and for $z = 0.4$–0.8.[28] Thus, while within the electrolytes in the Li_3PS_4–Li_3PO_4 subseries ($x = 0$) with their P/(S+O) ratios 1/4 no materials with *P4₂/nmc* structure were identified, along with moderate reduction of the phosphorus content ($x > 0$) and corresponding lower P/(S+O) ratios LGPS-type electrolytes could be realized in this system.

An extended investigation of semi/metal free oxygen-substituted LGPS was recently carried out analyzing a

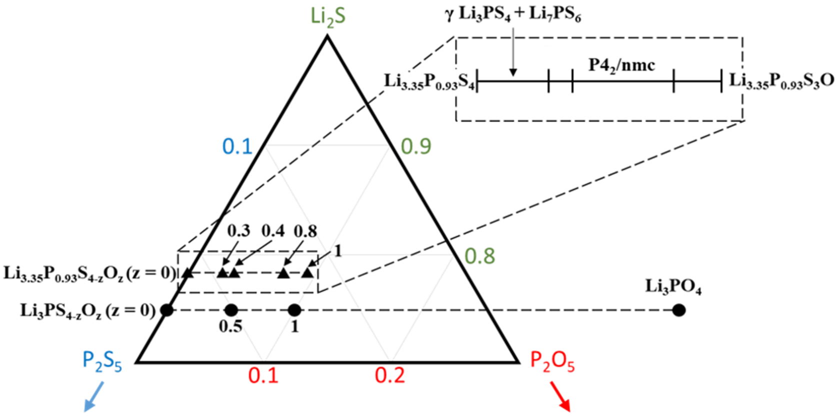

Fig. 10. Ternary Li_2S–P_2S_5–P_2O_5 phase diagram indicating the positions of materials of the $Li_3PS_{4-z}O_z$ and the $Li_{3.35}P_{0.93}S_{4-z}O_z$ subseries.[28]

$L_{9+d}P_{3+d'}S_{12-k}O_k$ series.[36] The target $P4_2/nmc$ was formed over the nominal composition range $k = 0.6$, $0.3 > d > 0.9$ and $-0.075 < d' < 0.075$, thus for materials with phosphorus contents varying from to $L_{9+d}P_{2.925}S_{11.4}O_{0.6}$ to $L_{9+d}P_{3.075}S_{11.4}O_{0.6}$ and P/(S+O) ratios lower as well as higher than 1/4. Experimentally, a lower limit of $k = 0.45$ was determined for the formation of the LGPS phase. As diffraction results indicate that the oxygen occupies exclusively S1 sites the hypothesis that maximum oxygen substitution that allows for $P4_2/nmc$ structure is $k = 4$.

The semimetal/halogen co-doped LGPS-type electrolyte $Li_{9.54}Si_{1.77}P_{1.44}S_{11.7}Cl_{0.3}$ has also been used a base composition for modification by oxygen substitution.[35] Keeping the Li, the Si and the Cl fractions in the composition constant, high phase purity LGPS was synthesized within this $Li_{9.54}Si_{1.77}P_{1.44}S_{11.7-z}Cl_{0.3}O_z$ $(0 < z < 1.5)$ series for $z = 0.15$, 0.3 and 0.6. Compared to the oxygen-free composition, the substitution on oxygen stabilized the $P4_2/nmc$ structure in these electrolytes on processing. Increase in oxygen content, however, results in the presence of substantial amounts of secondary phases. Argyrodite-type secondary phase was found in $Li_{9.54}Si_{1.77}P_{1.44}S_{10.8}Cl_{0.3}O_{0.9}$ $(z = 0.9)$ while LiSICon-type $Li_4Si_{0.4}P_{0.6}S_4$ were detected in the $Li_{9.54}Si_{1.77}P_{1.44}S_{10.2}Cl_{0.3}O_{1.5}$ $(z = 1.5)$ material.

2.2. *LGPS-type structure*

Characteristic for the structure of LGPS-type electrolytes is the space group $P4_2/nmc$. In the case of $Li_{10}GeP_2S_{12}$ materials, the temperature-dependent phase diagram Li_3PS_4 and Li_4GeS_4 demonstrates that below the solidus line there are no high-temperature phases with different structures (Fig. 4). The structure of LGPS electrolytes consists of anion building blocks of isolated tetrahedra formed by phosphorus and/or semi/metals PS_4^{3-} and MS_4^{2-} (M = Ge, Si, Sn). These components form the anionic skeleton of the structure. The Li-ions are distributed within the interspaces between the building blocks of the skeleton (Fig. 11).

There are two different sites for the phosphorus or semi/metal centers of the tetrahedra (Wyckoff positions 4d and 2d). In LGPS, the $[P1/Ge1]S_4$ 4d positions are shared by phosphorus and germanium, whereas the $[P2]S_4$ 2d position is occupied exclusively by phosphorus. The lithium is distributed among four different sites, two of them, Li1 and Li3 on 16h position, and Li2 and Li4 on 4d and 4c positions, respectively. The lithium atoms can be considered as coordinated by a neighboring sulfur atom forming coordination polyhedral. Thereby, Li1 and Li3 are relatively close to the coordinated sulfur atoms and form an edge-shared tetrahedral chain along the *c*-axis (Fig. 11(a2)). In the case of the Li2 and Li4 sites, the sulfur atoms are more remote, nevertheless these lithium atoms can be regarded as six-coordinated, forming $[Li2]S_6$ and $[Li4]S_6$ octahedra. These octahedra are connected to $[Li3]S_4$ or $[Li1]S_4$ via edge-sharing. These connected lithium-sulfur polyhedra form chains within the *a*–*b* plane (Figs. 11(a3) and 11(a4)).[18]

The chains or channels in the interspaces of this anion framework are considered to be pathways for the lithium transport. From a merely structural point of view, the width of the channels for the lithium transport and the absence of bottlenecks are the descriptors of the conditions for transport in the channels. The channel width is related on the one hand to the lattice spacing, on the other hand to the volume of the PS_4^{3-} and MS_4^{2-} polyhedra. Detailed work has been done with respect to the comparison of the lattice parameters for the different types of LGPS.

Modification of the stoichiometry of the prototype electrolyte $Li_{10}GeP_2S_{12}$ according to $Li_{10+d}Ge_{1+d}P_{2-d}S_{12}$ for $(-0.1 \le d \le 0.5)$ leads to an increase in lattice parameters *a* and *c* along with an increase in *d*, i.e. an increasing germanium content along with a diminution in the phosphorus content (Fig. 12).[18] Along with an increased Ge:P ratio as realized

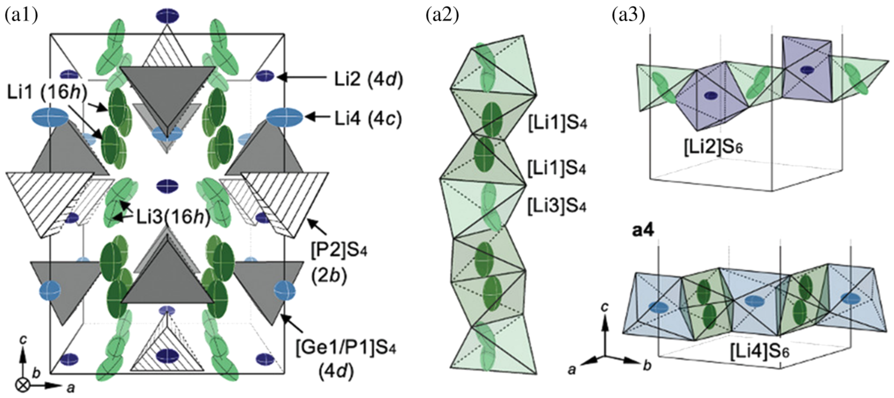

Fig. 11. Illustration of the original LGPS Crystal structure. (a1) Overview of the Li sites (with unit cell) within the tetrahedral skeleton. (a2) Arrangement of connected polyhedral units with Li sites as their center (e.g. [Li1]S4 and [Li3]S4). A section of the unit cell is shown in (a3) [Li3]S4 and [Li2]S6 and (a4) [Li1]S4 and [Li4]S6. Reprinted with permission from Kato *et al*. © 2020 Wiley-VCH GmbH.[17]

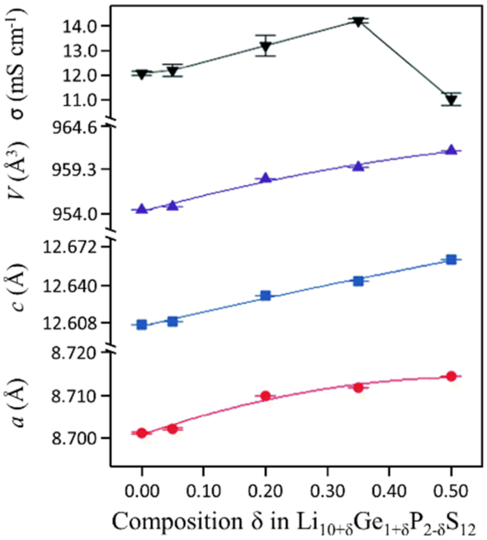

Fig. 12. Lattice parameters and cell volume for $Li_{10+d}Ge_{1+d}P_{2-d}S_{12}$ ($-0.1 \le d \le 0.5$). Reproduced from Ref. 18 with permission from the Royal Society of Chemistry © 2013.

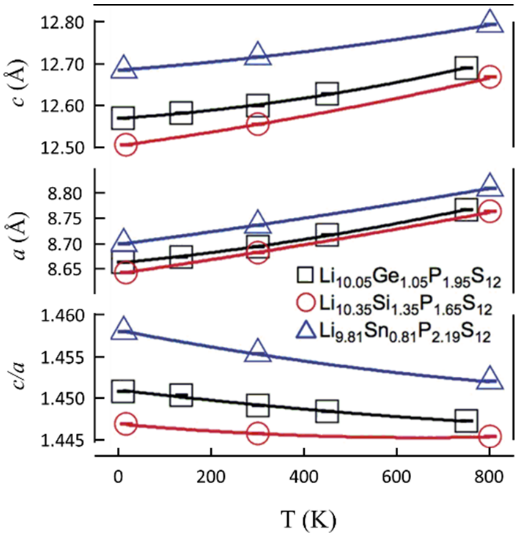

Fig. 13. Lattice parameters for $Li_{10.05}Ge_{1.05}P_{1.95}S_{12}$, $Li_{10.35}Si_{1.35}P_{1.65}S_{12}$ and $Li_{9.81}Sn_{0.81}P_{2.19}S_{12}$ at different temperatures. Reproduced with permission of the International Union of Crystallography.[38]

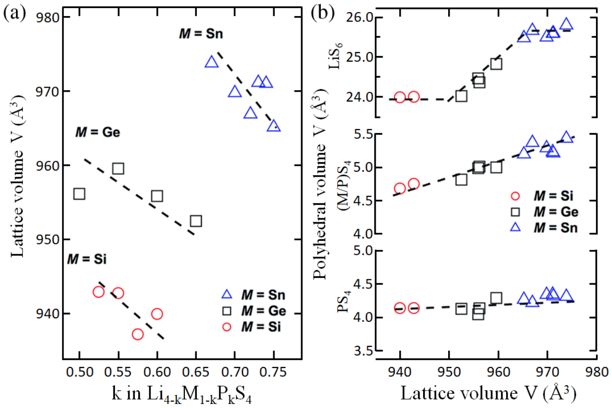

Fig. 14. (a) Lattice parameters and (b) volume of the polyhedral units PS_4, $(M/P)S_4$ and LiS_6 for $Li_{4-k}M_{1-k}P_kS_4$ (M = Ge, Sn or Si). Original work normalizes sulfur content to S_4. Lower and upper bound k-values of 0.525 and 0.75 correspond in the $Li_{10+d}M_{1+d}P_{2-d}S_{12}$ notation to d-values of 0.425 and –0.25, respectively. Reproduced from Ref. 21 with permission from the Royal Society of Chemistry © 2014.

Table 1. Lattice parameters and cell volume for $Li_{10}GeP_2S_{12}$ vs. $Li_7GeP_2S_8$.

Material	a (Å)	c (Å)	V (Å³)	Ref.
$Li_{10}GeP_2S_{12}$	8.717	12.634	960.008	7
$Li_{10}GeP_2S_{12}$	8.708	12.615	956.586	37
$Li_{10}GeP_2S_{12}$	8.714	12.607	957.297	31
$Li_7GeP_2S_8$	8.718	12.660	962.205	31

by the $Li_7GeP_2S_8$ electrolyte, the lattice parameter a does not change significantly vs. the lattice parameter for $Li_{10}GeP_2S_{12}$, but the c-axis for the former material is substantially elongated (Table 1).[31]

The influence of the semi/metal component and temperature on lattice parameters was compared for $Li_{10.05}Ge_{1.05}P_{1.95}S_{12}$, $Li_{10.35}Si_{1.35}P_{1.65}S_{12}$ and $Li_{9.81}Sn_{0.81}P_{2.19}S_{12}$ (Fig. 13).[38] The lattice parameters increase slightly, and the lattice parameter c is more pronounced in a sequence from Si to Ge to Sn. Along with higher temperature, both lattice parameters a and c increase. Quantitatively, the changes for the two parameters are not proportional, leading to a decrease in the c/a lattice distortion with an increase in temperature. However, as the stoichiometry of the materials is not the same, it is difficult to attribute the differences among the materials at a given temperature unequivocally to the type of semi/metal.

Clear evidence for the impact of the type of semi/metal results from a compound analysis of the systems $Li_{10+d}M_{1+d}P_{2-d}S_{12}$ with M = Ge, Sn or Si (Fig. 14).[21] In addition to the cell volumes, the data include information on the volumes of the polyhedrals PS_4, $(M/P)S_4$ and the LiS_6 octahedra. Within the respective ranges of solid solutions, the lattice volumes are the smallest for the silicon-based and the largest for the tin-based LGPS electrolytes. The volumes for the germanium-based LGPS electrolytes are approximately halfway between them. Overall, the differences in lattice volumes depending on the semi/metal component reflect the ionic radii of these elements Si^{4+}, Ge^{4+} and Sn^{4+} with 0.26 Å, 0.39 Å and 0.55 Å, respectively.

Analysis of the structure of the mixed cation systems germanium–silicon and germanium–tin for compositions $Li_{10}(Ge_{1-x}Si_x)P_2S_{12}$ and $Li_{10}(Ge_{1-x}Sn_x)P_2S_{12}$ ($0 \le x \le 1$) provided single-phase solid solutions with space group $P4_2/nmc$. Si-substitution of Ge reduced the lattice parameters, whereas lattice parameters were increased by substitution of Ge by Sn (Fig. 15).[22]

Trends in lattice parameters along with the partial substitution of oxygen for sulfur were investigated for Ge-based

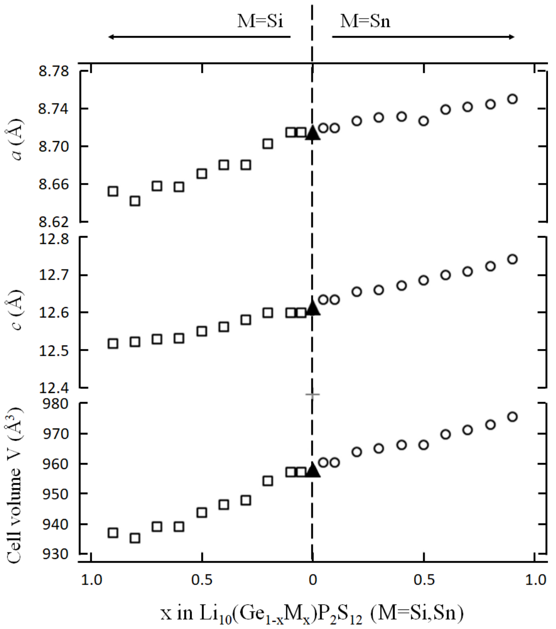

Fig. 15. Lattice parameters of $Li_{10}(Ge_{1-x}Si_x)P_2S_{12}$ and $Li_{10}(Ge_{1-x}Sn_x)P_2S_{12}$ for the compositions $0 \leq x \leq 1.0$, central data are for $Li_{10}GeP_2S_{12}$, increasing Si content is shown toward the left, increasing Sn content toward the right. Reprinted with permission from Kato *et al.* © 2014 Elsevier.[22]

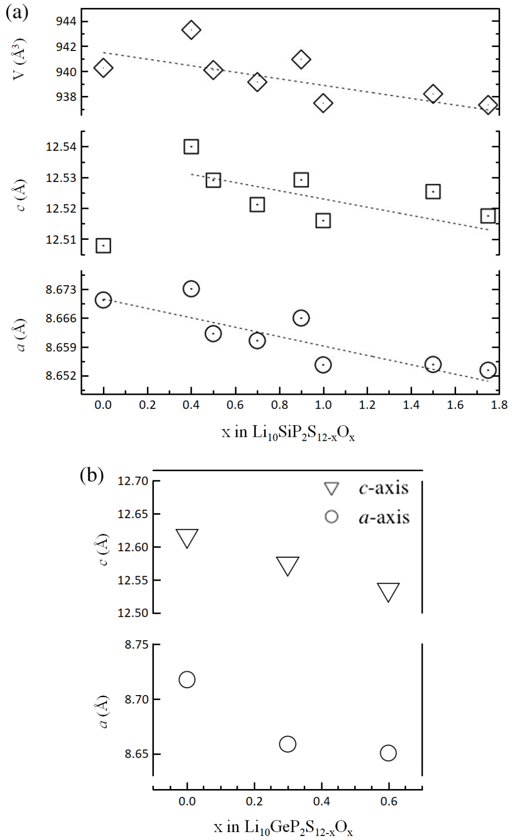

Fig. 16. Lattice parameters and cell volumes for (a) $Li_{10}SiP_2S_{12-x}O_x$ ($0.0 \leq x \leq 1.75$) depending on oxygen content. Reprinted with permission from Ref. 27. Copyright © 2019 American Chemical Society. (b) Lattice parameters and cell volumes for $Li_{10}GeP_2S_{12-x}O_x$ for $x = 0$, 0.3 and 0.6. Reprinted with permission from Sun *et al.* © 2016 Elsevier.[25]

$Li_{10}GeP_2S_{12-x}O_x$ ($0.3 \leq x \leq 0.6$) and Si-based $Li_{10}SiP_2S_{12-x}O_x$ ($0.0 \leq x \leq 1.75$) electrolytes.[25,27] In both materials, lattice parameters, *a* and *c* decrease along with higher oxygen content (Fig. 16) according to the ionic radii change from S^{2-} toward the smaller O^{2-} radii.

2.3. *LGPS-type processing*

Solid-state routes with educts, like Li_2S, P_2S_5 and semi/metal-disulfides GeS_2, SiS_2 or SnS_2, are the most widespread processes for the synthesis of LGPS materials.[7,9,18,20,30,31,37–41] Alternatively, LGPS can be synthesized from the elements Li, Ge, P and S.[42] This approach, however, requires a quite large sulfur excess in the educt stoichiometry (Li:Ge:P:S of 10:1:2:24) for $Li_{10}GeP_2S_{12}$. A wide scope for the devices used for milling and the milling duration as well as for the setting of the heat treatment step is reported. Milling process conditions range from 30 min milling time in a vibrational mill to 40 h mixing and grinding in a planetary ball mill.[7,21] Although the temperatures applied for oxygen free materials in the heat treatment step with maximum temperatures around 550°C are quite similar, the dwell times vary from 8 h to 72 h.[7,21] An investigation of the impact of sintering temperatures in the range between 500°C and 650°C along with a 2 h dwell time on Li-ion conductivity for $Li_{10}SnP_2S_{12}$, prepared by a solid-state route using nanocrystalline SnS_2 from hydrothermal synthesis, showed a maximum conductivity at $T_s = 600°C$.[43] With respect to this result, one has to take into account that the dwell time in these experiments is substantially shorter than in most other processes applied to LGPS-type materials (typically 8–72 h). The heat treatments are generally carried out in quartz tubes sealed under Argon atmosphere, evacuated (vacuum sealed) quartz tubes,[7,9,18,20,30,31,37–41] or in an Ar-protected tube furnace.[42]

Even though synthesis along with nonrate controlled cooling is possible,[37] in most reports emphasis is put on the importance of slow cooling rates (1°C/h). Major issues of concern for synthesizing monophasic LGPS electrolytes are the formation of secondary phases, the formation of glass phase and the loss of sulfur during heat treatment. If these issues become critical, it depends on the composition of the electrolyte materials, the choice of raw materials, the heat treatment conditions and also the form, pelletized or loose powder, in which the homogenized educts are heat treated. The trend for solid-state processing parameters seems to develop toward long milling, long dwell times during and slow cooling rates after heat treatment. This holds in the first instance for the materials with semi/metal cations as the only dopants.

Preparation conditions for merely Li–P–S-based and semi/metal-halogen-doped and Li–P–S are similar with respect to milling, but different with respect to the temperatures. The LGPS-type $Li_{9.6}P_3S_{12}$ is prepared by 120 h ball milling and heat treatment at 230°C–260°C for 4 h in the furnace.[9] Along with Li_2S, P_2S_5 and LiBr or LiI educts, low (200°C–220°C) temperatures are also applied for the synthesis of *P4₂/nmc*-structured $Li_{10}P_3S_{12}Br$ and $Li_{10.25}P_3S_{12.25}I_{0.75}$.[34] Extended milling times (40 h) and moderate heat treatment times (8 h) at relatively low temperatures (475°C) for the heat treatment were applied to synthesize $Li_{9.54}Si_{1.74}P_{1.44}S_{11.7}Cl_{0.3}$ from educts P_2S_5, SiS_2 and LiCl.[9]

In contrast to the oxygen-free LGPS electrolytes, the temperatures for the LGPS materials incorporating Li_2O or SiO_2 as oxygen sources are substantially higher (1000°C).[25,26] Moreover, cooling by quenching is reported for $Li_{9.42}Si_{1.02}P_{2.1}S_{9.96}O_{2.04}$ and its solid solutions.[26]

2.4. *LGPS type conductivity*

In the past 10 years after the first publication on an LGPS-type Li-ionic superconductor, the ongoing research activities have provided a wide scope of new material developments and results related to this type of electrolyte.[7] On a microscopic scale, the conduction pathways for Li-ions and the tools to control them are still under discussion, and on the macroscopic scale, the research on high performance, resource efficient and stable LGPS electrolytes is ongoing.

Briefly summarizing the issues regarding Li-ion conductivity on an atomistic scale, the LGPS anion lattice framework consists of PS_4^{3-} and GeS_4^{2-} tetrahedra, while Li-ions are distributed on four different sites within this framework. The lithium can be considered to be a part of four and six coordinated LiS_4 and LiS_6 units. The Li-conduction in LGPS depends on the connectivity between these tetrahedral and octahedral units. In the case of two of the four Li-positions, it seems to be proven that their edge-sharing tetrahedra form Li-conducting chains in *c*-direction. The realization of chains formed by the octahedral LiS_6 together with tetrahedral units, which may result in conduction pathways in the *a*–*b* direction, is still under discussion.

The discussion of the conductivity on a macroscopic scale focusing on the performance of the electrolytes will be split into three subtopics before summarizing the results in a concluding section. On the one hand, the first part will be concerned with modifications of the germanium-based prototype materials with respect to stoichiometry, taking into account the effects of the different procedures for preparation of the samples for the conductivity measurements. On the other hand, this part focuses on a comparison of two types of Li–Ge–P–S materials with highly similar chemical compositions, the LGPS-type electrolytes and the electrolytes originally considered as thio-LiSICon. In the second part, the influence of the semi/metal providing the MS_4^{-2} tetrahedra — Ge vs. Si vs. Sn — on the Li-ion conductivity will be analyzed. The third part deals with the impact of anion substitution by oxygen or halogen incorporation for sulfur in the LGPS-type materials on their Li-ion conductivity.

2.4.1. *Germanium-based LGPS*

With respect to modifications of the stoichiometry of germanium-based LGPS, research is focused on the $Li_{10+d}M_{1+d}P_{2-d}S_{12}$ stoichiometry. The phases in this series of materials can be presented as a mixture of Li_3PS_4 and Li_4GeS_4, which in turn are binary mixtures of Li_2S and P_25 or Li_2S and GeS_2, respectively. According to investigations of a series in $Li_{10+d}Ge_{1+d}P_{2-d}S_{12}$ with $-0.1 \leq x \leq 0.5$, single-phase *P4₂/nmc* LGPS exists within a compositional range of $0 \leq d \leq 0.35$.[18] All compounds within this compositional range have a similar high level of conductivity, i.e. differing less than one order of magnitude (Fig. 17). Moreover, Li-ion conductivity of $Li_{10.35}Ge_{1.35}P_{1.65}S_{12}$ even higher than those that was found for the LGPS prototype. Differences of ambient temperature Li-ion conductivity of $3–5 \times 10^{-3}$ S/cm arise with respect to conductivity measurements on sintered samples vs. compressed powders.[18] Attempts to reproduce materials from the $Li_{10+d}Ge_{1+d}P_{2-d}S_{12}$ series were in large part successful, resulting in electrolytes with only relatively small reduction in performance (Fig. 17) when compared to those prepared by the group of the inventors of the LGPS at Tokyo Institute of Technology.[31,42,47,48]

Considering the relatively good stability of processing of the $Li_{10+d}Ge_{1+d}P_{2-d}S_{12}$ series, it seems quite puzzling, that for electrolytes with compositions $Li_{4-k}Ge_{1-k}P_kS_4$, analyzed in 2001 by the Tokyo Institute of Technology, structure and performance differ.[30] Given in terms of the $Li_{10+d}Ge_{1+d}P_{2-d}S_{12}$, the $Li_{4-k}Ge_{1-k}P_kS_4$ compositional range $0.5 \leq k \leq 0.7$ corresponds to $-0.1 \leq d \leq 0.5$. Although the 2001 $Li_{4-k}Ge_{1-k}P_kS_4$ series materials were the best performing electrolytes at that time,

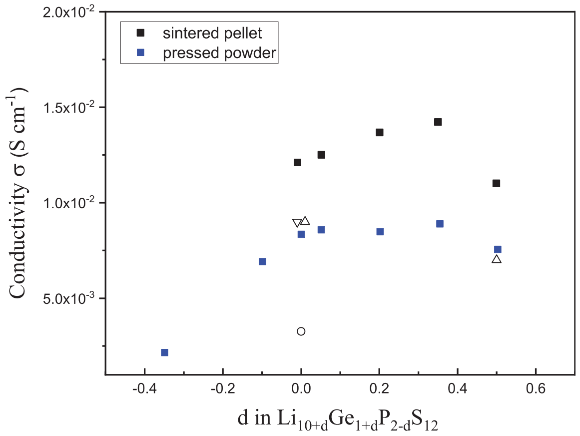

Fig. 17. Ambient temperature Li-ion conductivity for $Li_{10+d}Ge_{1+d}P_{2-d}S_{12}$ electrolytes[18] comparing conductivity for sintered ceramics vs. cold pressed pellets. Data on conductivities shown are from Kwon (black and blue squares) Δ: Kuhn *et al.*,[44] ∇: Bron *et al.*[45] and ○: Zhang *et al.*[46]

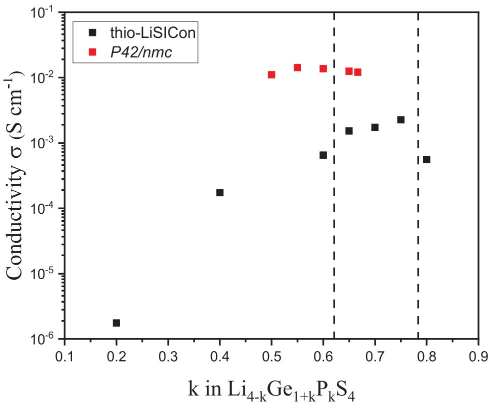

Fig. 18. Ambient temperature Li-ion conductivity of $P4_2/nmc$ structured $Li_{4-k}Ge_{1-k}P_kS_4$ sintered pellets[18] vs. $Li_{4-k}Ge_{1-k}P_kS_4$ with very similar chemical composition, originally considered as thio-LiSICon.[30]

their Li-ion conductivities are roughly an order of magnitude lower than those of the LGPS-type electrolytes (Fig. 18).

Moreover, the structure of the former electrolytes, originally approached by fitting according to a LiSICon-like monoclinic $P2_1/m$ space group, is not completely understood up to today.[17] Although arguing on the differences between these two series of materials is up to some extent speculative, a possible reason might be the differences in temperatures for the heat treatments. While the $Li_{10+d}Ge_{1+d}P_{2-d}S_{12}$ LGPS $P4_2/nmc$ electrolytes were prepared at temperatures of 550°C,[18] the temperature during the synthesis of the original $Li_{4-k}Ge_{1-k}P_kS_4$ was 700°C.[30] According to the binary Li_3PS_4–Li_4GeS_4 phase diagram, temperatures higher than 550–650°C approximately exceed the solidus of compositions $Li_{4-k}Ge_{1-k}P_kS_4$ ($0.45 \le k \le 0.65$).[19] Thus, for synthesis of the original $Li_{4-k}Ge_{1-k}P_kS_4$ 2001 series, most probably a liquid-phase intermediate stage was involved, whereas the synthesis of the $Li_{10+d}Ge_{1+d}P_{2-d}S_{12}$ LGPS should remain, at least in large, in the solid-state regime.

2.4.2. *Ge vs. Si vs. Sn — The influence of the semi/metal base in LGPS*

Motivated by the substitution of rare expensive germanium by resource-efficient semi/metals, LGPS-type electrolytes based on Si and Sn semi/metal components were developed. The ambient temperature Li-ion conductivities of the Si- and Sn-containing electrolytes are very high, although they do not reach the level of the best Ge-based LGPS compositions. Figure 19(a) provides an overview of the $Li_{10+d}M_{1+d}P_{2-d}S_{12}$ electrolytes within a scope limited to materials considered to be almost single phase.

For the electrolytes with a single semi/metal component, $Li_{10+d}Si_{1+d}P_{2-d}S_{12}$ and $Li_{10+d}Sn_{1+d}P_{2-d}S_{12}$, the ambient temperature Li-ion conductivities for the highest performing materials of these series are 6.7×10^{-3} S/cm for $Li_{10.35}Si_{1.35}P_{1.65}S_{12}$ and 5.0×10^{-3} S/cm for $Li_{9.81}Sn_{0.81}P_{2.19}S_{12}$, both at levels well below 10^{-2} S/cm.[21] Slightly higher Li-ion conductivities at ambient temperature in the Ge_xSn_{1-x} and Ge_xSi_{1-x} based LGPS are in particular at compositions $Li_{10}Ge_{0.95}Si_{0.05}P_2S_{12}$ and $Li_{10}Ge_{0.95}Sn_{0.05}P_2S_{12}$ (8.6×10^{-3} S/cm for $Li_{10}Ge_{0.95}Si_{0.05}P_2S_{12}$) (Fig. 19(a)).[22] Due to the relatively high germanium fraction in the semi/metal components of these materials, they do not provide an actual substitution for the exclusively germanium-based LGPS on a technical level. However, a very high performance germanium free electrolyte in the LGPS structure with an ambient temperature Li-ion conductivity of 1.1×10^{-2} S/cm can be realized with a binary $[Sn_ySi_{1-y}]_{1+\delta}$ component, such as for $Li_{10.35}Sn_{0.27}Si_{1.08}P_{1.65}S_{12}$.[23]

2.4.3. *Oxygen substitution in LGPS*

Issues with respect to the electrochemical stability of the LGPS materials promoted further research on this type of electrolyte. Motivated by the result from theory, that

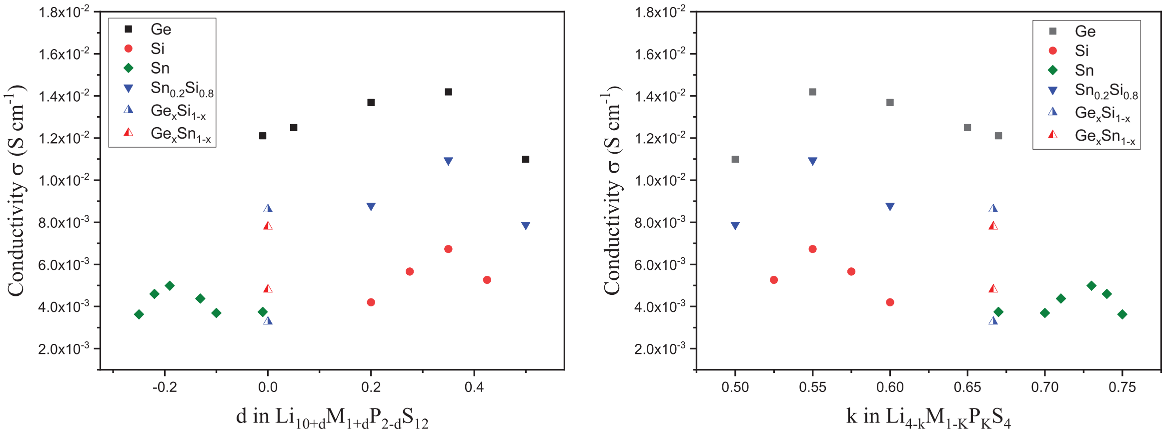

(a)

(b)

Fig. 19. Ambient temperature Li-ion conductivity of semi/metal-based LGPS electrolytes with M = Ge, Sn, Si and $Sn_{0.2}Si_{0.8}$. The symbols for the LGPS electrolytes with M = Ge_xSn_{1-x} and Ge_xSi_{1-x} denote upper and the lower bounds of Li-ion conductivities realized with the electrolytes. The compositions for the LGPS are plotted in terms of the (a) d-parameters for $Li_{10+d}Si_{1+d}P_{2-d}S_{12}$ and (b) k-parameters for $Li_{4-k}Ge_{1-k}P_kS_4$. Data and references are found in Table 2.

oxygen-based $Li_{10}MP_2X_{12}$ electrolyte materials have wider band gaps, and thus a higher electrochemical stability window than their sulfur-based counterparts, approaches for partial substitution of the sulfur by oxygen in these materials were forwarded. The approaches to develop oxygen-doped LGPS materials differ with respect to the semi/metal base component and the contents of the substituting oxygen. Considering the effects of isovalent substitution of sulfur by oxygen, it is established that the oxygen is replacing sulfur at one specific site, in the Li-S1 tetahedron, among three crystallographically equivalent sites.[17] The impact of oxygen incorporation on Li-ion conductivity, however, is quite different for Ge-based LGPS with low and for Si-based LGPS with high oxygen contents.

In the LGPS with Si as the semi/metal component, $Li_{9.42}Si_{1.02}P_{2.1}S_{9.96}O_{2.04}$, the ambient temperature Li-ionic conductivity is 3.2×10^{-4} S/cm,[26] which is substantially lower than the Li-ionic conductivity of a Si-based oxygen-free electrolyte, which amounts to 6.7×10^{-3} S/cm for $Li_{10.35}Si_{1.35}P_{1.65}S_{12}$.[21] The oxygen content in the $Li_{9.42}Si_{1.02}P_{2.1}S_{9.96}O_{2.04}$ material is relatively high. In contrast, an ambient temperature Li-ion conductivity close to those of the corresponding oxygen-free Ge-based LGPS materials was found for $Li_{10}GeP_2S_{11.7}O_{0.3}$ for which, while keeping the oxygen content moderately low, has an ambient temperature Li-ion conductivity of 1.03×10^{-2} S/cm.[23] In general, oxygen substitution seems to lower the Li-ion conductivity in LGPS electrolytes. With high oxygen substation, the crystalline LGPS-like phases degrade and generate the oxygen-rich Li_3PO_4 phase which has a lower Li-ion conductivity.[27] At lower oxygen substitution levels, the reduction in Li-ion conductivity may be due to the slight contraction of lattice parameters along with a strong electrostatic attraction between Li-ions and oxygen atoms.[25] Another contributing factor could be the smaller lattice volumes of the oxysulfides formed.[28]

2.4.4. *Summary on conductivity in LGPS*

A summary of some of the best performing LGPS-type electrolytes is provided in Fig. 20. Most materials that rely exclusively on a semi/metal modification of the phosphosulfide framework are among the electrolytes with Li-ion conductivities close to or slightly higher than 10^{-2} S/cm at ambient temperature. All these materials are $Li_{10+d}M_{1+d}P_{2-d}S_{12}$ type. Thereby, the highest Li-ion conductivities are realized with germanium-based electrolytes $Li_{10.35}Ge_{1.35}P_{1.65}S_{12}$ and $Li_{10}GeP_2S_{12}$ with slightly advantageous performances of the former at ambient temperature, and for the latter at elevated temperatures. Among the LGPS electrolytes with resource efficient semi/metal base, $Li_{10}Si_{0.5}Sn_{0.5}P_2S_{12}$ has an ambient temperature Li-ion conductivity most close to those of the Ge-based LGPS materials. The ambient temperature Li-ion conductivity of $Li_{9.6}P_3S_{12}$ is almost an order of magnitude lower than those of the semi/metal-containing LGPS electrolytes.

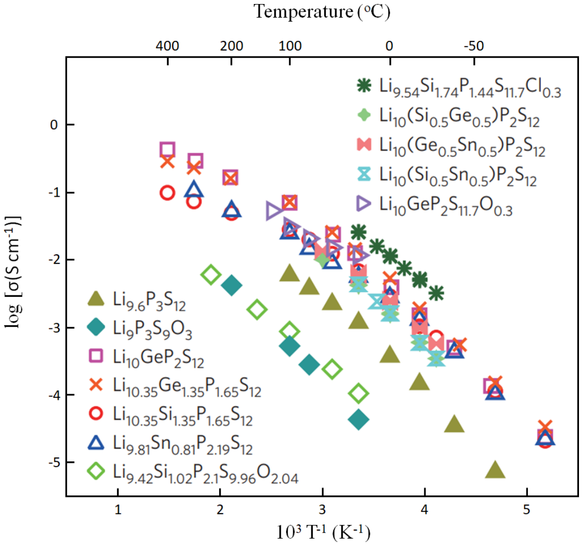

Fig. 20. Li-ion conductivity vs. temperature plots for the LGPS-type electrolytes including the $Li_{9.6}P_3S_{12}$ and $Li_{9.54}Si_{1.74}P_{1.44}S_{11.7}Cl_{0.3}$ LGPS. Reprinted with permission from Kato *et al.* © 2016 Springer Nature.[9]

Table 2. Li-ion conductivity and activation energies of LGPS type structures at ambient temperature unless otherwise stated. * Denotes results from simulation.

Stoichiometry	σ (S/cm)	E_a (eV)	Ref.
$Li_{3.25}Ge_{0.25}P_{0.75}S_4$	2.2×10^{-3}	0.207	30
$Li_{3.25}Ge_{0.25}P_{0.75}S_4$	1.82×10^{-4} (30°C)	0.42	39
$Li_{10.35}Ge_{1.35}P_{1.65}S_{12}$	1.42×10^{-2}	0.27	18
$Li_{10}GeP_2S_{12}$	$*1.3 \times 10^{-2}$	$*0.21 \pm 0.04$	40
$Li_{10}GeP_2S_{12}$	1.2×10^{-2}	0.249	7
$Li_{10}GeP_2S_{12}$	9.00×10^{-3}	0.22	31
$Li_{10}GeP_2S_{12}$	3.27×10^{-3}	0.264	42
$Li_{10}GeP_2S_{12}$	1.6×10^{-3}	—	49
$Li_{10}GeP_2S_{11.7}O_{0.3}$	1.03×10^{-2}	0.207	25
$Li_{10}GeP_2S_{11.4}O_{0.6}$	8.43×10^{-3}	0.218	25
$Li_{10}GeP_2O_{12}$	$*3.0 \times 10^{-5}$	*0.363	40
$Li_{9.54}Si_{1.74}P_{1.44}S_{11.7}Cl_{0.3}$	2.5×10^{-2}	—	9
$Li_{10}SiP_2S_{12}$	$*2.3 \times 10^{-2}$	$*0.20 \pm 0.03$	40
$Li_{10}Ge_{0.95}Si_{0.05}P_2S_{12}$	8.6×10^{-3}	0.244	22
$Li_{10.35}Si_{1.35}P_{1.65}S_{12}$	6.7×10^{-3}	0.27	21
$Li_{10}SiP_2S_{11.3}O_{0.7}$	$3.1 \pm 0.4 \times 10^{-3}$	0.33 ± 0.015	27
$Li_{9.42}Si_{1.02}P_{2.1}S_{9.96}O_{2.04}$	3.2×10^{-4}	0.349	26
$Li_{11}Si_2PS_{12}$ (calculated)	$\sim 0.8 \times 10^{-2}$	0.20	50
$Li_{10}SnP_2S_{12}$	$*6.00 \times 10^{-3}$	$*0.24 \pm 0.03$	40
$Li_{10}SnP_2S_{12}$	4.00×10^{-3}	—	20
$Li_{9.81}Sn_{0.81}P_{2.19}S_{12}$	5.00×10^{-3}	—	21
$Li_{11}AlP_2S_{12}$	$*3.3 \times 10^{-2}$	$*0.18 \pm 0.06$	40
$Li_{11}AlP_2S_{12}$	8.02×10^{-4}	0.263	51
$Li_3Y(PS_4)_2$	$*2.16 \times 10^{-3}$	*0.278	52
Li_7GePS_8	7.00×10^{-3}	0.22	31
$Li_{10.35}Sn_{0.27}Si_{1.08}P_{1.65}S_{12}$	1.1×10^{-2}	0.197	23

Very different effect on the Li-ion conductivity results from the substitutions in the anions. Substitution of sulfur by relatively high amounts of oxygen in semi/metal free and

Si-based LGPS results in Li-ion conductivities of more than one and almost two orders of magnitude lower than for the corresponding oxygen-free electrolytes. In contrast, Ge-based LGPS with moderate oxygen contents has a Li-ion conductivity that only slightly differs from that of the oxygen-free material. The most pronounced progress, however, is provided by the integration of halogen components in the LGPS. Development of Si-based LGPS with moderate halogen content along with modified stoichiometry resulted in the high performance electrolyte $Li_{9.54}Si_{1.74}P_{1.44}S_{11.7}Cl_{0.3}$ with to-date the highest Li-ion conductivity of 2.53×10^{-2} S/cm at 90% pellet density and 1.40×10^{-2} S/cm for a 75% dense powder compact at ambient temperature.[9]

3. Argyrodite-Type Electrolyte Materials

Originating from two sources — the knowledge of the naturally occurring mineral Argyrodite (Ag_8GeS_6), first described in 1886,[53] and reports that Li_7PS_6 had been synthesized[3] — the first fully crystalline Li-based Argyrodites were synthesized and investigated with respect to their Li-ion conductivities in 2008 by Deiseroth *et al*.[6] The Argyrodite Li_7PS_6 consisting of Li, P and S only, at ambient temperature adopts the orthorhombic low temperature modification with space group *Pna21*. The characteristic structure for Argyrodite electrolytes is, however, the cubic high temperature modification (space group *F-43m*), which is stabilized by integrating a halogen component in the composition.

Materials with compositions Li_6PS_5X with X = Cl, Br or I can be considered as the typical Argyrodite electrolytes. Until recently, research on Li-ion conducting electrolytes was focused almost exclusively on such compositions, including materials with mixed halogen components.[54,55] Current follow-up investigations are concerned with the development of Argyrodite electrolytes containing semi/metal components as well.[6] Thus, taking Li_7PS_6 as a starting point for the research on true phosphorus-containing Argyrodites, three lines of development are approached: (i) halogen-based Argyrodites,[54–59] (ii) electrolytes based on halogen-containing materials with additional semi/metal components[60–62] and (iii) halogen-free Argyrodites based on Li, P, S and semi-metal[29,63] (Fig. 21). In addition to these lines, there is ongoing experimental work on phosphorous-free Argyrodite electrolytes based on Li, S and a semi/metal component.[44]

Alternative to the classification by the constitutive elements, the different types of Argyrodites can be described in terms of dopant strategies with respect to Li_7PS_5. According to this point of view, the Li_6PS_5X Argyrodites result from aliovalent doping of Li_7PS_5 by halogens replacing sulfur with concomitant charge compensation by the reduction of the lithium content. Integrating semi/metals follows different strategies, aliovalent doping with semi/metals for phosphorus balanced by corresponding increase in lithium to $Li_{7+x}M_xPS_6$ or aliovalent doping with semi/metals for lithium with a corresponding decrease in lithium content. In addition to these two approaches, mixed substitution concepts are under investigation as well.[63]

In recent approaches, combined application of halogen and semi/metal doping is applied. Thereby, the stoichiometry of the materials under investigation intends to replace phosphorus by the semi/metal and sulfur by the halogens along with an adjustment of lithium to balance the charges for both aliovalent dopants. A limiting condition for the dopant strategies is to maintain the cubic *F-43m* structure. In contrast to doping approaches for other materials, where the creation of vacancies or interstitials is the focus of strategy and analysis, creating disorder in the structure is a major objective of the dopant strategy in Argyrodites.

3.1. *Chemistry and phase relations of Argyrodites*

Li_7PS_6, the Argyrodite-structured electrolyte of the Li_2S:P_2S_5 type consists of these components in a 7:1 (or 87.5:12.5)

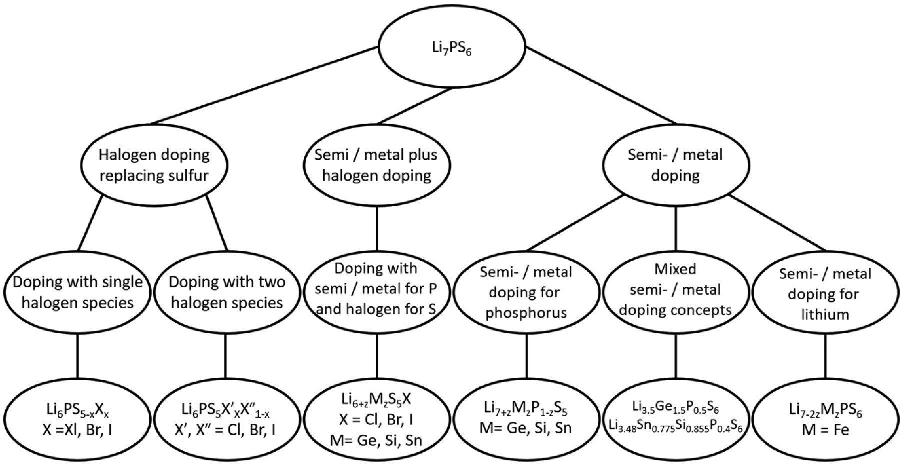

Fig. 21. Dopant strategies for Li-ion conducting Argyrodite-structured electrolytes.

ratio. Among the established structures in the Li_2S:P_2S_5 system, Li_7PS_6 has the highest relative content of Li_2S and is represented on the Li_2S–P_2S_5 tie line close to Li_2S in a Li_2S–P_2S_5–LiX ternary phase diagram (Fig. 22). Neighboring toward the more P_2S_5 rich side of the tie line are the Li-doped modifications of Li_3PS_4, the $Li_{3+x}P_{1-x}S_4$ electrolyte materials. Considering the sulfur and phosphorus contents in Li_7PS_6, its S:P ratio of 6:1 indicates that not all anionic species can be present in the form of ortho-thiophosphate tetrahedral moieties. The anionic species existent in Li_7PS_6 are isolated $PS_4{}^{3-}$ tetrahedra and free S^{2-} in a 1:2 ratio. There are two different crystallographic sites for the S^{2-} anion species.

These basic facts regarding the structure in combination with the ionic radii provide the base for the development of the different dopant strategies by halogens, semi/metals or combinations thereof. The ionic radii for the Li_7PS_6 and common halogen and semi/metal dopants for Argyrodite electrolytes are compiled in Table 3.

3.1.1. *Halogen-substituted Li_7PS_6–Li_6PS_5X (X = Cl, Br, I)*

Doping with halogens is typical for Argyrodite electrolytes. Argyrodite-structured Li_6PS_5X (X = Cl, Br, I), or in a more general form $Li_{7-z}PS_{6-z}X_z$, emerges from the aliovalent dopant approach according to which in Li_7PS_6 halogens replace part of the sulfur. The ionic radii of the halogen anions Br^-, Cl^- and I^- are similar to the S^{2-} ionic radius. Consequently, the halogens tend to replace the sites of free S^{2-} anions, although according to different patterns with respect to the crystallographic sites depending on the halogen species. The change in negative charge, from S^{2-} to X^-, is balanced by a reduction of Li^+ in the compositions. The properties of the halogen-substituted Li_6PS_5X crucially depend on the degree of disorder of S^{2-} and X^- between the crystallographic sites for the free sulfur anions.

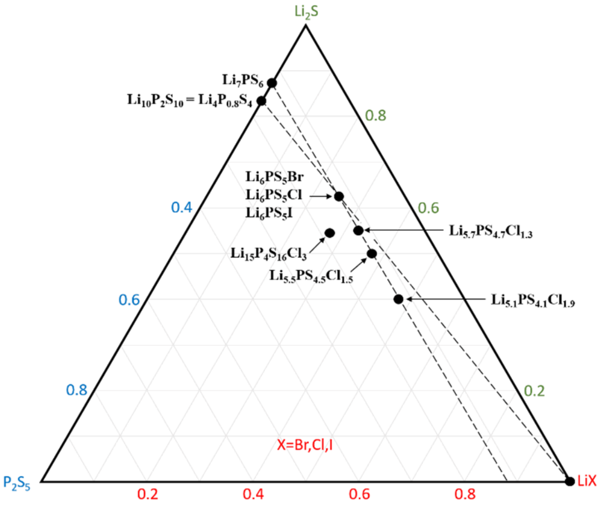

Fig. 22. Phase diagram Li_2S–P_2S_5–LiX (X = Br, Cl, I) showing halogen-doped Argyrodite materials Li_6PS_5X with tie line LiX to $Li_{10}P_2S_{10}$ (= $Li_4P_{0.8}S_4$) and the chlorine-doped $Li_{5.5}PS_{4.5}Cl_{1.5}$ at the solubility limit of the *F-43m* phase for halogens.

Table 3. Ionic radii for Li, P, S and common dopant ions for Argyrodite electrolytes.

Anion	Radius (Å)	Ref.	Cation	Radius (Å)	Ref.
S^{2-}	1.84	54	Li^+	0.59	29
Cl^-	1.81	54	P^{5+}	0.17	29
Br^-	1.95	54	Ge^{4+}	0.39	29
I^-	2.16	54	Si^{4+}	0.26	29
			Sn^{4+}	0.55	29

Halogen-doped Argyrodites Li_6PS_5Br, Li_6PS_5Cl and Li_6PS_5I consist of Li_2S, P_2S_5 and LiX in 5:1:2 ratio corresponding to their 0.625:0.125:0.25 constituent molar fractions. The structure also allows for a mixed halogen anion doping with contents summing up to 1 mole.[54,55] Variation of the chlorine anion content from 0.5 moles up to 1.5 moles Cl per formula unit, i.e. $Li_{5.5}PS_{4.5}Cl_{1.5}$ provides single-phase Argyrodite with cubic *F-43m* symmetry.[57,59]

Related to the corresponding ternary phase diagram, the design principle for halogen-type Argyrodites can be described by compositions with constant P_2S_5 fraction in which Li_2S is exchanged by LiX, while the sum of the fractions of these two components remains constant at 0.875. Li_6PS_5X is represented on a tie line from LiX to $Li_{10}P_2S_{10}$ in the phase diagram (Fig. 22). The latter material with 5:1 Li_2S:P_2S_5 ratio is one of the compositions ($x = 0.2$) for the Li-doped Li_3PS_4 series, $Li_{3+5x}P_{1-x}S_4$ ($Li_{10}P_2S_{10} = Li_4P_{0.8}S_4$).[24]

Neighboring the halogen-doped Argyrodites, that is when reducing the Li_2S content from 2.75 for $Li_{6.25}PS_{5.25}Cl_{0.75}$ ($z = 0.75$) to 1.5 (Li_2S:P_2S_5:LiCl ratios of 2.75:0.5:0.75 vs. 1.5:0.5:0.75), a new chlorothiophosphate structure with composition $Li_{3.25}PS_4Cl_{0.75}$ (= $Li_{15}P_4S_{16}Cl_3$) and space group *I-43d* was discovered.[64]

3.1.2. *Argyrodites based on Li, P, S and semi/metal*

The evaluation of aliovalent dopant effects by semi/metals in Li_7PS_6 is challenging. Considering the ionic radii of Ge^{4+} and Si^{4+} with $r = 0.39$ and 0.26, respectively, they may either occupy Li^+ ($r = 0.59$ Å) or P^{5+} ($r = 0.17$ Å) sites. From the structure analysis of LGPS, it is known that $GeS_4{}^{2-}$ and $SiS_4{}^{2-}$ tetrahedra are formed when the sulfur content is exceeding the amount required for the formation of $PS_4{}^{3-}$ tetrahedra.

Along with low dopant levels, the approach to replace part of the phosphorus by Ge or Si works quite well. The doping strategy includes a concomitant increase in lithium content in order to compensate for the reduction in positive charges emerging from the substitution of Ge^{4+} or Si^{4+} for P^{5+}. Electrolytes in the series of $Li_{7+x}M_xP_{1-x}S_6$ crystallize in *F43m* Argyrodite type for $0 \le x \le 0.4$ with a slight residual amount of Li_2S.[65] The phase with maximum semi/metal content in this series is $Li_{7.4}M_{0.4}P_{0.6}S_6$. The same concept applied to silicon doping also promotes high temperature Argyrodite majority phase formation. Within another approach investigating the $Li_{2z}SiP_2S_{7+z}$ series, where the Li_2S content was varied at constant silicon and phosphorus contents in the range of $5 \leq z \leq 14$, the compound with $Li_{22}SiP_2S_{18}$ ($z = 11$) composition is mainly *F-43m*-type material along with low content of secondary phases.[66] When normalized to S_6, the composition, which was denoted as $Li_{22}SiP_2S_{18}$ in the original paper, reads as $Li_{7.33}Si_{0.33}P_{0.66}S_6$. A comparison with the formula $Li_{7+x}M_xP_{1-x}S_6$ for $x = 0.33$ indicates that $Li_{7.33}Si_{0.33}P_{0.66}S_6$ is derived from the Li_7PS_6 composition, where silicon is replaced by phosphorus with charge compensation via additional lithium. Similar to the germanium-bearing phases, silicon is exclusively substituting phosphorus at low semi/metal content.

In a ternary $Li_2S–P_2S_5–GeS_2$ phase diagram, the electrolytes $Li_{7+x}M_xP_{1-x}S_6$ are on the tie line between Li_7PS_6 and Li_8GeS_6 (Fig. 23). However, the established Argyrodite compositions do not cover the complete scope and are limited to the Li_7PS_6-rich part only. Li_8GeS_6 itself, however, is not an Argyrodite instead it is a lithium thio-germanate.[46,67]

The site occupancy of the semi/metal components changes for the higher dopant concentrations. Inoue *et al*. explored materials based on Li_2S, P_2S_5 and GeS_2 in search for phosphosulfide Argyrodites by synthesizing a total of 17 compositions. This resulted in materials concentrated on or close to the tie line described by $Li_{7-4y}Ge_{3+y}PS_{12}$ in partial formation of Argyrodite (Fig. 24).[63] Most of them, however, contained substantial amounts of secondary phases. In materials with stoichiometries close to $Li_7Ge_3PS_{12}$, the secondary phase content is very low, thus this composition can be considered as an Argyrodite-type electrolyte.

Recalculating the underlying dopant concept results in Argyrodite structure from the stoichiometry of $Li_7Ge_3PS_{12}$ reveals that the stoichiometry intends to use a part of the Ge to replace phosphorus, while the other part is designed to substitute lithium. Considering the formula of $Li_7Ge_3PS_{12}$ normalized to S_6, $Li_{3.5}Ge_{1.5}P_{0.5}S_6$ or $(Li_{3.5}Ge)(Ge_{0.5}P_{0.5})S_6$, it is indicated that 0.5 moles of the Ge-dopant substitute phosphorus, while 1 mole of Ge^{4+} occupies lithium sites. The occupancy of 0.5 moles of Ge^{4+} on the P^{5+} sites corresponds well to the solubility limit indicated for the substitution pattern in the investigations of the Argyrodites with low dopant content.[65] The changes in the Li-content compared to Li_7PS_6 results from the charge balancing for the P^{5+} substitution which would increase the lithium content by 0.5 moles, and the charge compensation for the Li^+ substitution implies a decrease in lithium content by 4 moles per formula unit. Thus, at higher contents of Ge in the Argyrodites, there are two different doping mechanisms resulting in the substitution of Ge in both phosphorus and lithium sites.

The region for the Argyrodite-containing compositions is indicated in a ternary $Li_2S–P_2S_5–GeS_2$ phase diagram (Fig. 24). The fractions $Li_2S:P_2S_5:GeS_2$ for the Argyrodite $Li_7Ge_3P_2S_{12}$ ($Li_{3.5}Ge_{1.5}P_{0.5}S_6$) are 0.50:0.07:0.43. This composition is displayed in the ternary $Li_2S–P_2S_5–Ge_2S$ phase diagram on the $Li_7PS_6–GeS_2$ tie line with fractions 0.25:0.75 (Fig. 24).

Very recent work forwarded a novel type of phosphosulfide lithium conductor of the cubic Argyrodite type based on binary semi/metal components Sn and Si, resulting in electrolyte $Li_{6.96}Sn_{1.55}Si_{1.71}P_{0.8}S_{12}$.[29] Summing up the semi/metal

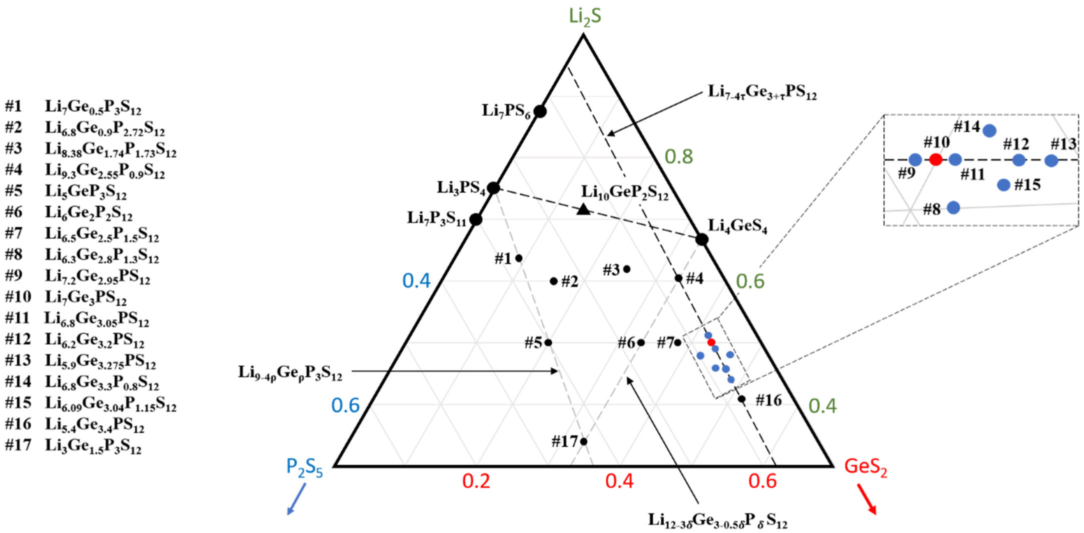

Fig. 23. Ternary $Li_2S–P_2S_5–GeS_2$ phase diagram indicating the regions for Argyrodite-containing compositions (blue symbols) as opposed to compositions where no formation of Argyrodite is observed (black symbols). The position of $Li_7Ge_3P_2S_{12}$ is indicated by the red symbol. Stoichiometric ratios calculated from Table 1 from Inoue *et al*.[60]

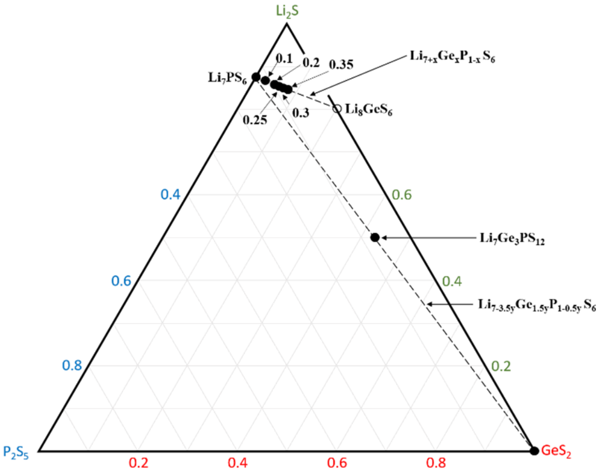

Fig. 24. Ternary Li_2S–P_2S_5–GeS_2 phase diagram indicating the two substantially different regions for Ge-stabilized Argyrodites.

content and normalizing to S_6, the stoichiometry for $Li_{6.96}Sn_{1.55}Si_{1.71}P_{0.8}S_{12}$ can be given as $Li_{3.48}Sn_{0.775}Si_{0.855}P_{0.4}S_6$ or $Li_{3.48}M_{1.63}P_{0.4}S_6$, which is close to, but not identical to the stoichiometry of the Ge-based $Li_{3.5}Ge_{1.5}P_{0.5}S_6$ ($Li_7Ge_3PS_{12}$) electrolyte. In contrast to the latter material, in $Li_{3.48}M_{1.63}P_{0.4}S_6$, the total semi/metal fraction is higher. Moreover, the concept with respect to the distribution of the semi/metal on Ge- and P-sites is different from that prevailing in $Li_{3.5}Ge_{1.5}P_{0.5}S_6$ ($Li_7Ge_3PS_{12}$). While in the Ge-doped material, the fraction of Ge on P-sites is 0.33 (corresponding to a ratio between Ge on P vs. Ge on Li sites of 0.5:1). A higher fraction of 0.37 for Si/Sn on P-sites is realized in the $Li_{3.48}Sn_{0.775}Si_{0.855}P_{0.4}S_6$ electrolyte. The fractions Li_2S:P_2S_5:MS_2 ($M = Sn_{0.475}Si_{0.525}S_2$ or GeS_2) are 0.487:0.056:0.457 compared to fractions 0.50:0.07:0.43 for the germanium-based Argyrodite $Li_7Ge_3P_2S_{12}$. Considering the differences in ionic radii between Ge^{4+} vs. Si^{4+} and Sn^{4+}, slightly different stoichiometry is required for matching the stabilization of the high temperature Argyrodite phase. However, the general substitution pattern according to which part of the semi/metal substitutes for phosphorus and another part for lithium when doping with semi/metals at higher dopant levels also holds for this material.

A doping strategy to yield high temperature Argyrodite electrolytes along with exclusive substitution of the dopant for lithium is not established for Ge and Si but applied in case of iron (Fe^{2+}) as dopant.[68] Subject of investigations was iron-doping of Li_7PS_6 along with the reduction in lithium accounting for charge balance according to $Li_{7-2x}Fe_xPS_6$, specifically for $x = 0.5$, $Li_6Fe_{0.5}PS_6$. While in the semi/metal dopant strategies replacing phosphorus and the mixed-site semi/metal dopant approaches, occupancy of lithium sites is exceeding the occupancy in Li_7PS_6. In doping approaches replacing Li^+ by higher valent (Fe^{2+}) cations, the site occupancy is reduced. Consequently, there will be vacancies on lithium sites. Along with this strategy $Li_6Fe_{0.5}PS_6$ crystallizes in cubic *F-43m* Argyrodite structure. Thus, although along with a different species of dopant, doping with metals on the lithium site is also an option for the modification of Li_7PS_6 that may lead to the stabilization of the high temperature Argyrodite structure.

In summary, depending on the type of semi/metal and the dopant level, the site occupancy of the semi/metal can be on phosphorus, on lithium sites or in a configuration mixed on both sites. While the first case applies to Ge- and Si-doping at low levels, the third configuration is gathered at higher dopant levels for these elements. An exclusive occupation of the lithium sites by the dopant in the Argyrodite structure is realized when doping with 0.5 moles of iron.

3.1.3. *Phosphorous-free electrolytes based on Li, S and a semi/metal component*

Argyrodite-structured Li-conducting electrolytes also form within the Li_4SiS_4–Li_5AlS_4 binary system. Examination of these phosphorus-free electrolyte materials along the

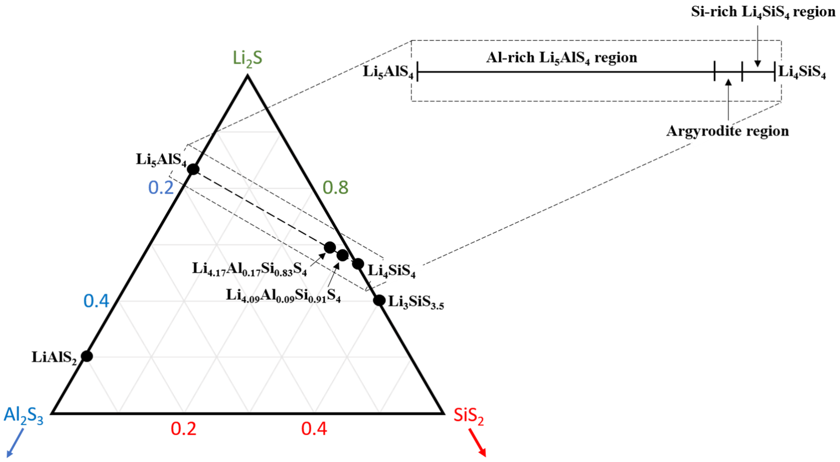

Fig. 25. Ternary Li_2S–Al_2S_3–SiS_2 phase diagram indicating the regions for thio-LiSICon-type Li_4SiS_4 and Li_5AlS_4 and Argyrodite-type materials.

Li_4SiS_4–Li_5AlS_4 tie line in a Li_2S–SiS_2–Al_2S_3 phase diagram with general stoichiometry $Li_{4+x}Si_{1-x}Al_xS_4$ revealed a region with Argyrodite-type materials, which is located close to the Li_2S–SiS_2 axis in this diagram (Fig. 25).[44] Along the complete Li_4SiS_4–Li_5AlS_4 tie-line, three regions were identified. The Argyrodite region extends over a very narrow range around $Li_{4.1}Si_{0.9}Al_{0.1}S_4$ from ($0.09 \le x \le 0.17$), while Li_5AlS_4-type materials are formed for $0.3 \le x \le 0.8$ and in the Si-rich region, synthesis results in thio-LiSICon Li_4SiS_4.

3.1.4. *Halogen-containing Argyrodites with additional semi/metal components*

A quite recent approach for synthesis of *F-43m* Argyrodites is the combined doping of Li_7PS_6 by halogens and semi/metals. Till date, the investigations focused on compositions with 1 mole halogen substituting sulfur in Li_7PS_6 along with semi/metal doping at varying contents and concomitant balancing of the charges by adjustment of the lithium content according to $Li_{6+y}M_yP_{1-y}S_5X$ (M = Ge, Si, Sn).[55,61,62] Thereby, as indicated by the stoichiometry, the amounts of semi/metal dopant are kept low enough to remain within the solubility limit for these elements on the phosphorus site. Combination of Si and Br dopants $Li_{6+y}Si_yP_{1-y}S_5Br$ with Si-contents[10] up to $x = 0.35$ results in a *F-43m* major phase along with secondary phases contents less than 3% of Li_3OBr and LiBr. However, attempts to incorporate germanium into Li_6PS_5Br are not successful so far.[61]

In contrast, all of the most common semi/metal dopants for phosphosulfides, M (M= Ge, Sn, and Si), form Argyrodite-type solid solutions with the iodine-doped material $Li_{6+y}M_yP_{1-y}S_5I$.[60,62] The solubility behavior is different for Ge, Sn and Si. While the solubility for Ge^{4+} in the P^{5+} position is up to $y = 0.8$, whereas for Sn^{4+}, the solubility is limited to $y = 0.2$ only. For Si^{4+}, it is difficult to determine a distinct limit for its solubility, the incorporation of Si in the $Li_{6+y}Si_yP_{1-y}S_5I$ lattice seems to be ongoing along with secondary phase formation up to more than a content of $y = 0.5$ Si. The changes in properties and performance along with doping are larger for the iodine-based Argyrodites than for the bromine material.

3.2. *Argyrodite structure*

The naturally occurring mineral Argyrodite (Ag_8GeS_6) and its structure were first described in 1886.[53] The phosphosulfide Argyrodite Li_7PS_6 crystallizes in an orthorhombic space group *Pna2₁* or a cubic space group *F-43m* depending on temperature.[10] The phase transition temperature between the low temperature *Pna2₁* and the high temperature *F-43m* is ~210°C. The structural building blocks of the anionic framework are isolated ortho-thiophosphate PS_4^{3-} tetrahedra and S^{2-} anions with a ratio of 1:2.[45] In the *F-43m* structure (Z = 4), the PS_4^{3-} tetrahedra, with P in 4b and S in 16e position, are in the unit cell-center and in the middle of all 12 edges. These positions correspond to octahedral voids of the cubic face-centered anion lattice formed by the S^{2-} in 4a sites. The other part of the S^{2-} anions is located in tetrahedral voids at 4d positions. There are two distinct positions for the lithium, 24g and 48h. The lattice parameter of Li_7PS_6 *F-43m* phase is $a = 9.993$ Å at 230°C.[10] Considering the structure from another point of view, the 16e sulfur in the PS_4^{3-} tetrahedra forms the first, the S^{2-} free sulfur on 4d forms the second, and the free sulfur on 4d forms the third sulfur coordination sphere for the phosphorus (Fig. 26).

3.2.1. *Halogen-substituted Li_7PS_6–Li_6PS_5X (X = Cl, Br, I)*

The halogen-doped phosphosulfides are stable in the high temperature *F-43m* phase at ambient temperature. The halogen anions Cl^-, Br^- or I^- occupy the free sulfur positions. However, depending on the halogen-nature, they settle into different crystallographic sites. Chlorine and bromine are distributed over the 4a and 4d positions, whereas iodine is located exclusively in the 4a position. The distribution of the halogens over the sites, in particular the ordering of the anion sub-lattice for I^- doped vs. the disordered sub-lattices for Cl^- and Br^- doped Argyrodites, has far-reaching consequences for the properties of the materials. This is due to the fact that disorder induced softening of the lattice plays a major role

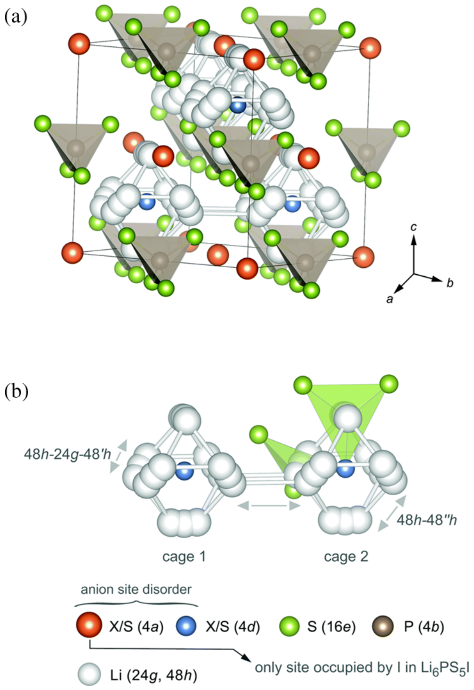

Fig. 26. Crystal structure of cubic Argyrodite showing (a) the unit cell (*Z* = 4) and (b) local arrangement of lithium-forming polyhedral centered by S (4d). Reproduced from Ref. 54 with permission from the Royal Society of Chemistry © 2019.

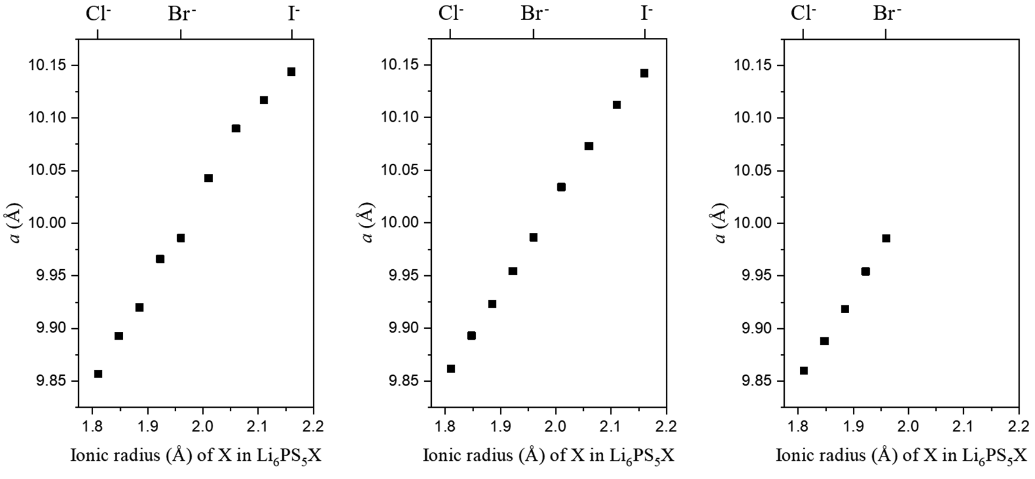

(a) (b) (c)

Fig. 27. Lattice parameters of Li_6PS_5X with X = Cl, Br I and mixtures thereof vs. mean ionic radius of the halogen anions. (a) plotted from data from Hanghofer *et al*.[51] (b) plotted from data from Kraft *et al*.[52] (c) plotted from data from Zhou *et al*.[48]

for the Li-ion transport properties of the material. While the ionic radii of Cl^- 1.81 Å and Br^- 1.95 Å are relatively close to the radius of S^{2-} (1.84 Å), the ionic radius for I^- is substantially larger (2.16 Å). Thus, the iodine does not dwell on the Li-cage instead is limited to the 4a position.[54]

The lattice constants are also substantially influenced by the type of halogen dopant. The lattice parameter for the Argyrodites doped with a single halogen species at a dopant content of one mole increases with the ionic radius of Cl^-, Br^- and L^- from 9.857 Å for Li_6PS_5Cl over 9.986 Å for Li_6PS_5Br to 10.145 Å for Li_6PS_5I, respectively. The phosphosulfide Argyrodites with mixed halogen content of 1 mole in total also match pretty well into this scheme (Fig. 27).[51,54,55] Moreover, lattice parameters from liquid phase synthesized $Li_6PS_5Cl_xBr_{1-x}$ are highly similar to those for solid-state synthesized material.[51]

Along with higher halogen content in $Li_{7-x}PS_{6-x}Cl_x$, the site occupancies for Cl^- are increasing. Thereby, the additional Cl^- distributes to both 4a and 4d sites. Compared to Li_6PS_5Cl in $Li_{5.5}PS_{4.5}Cl_{1.5}$, the occupancy on 4a site by Cl^- is enhanced from 0.385 to 0.615, the fraction of Cl^- on the 4d site rises from 0.615 to 0.835, both coupled with a corresponding reduction in S^{2-} occupancy of the respective sites.[55,57] The difference in ionic radii of Cl^- vs. to S^{2-} is small, therefore, the decrease in lattice parameter from 9.8598(4) Å for Li_6PS_5Cl to 9.8061(1) Å for $Li_{5.5}PS_{4.5}Cl_{1.5}$ is in most part due to the Li^+ vacancies.[57]

3.2.2. *Argyrodites based on Li, P, S and semi/metal*

Doping with semi/metals also stabilizes the cubic high temperature Argyrodite phase. The analysis of the influence of semi/metal doping has to at first take the site occupancy of the dopant into account. At low concentrations of germanium and silicon, these dopants substitute exclusively for phosphorus. With dopant contents of 0.25 moles Ge or Si, corresponding to $Li_{7.25}Ge_{0.25}P_{0.75}S_6$ and $Li_{7.25}Si_{0.25}P_{0.75}S_6$, the lattice parameters are $a = 9.9543(1)$ Å and $a = 9.9461(1)$ Å, respectively.[65] Lattice parameters for both, measured at ambient temperature, are smaller than the lattice parameter given for the high temperature Li_7PS_6 phase, however, the parameters for Li_7PS_6 was determined at 230°C.[10] Thus, this comparison does not provide the full picture on the impact of the semimetal doping.

However, consideration of the compositional range from 0.1 moles to 0.35 moles of Si and Ge indicates that along with increasing dopant content the lattice parameter increases, and for a given dopant content, the lattice parameter along with Ge-doping is larger than that for Si-doping.[65] As the ionic radii of both, Ge^{4+} and Si^{4+} are larger than the P^{5+} radius, it supports the trend of the lattice parameters in this series. At higher dopant occupancies, and concomitant to that, the influence of the semi/metal doping becomes different from the trends observed for the low-level dopant content. The mixed site occupancy with Ge substituting P^{5+} and Li^+ can be derived from the analysis of the stoichiometry of $Li_7Ge_3PS_{12}$ and is also confirmed by structural analysis. The structure of this material is cubic. Refinements revealed that Ge occupies 4b sites in the center of the $(Ge/P)S_4$ tetrahedra. With respect to the other part of the germanium substitution, it is confirmed by the structural analysis that it is also distributed within the 48h sites, with Li and Ge occupation of 0.42 and 0.08, respectively. Analysis of the lattice parameter with respect to the ionic radii reveals that there are counteracting effects of the replacement in the two sites. Substitution of Ge for P (0.39 Å vs. 0.17 Å) tends to increase the lattice parameter whereas substitution of Ge for Li reduces the lattice parameter. Overall, the substitution pattern results in a relatively small lattice parameter $a = 9.78525(5)$ Å.

In the cubic Argyrodite-type $Li_{6.96}Sn_{1.55}Si_{1.71}P_{0.8}S_{12}$, the lattice constant is $a = 9.842074(18)$ Å, which is also much smaller than those of the low-doped semi/metal bearing materials. Similar to $Li_7Ge_3PS_{12}$, the semi/metal dopants occupy in part P^{5+}, and partially Li^+ sites. Due to the mixed cation composition, the site occupancy is even more complex in the former material, however, owing to the very similar ionic radii of Li^+ (0.59 Å) and Sn^{4+} (0.55 Å), the Sn fraction of the dopant is likely to occupy preferably the lithium sites.[29]

3.2.3. *Halogen-containing Argyrodites with additional semi/metal components*

A very recent approach to phosphosulfide electrolytes with high-temperature Argyrodite structure is co-doping Li_7PS_6 with halogens and semi/metal. Research in these materials has so far focused on the compositions $Li_{6+x}P_{1-x}M_xS_5X$ with semi/metal contents below their solubility limits on the P^{5+} (4b) site and 1 molar doping by halogens.[60–62] There is a different impact from the semi/metal co-dopant depending on the type of halogen dopant. On doping the phosphosulfide Argyrodite with I^- only, an ordered lattice with exclusive site occupancy on S^{2-} (4a) sites by the iodine is formed. The co-doping of Li_6PS_5I induces structural disorder in terms of the occupancy of the free sulfur S^{2-} positions by the iodine. Starting from co-dopant levels of 0.2 moles tin or germanium approximately, the iodine is no longer limited to lattice position onto the S^{2-} (4a) site, but distributes between S^{2-} (4a) and S^{2-} (4d) positions (Fig. 28(a)). The disorder induced by the formation of $GeS_4{}^{2-}$ or $SnS_4{}^{2-}$ tetrahedra enables partial exchange of sulfur and iodine between the 4a and the 4d sites, thus generating further disorder in the structure $Li_{6+x}P_{1-x}M_xS_5I$ with concomitant softening of the lattice.

Substitution of all three major tetravalent dopant ions for phosphosulfides, Ge^{4+}, Si^{4+} and Sn^{4+}, leads to a pronounced increase in the lattice parameters of $Li_{6+x}P_{1-x}M_xS_5I$ (Fig. 28(b)). This increase scales with the ionic radius of the dopant ion. The plateaus for the increase in lattice parameters with dopant content indicate the solubility limits of 0.8 moles for Ge and 0.3 moles for Sn. In the case of Si, no distinct plateau can be identified. In this material, the lattice parameters for Si-contents higher than 0.3 moles increase further, which is interpreted to indicate, that part of, but not all silicon is integrated in the lattice and concomitant formation of secondary phases occurs. Overall, along with the co-doping approach, there are two co-acting factors of influence from the differences in ionic radii between dopants I^- and Si^{4+} and hosting ions S^{2-} and P^{5+} leading to an increase in lattice spacing. The widening in combination with the disorder-induced softening of the lattice thus merging two of the dopant strategies for Argyrodites to enhance the mobility of Li-ions in the lattice.

Although from a stoichiometry point of view, the doping of Li_6PS_5I and Li_6PS_5Br with Si is analogous, the impact on the structure is different. In the dopant-free Li_6PS_5I, the free S^{2-} and the I^- anions are exclusively on the 4d and 4a sites, respectively.[54] The substitution of phosphorous by silicon induces major disorder distributing both anions on both sites, amounting to a 4d site occupancy of the I^- anions up to 12% at a Si-content of 0.5 moles. In contrast, substantial site disorder is already present in the semi/metal free Li_6PS_5Br wherein the site disorder Br^-/S^{2-} is 22%.[55,62] In this material, there are only minor effects from doping with silicon on the site disorder.[61]

However, Si-doping in $Li_{6+x}P_{1-x}Si_xS_5Br$ leads to an increase in the lattice parameter that is more pronounced than that for $Li_{6+x}P_{1-x}Si_xS_5I$ (Fig. 29). The lattice spacing of

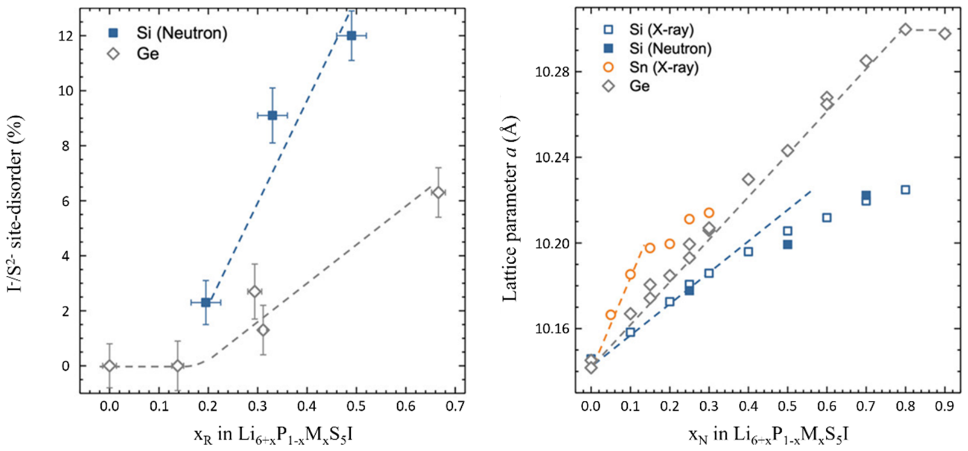

(a) (b)

Fig. 28. (a) Site disorder (occupancy of 4a sites by iodine anions in terms of the ratio I^-/S^{2-} on 4a sites for $Li_{6+x}P_{1-x}M_xS_5I$ (M = Ge, Si). (b) Lattice parameters of the cubic *F-43m* Argyrodites $Li_{6+x}P_{1-x}M_xS_5I$ (M = Ge, Si, Sn) depending on dopant content. Reprinted with permission from Ref. 62. Copyright © 2019 American Chemical Society.

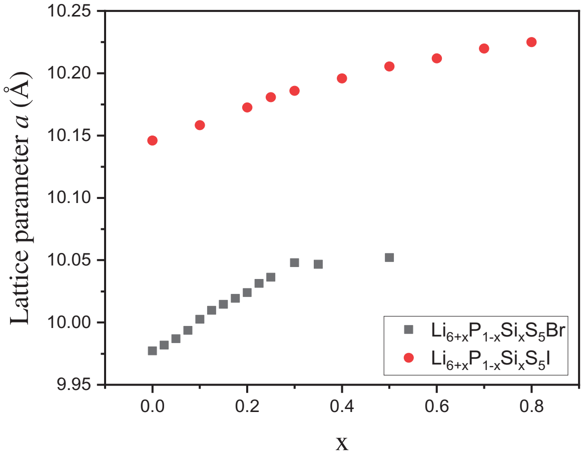

Fig. 29. Lattice parameters of the cubic *F-43m* Argyrodites $Li_{6+x}P_{1-x}Si_xS_5$-Br[61] and $Li_{6+x}P_{1-x}Si_xS_5I$.[62]

$Li_{6+x}P_{1-x}Si_xS_5Br$ increases from 9.975 Å for Li_6PS_5Br with Si-content up to its solubility limit of 0.35 moles to 10.05 Å for $Li_{6.3}P_{0.7}Si_{0.3}S_5Br$ by ≈ 0.075 Å. The same amount of Si-doping in $Li_{6+x}P_{1-x}Si_xS_5I$ effects cause an increase of the lattice parameter on ≈ 0.05 Å. Impact from Si-doping on the properties for the Br-based $Li_{6+x}P_{1-x}Si_xS_5Br$ can maybe attributed to the enhanced Li-ion content in the 24g site or the widening of the lattice parameters.[61]

3.3. *Argyrodite processing*

Considerable research activity is ongoing related to the processing of Argyrodite phosphosulfide electrolytes. Thereby, in particular with respect to the halogen-based materials, both, solid-state routes and liquid-phase synthesis are subject to current investigations and development.

For solid-state processes, as for most other phosphosulfide electrolyte materials, educts are Li_2S, P_2S_5 with addition of lithium-halides LiBr, LiCl and LiI as source for the halogen component, respectively. The two essential steps of the solid-state route must be carried out in an inert environment due to the sensitivity of the materials. Thereby, the process parameters for both steps, the homogenizing and grinding the starting materials via ball-milling and the subsequent heat-treatment of the mixtures at elevated temperatures have to be matched to each other.

Considering heat-treatment and milling conditions, there are two strategies for obtaining phase pure materials. On the one hand, mixing or very moderate milling conditions coupled with relatively high temperatures and very long times for the heat treatment are applied in order to obtain phase pure materials.[6,69,70] Mixing of the educts followed by a heat treatment at 550°C/168 h or 1 h ball milling at 110 rpm can be combined with a heat treatment at 550°C/10 h result in phase pure materials.[6,70] On the other hand Argyrodites can also be obtained by intense ball milling with subsequent heat treatment at lower temperatures or reduced dwell times. Along with ball milling at 500 rpm for 8 h, Li_6PS_5Br and Li_6PS_5I were prepared at 300°C and 350°C with dwell times 5 h and 15 h, respectively.[58,70] However, even with intense ball milling under optimized conditions at 700 rpm, a minimum heat treatment temperature of 500°C is needed.[59]

Most important, however, are the cooling rates, which prove to be relevant for the degree of disorder of site-disorder on the 4a and 4d sites, which in turn is considered to be a main factor of influence on the conductivity.[71,72] Analysis of Li_6PS_5Br synthesized at 550°C/30 min, slow cooled and reheated subsequently to temperatures of 350–550°C and quenched thereafter to freeze the high temperature state, indicated a systematic trend of the disorder parameter (Fig. 30(a)). Right after the first slow cooling from 500°C/30 min step, the materials show an almost ordered structure with 10% disorder. Increasing disorder is generated by the second step heat treatments. The degree of disorder increases with temperature and amounts up to 39% after the heating step to 550°C. Concomitant with the increase in disorder, there are changes in the lithium substructure and a decrease in the lattice parameter.[72]

Considering common processing temperatures at 550°C for Li_6PS_5Br, Li_6PS_5Cl and Li_6PS_5I, the aggregate state of the materials during processing might be different depending on the type of halogen. Assuming that the P_2S_5 reacts readily with Li_2S during the milling procedure or at relatively low temperature to form Li_3PS_4, this intermediate is in solid state up to 700°C.[19] So, conditions for a true solid-state reaction might be given by the melting points of the lithium-halides. While the melting point for LiBr is at 550°C, Lil melts at 489°C, thus at considerably lower temperature, whereas LiCl with a melting temperature of 650°C is in solid state at a 550°C heat treatment (Fig. 30(b)). Analysis of the reaction conditions with respect to liquid-phase formation might be an approach for further understanding of the product properties.

Considerably higher processing temperatures than those used for the halogen-type Argyrodites have to be applied on of Al-stabilized Argyrodite electrolytes. The melt quenching route for preparation of $Li_{4+x}Al_xSi_{1-x}S_4$ included two temperature steps after vibration mixing at 370 rpm for 30 min, in which the first temperature step was at 1000°C with 5 h dwell time. Following ice water quench, the material was then regrounded and subjected to a final heat treatment at 200°C for 10 h.[44] Heating at 870°C for 8 h was applied for the synthesis of $Li_7Ge_3PS_{12}$.[63] In contrast, the process temperatures for Argyrodites with tin and silicon as the stabilizing elements $Li_{6.96}Sn_{1.55}Si_{1.71}P_{0.8}S_{12}$ are much more moderate in the same temperature range as for the halogen-based Argyrodites. After 380 rpm ball milling for 40 h, heat treatment of appropriate mixtures of Li_2S, P_2S_5, SiS_2 and SnS_2 at 500°C for 5 h

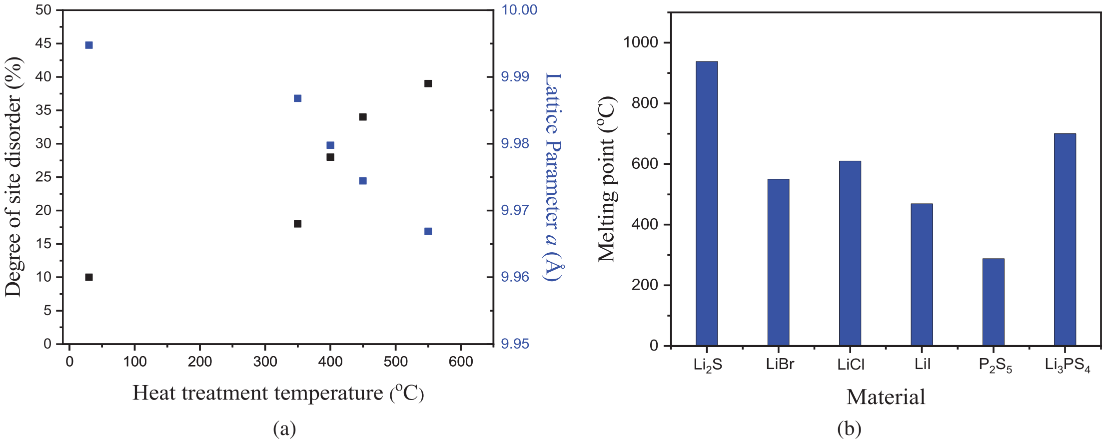

Fig. 30. (a) Degree of site disorder on 4a and 4d sites and lattice parameter for Li_6PS_5Br depending on quenching temperature.[71,72] (b) Melting points of reactants and intermediates for various halogen-stabilized Argyrodite synthesis.

was sufficient to provide phase pure Argyrodite-structured electrolytes.[29]

Liquid-phase synthesis of halogen-based materials is facing the challenge to meet simultaneously the solubility, the stability, the solvent complexation and the crystallization of the three reactants Li_2S, P_2S_5 and the halogenides LiBr, LiCl or LiI, respectively.[16] In particular, solvents that are capable to form PS_4^{3-} to initiate the reaction do mostly not allow for co-crystallization of S^{2-} and halogen anions. On the other hand, solvents suitable for co-crystallization of these anions in many cases tend to react with the precursors. An approach to address these issues is, in the first instance, to use a two-step procedure, as applied for the synthesis Li_6PS_5Br. Thereby in the first step, Li_2S and P_2S_5 are reacted in tetrahydrofuran (THF) to form Li_3PS_4-THF complexes. The product of this reaction is then further reacted with Li_2S and LiBr in ethanol (EtOH).[73]

The same process methodology was applied to synthesize Li_6PS_5Cl, Li_6PS_5I and $Li_{6-y}PS_{5-y}Cl_{1+y}$.[51] By means of an alternative approach with sequential addition of the reactants, Li_6PS_5Cl was prepared by first mixing and stirring Li_2S and LiCl, and then subsequently adding P_2S_5 using ethyl acetate (EA) as a solvent.[74] The synthesis resulted in 20–30 μm sized particles with rod-like morphology composed of nanosized subparticles. In a third type of approach, EP was used as the solvent while the reaction was supported by ultrasonication to synthesize Li_6PS_5Br from Li_2S, P_2S_5 and LiBr powders. The ultrasonication promotes the reaction between Li_2S and P_2S_5 to form PS_4^{3-} unit and results in α-Li_3PS_4 precursor. By means of addition of ethanol to the white suspension, the α-Li_3PS_4 precursor, Li_2S and LiBr dissolve to PS_4^{3-}, Li^+, S^{2-} and Br^- ion species. Li_6PS_5Br precipitates on heat treatment by evaporation of EP-ethanol solvent.[75]

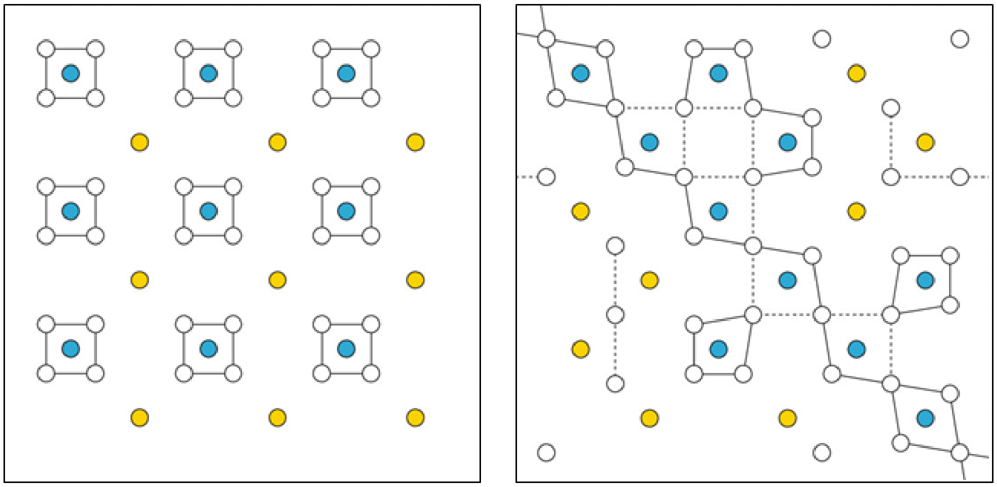
(a)
(b)

Fig. 31. Relations between configurational order/disorder of the anion substructure and static order/disorder of the Li sites: (a) ordered anion substructure and (b) disordered anion substructure. In the ordered substructure, the Li sites move toward S^{2-} (blue) and away from X^- (yellow) anions resulting in an ordered nonpercolating network of short site–site distances. In the disordered substructure, the movement of the Li-sites toward S^{2-} and away from X^- forms a percolating network of short site–site distances. Reprinted with permission from Ref. 78. Copyright © 2021 American Chemical Society.[78]

3.4. *Argyrodite conductivity*

Among the modifications of the Argyrodites, particularly the high temperature cubic modification with space group *F-43m* is considered favorable for Li-ionic conductivity. Extensive investigations have been carried out on the main factors of influence and the mechanisms for Li-ion conduction in the prototype Argyrodite materials Li_6PS_5X (X = Cl, Br, I), that is materials that were stabilized in the *F-43m* structure by substitution of sulfur by halogens. In these materials, the Li-ion conductivity is related to Li vacancies emerging from reduced Li-content and, in particular, to the X^-/S^{2-} anion disorder, which in turn modulates the lithium substructure.[76,77] In anion-ordered systems, Li-ions form cage-like substructures with inactive critical site–site pathways and lithium motion is largely restricted within these structures (Fig. 31(a)). In contrast, in anion-disordered systems, modified Li-positions result in delocalized Li-density and activation of site–site pathways, thus forming a percolating three-dimensional diffusion network (Fig. 31(b)).[77,78] Much less is known about the Li-transport mechanisms in semi/metal-based Argyrodites.

According to the different types of elements for stabilizing the *F-43m* structure in the Argyrodite, the discussion of the conductivity is grouped into three sections; halogen-based Argyrodites, semi/metal-based Argyrodites and Argyrodites in which combined semi/metal and halogen substitution provides the presence of the cubic structure. The section is concluded with a comparison of the results for the Li-ion conductivities with respect to the different dopants.

3.4.1. *Halogen-based Argyrodites*

Direct comparison of results for 1 mole halogen content: Chlorine, bromine and iodine are suitable to stabilize the cubic *F-43m* structure when substituted sulfur in a Li_7PS_6 Argyrodite framework. The analysis of similarities and differences that leads to the specific Li-ion conductivities for each of the materials have been the subject of many investigations. Research work mostly focused on a one molar content of the halogens, i.e. compositions of Li_6PS_5X with X = Cl, Br, I as well as modifications thereof via mixed-halogen doping. Experimental work dedicated to comparison of Li-ion conductivities depending on the type of halogens used for the doping evidenced high Li-ion conductivities in the range 10^{-3} S/cm for Li_6PS_5Br and Li_6PS_5Cl and some orders of magnitude lower Li-ion conductivity for Li_6PS_5l (Table 4).

The starting point for analyzing the differences in Li-ion conductivity for Br, and Cl vs. I based Argyrodites are the differences in structure related to the X^-/S^{2-} disorder on the 4c site. Disorder leads to Li-substructures to be modified in a way that favors the intercage jumps of the Li-ions which are necessary for its long range transport. The degree of disorder scales with the ionic radii of the halogen ionic species.

Table 4. Ambient temperature Li-ion conductivity for Li_6PS_5X (X = Cl, Br, I) — The table contains only those results in which Argyrodites with all three halogens Cl, Br and I were prepared by the same research group with the same synthetic method.

σ (mS/cm)				
X = Cl	X = Br	X = I	Synthesis method	Ref.
3.4	2.2	0. 00107		54
1.8	1.3	0.015	SS, Li_2S-excess	79
0.74	0.72	0.00046	Annealed	80
2.0	1.1	0.0012		55
0.34	0.31	0.029	Liquid phase	81
0.95	0.82	0.37	Mechanical mill	73

Concomitant to the influence on disorder and Li-substructure, the type of halogen ion impacts also the lattice volume, which increases the intercage jump distances.[55] The combined effects of disorder and lattice spacing result in a modified Li-substructure with flattened energy landscape. The substructures are described in part of the investigations by differences in the occupation of specific Li-positions,[6,76,82] while another part emphasizes the inhomogeneous distribution of local anionic charge, and the resulting spatially diffuse lithium distributions.[77,78] Corresponding to the degree of disorder and its implications, the Li-ion conductivity decreases in the order $Li_6PS_5Cl \rightarrow Li_6PS_5Br \rightarrow Li_6PS_5I$.

Further evidence for the high degree of order being the limiting factor for the Li-ion conductivity in Li_6PS_5l when prepared by conventional processing is provided by experiments introducing structural disorder in these materials by means of post-preparation high energy ball milling. Applying this approach to initially microcrystalline Li_6PS_5l prepared by a solid-state route results in a structurally distorted material with a ambient temperature Li-ion conductivity of 0.5×10^{-3} S/cm, which is two orders of magnitude higher than that of the original microcrystalline material.[83] Similarly, kinetic freezing of the site disorder in Li_6PS_5Br by quenching after heat treatment leads to an enhancement of conductivities compared to the slow- and standard-cooled material by approximately a factor of 2.[71]

Mixed halogens with cation radius as parameter: The trend that chlorine promotes the Li-ion conductivity the most, while iodine leads to low Li-ion conductivity, maintains also for Argyrodites with mixed halogen doping with conductivity scaling inversely to halogen anion radii (Fig. 32(a)). Comparisons addressing a total halogen content of 1 mole demonstrate the effects of the different halogen species and mixtures thereof. The Li-ion conductivities are correlated to the X^-/S^{2-} site disorder and scale inversely with the lattice parameter (Fig. 32(b)).

Li-conductivity depending on the halogen content: Considering the range for the halogen contents providing Argyrodites in the *F-43m* structure, investigations of

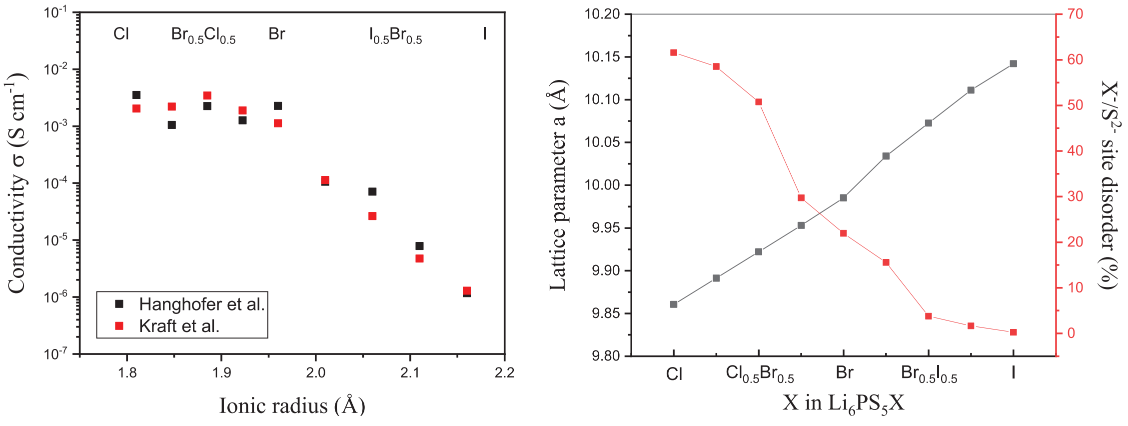

(a)

(b)

Fig. 32. (a) Ambient temperature Li-ion conductivity for Argyrodites stabilized by halogens with an overall halogen content of 1 mole.[54,55] (b) Lattice parameters and disorder parameters for the 1 mole halogen stabilized Argyrodites.[55]

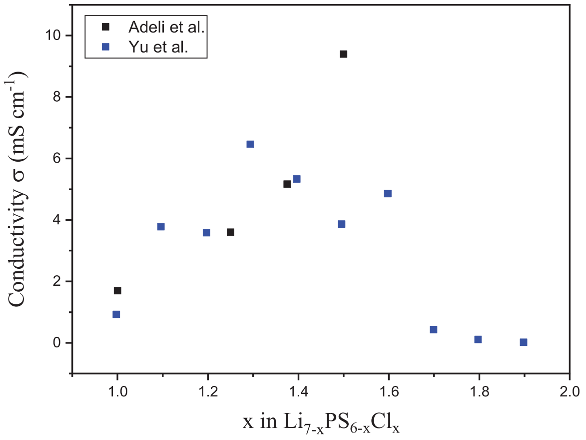

Fig. 33. Li-ion conductivities of $Li_{7-x}PS_{6-x}Cl_x$ depending on x for chlorine contents higher than 1 mol.[57,58]

Cl-substituted Argyrodites demonstrated a lower bound of at least 0.5 moles to be sufficient to stabilize the high temperature modification.[59] However, the most interesting with respect to high Li-ion conductivities in $Li_{7-x}PS_{6-x}X_x$ is the range with halogen contents $1 < x < 2$. In Cl-doped Argyrodite, along with the chlorine content moderately exceeding 1 mole per formula unit, the Li-ion conductivities are enhanced up to almost an order of magnitude compared to Li_6PS_5Cl (Fig. 33). A maximum ambient temperature Li-ion conductivity amounting up to 9×10^{-3} S/cm and 6×10^{-3} S/cm, respectively, were identified at $x = 1.5$[57] and $x = 1.3$.[58]

3.4.2. *Semimetal-stabilized Argyrodites*

The conductivities of the semi/metal stabilized Argyrodites face different conditions with respect to the structural surroundings depending on the semi/metal content in the electrolytes. At low Si^{4+} or Ge^{4+} content, these ions substitute for phosphorus P^{5+}, form SiP_4^{3-} or GeP_4^{3-} tetrahedra contributing to the anion framework while the Li^+ content is enhanced compared to nonmodified Li_7PS_6. In contrast, for higher semi/metal content, part of the semi/metal occupies Li^+ sites along with reduced lithium content.

The doping approach to replace phosphorus by semi/metals stabilizes the cubic phase that already occurs at small amounts of semi/metals and provides ambient temperature Li-ion conductivities in the range of $1–2 \times 10^{-3}$ S/cm.[65] The highest ambient temperature Li-ion conductivities among these electrolytes are realized by Ge-doping according to $Li_{7+x}Ge_xP_{1-x}S_6$ at contents $x = 0.25–0.30$ (Fig. 34). The conductivities for $Li_{7+x}Si_xP_{1-x}S_6$ are quite stable within a large part of the Argyrodite stability range ($0.2 > x > 0.4$) at $1.0–1.2 \times 10^{-3}$ S/cm with a slight maximum at $x = 0.35$. Higher Li-ion conductivities were obtained with the composition $Li_{7.33}Si_{0.33}P_{0.66}S_6$ denoted $Li_{2z}SiP_2S_{7+z}$ ($z = 11$) $Li_{22}SiP_2S_{18}$ in the original paper, where σ is 3.2 mS/cm at ambient temperatures.[66] Although still proving good Li-conducting properties, the conductivity of the Argyrodite doped with Fe^{2+}

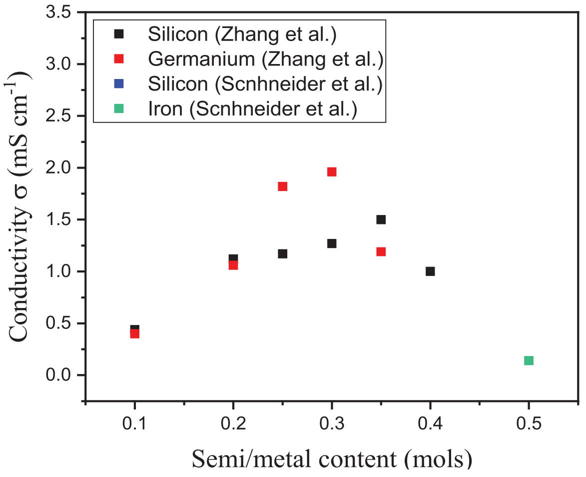

Fig. 34. Li-ion conductivities of $Li_{7+x}Ge_xP_{1-x}S_6$ and $Li_{7+x}Si_xP_{1-x}S_6$ ($0.1 < x < 0.4$), $Li_{7.333}Si_{0.333}P_{0.667}S_6$ and $Li_6Fe_{0.5}P_{0.5}S_6$ for low semi/metal contents.[65,66,68]

($Li_6Fe_{0.5}P_{0.5}S_6$) is approximately an order of magnitude less than those of the Si^{4+} and Ge^{4+} doped electrolytes.[68]

Along with a higher dopant content, for the electrolytes investigated to date, the Li-ion conductivities are one order of magnitude lower than for the best ones of those with low semi/metal contents. Li-ion conductivities are 1.1×10^{-4} S/cm in the highly germanium-doped $Li_7Ge_3PS_{12}$, corresponding to $Li_{3.5}Ge_{1.5}P_{0.5}S_6$[63] and 8.5×10^{-5} S/cm in $Li_{6.96}Sn_{1.55}Si_{1.71}P_{0.8}S_{12}$ ($Li_{3.48}Sn_{0.775}Si_{0.855}P_{0.4}S_6$) Argyrodite stabilized by binary semi/metals silicon and tin.[29]

3.4.3. *Semimetal plus halogen-stabilized Argyrodites*

Co-doping halogen-stabilized Argyrodites with semi/metals according to the compositions $Li_{6+x}M_xP_{1-x}S_5X$ (X = Cl, Br, I) was addressed for the combinations of bromine-based Argyrodites with Si[61] and for iodine-based Argyrodites with M = Ge, Si and Sn co-dopants.[60,62] The original idea behind the co-doping approach was to enhance the structural disorder of I^-/S^{2-} sites. The impact of the co-doping in first instance crucially depends on the type of halogen in the Argyrodite.

A moderate increase in the Li-ion conductivity with Si-content was found for bromine-based Argyrodites $Li_{6+x}Si_xP_{1-x}S_5Br$, leading to the highest ambient temperature Li-ion conductivity within this series of material for $x = 0.35$ corresponding to increase by a multiple of three from 0.7×10^{-3} S/cm to 2.3×10^{-3} S/cm compared to the Si free material Li_6PS_5Br (Fig. 35(a)).[61] In contrast, co-doping of iodine-based semi/metals Si, Sn and Ge results in an increase of conductivity up to several orders of magnitude. Thereby, the conductivities scales with the semi/metal co-dopant content (Fig. 35(b)). Differences in the maximum solubility of semi/metals depending on semi/metal type limit the conductivity performance of the specific materials. While with $x = 0.2$, there is only little solubility for Sn ($Li_{6+x}Sn_xP_{1-x}S_5I$), the solubility limits are enhanced to $x = 0.45$ for Si and to $x = 0.8$ for Ge providing electrolytes with compositions $Li_{6+x}Si_xP_{1-x}S_5I$ and $Li_{6+x}Ge_xP_{1-x}S_5I$, respectively. Accordingly, the maximum conductivities can be observed in the germanium co-doped electrolytes $Li_{6.6}Ge_{0.8}P_{0.4}S_5I$, where the ambient temperature Li-ion conductivity amounts to 5.4×10^{-3} S/cm in a cold pressed state vs. conductivities of 1×10^{-4} S/cm and 2×10^{-3} S/cm for the best tin and silicon co-doped materials, respectively. Although an increase in site disorder along with co-dopant content was detected, the main impact on the enhanced conductivity is attributed to the modifications in Li-substructure.[62]

3.4.4. *Overall comparison of Argyrodite Li-ion conductivities*

A compilation of the results on Li-ion conductivities of the three most discussed types of Argyrodites, halogen stabilized, semi/metal stabilized and the halogen-semi/metal co-doped electrolytes is given in Fig. 36 and Table 5 with distinction made for the processing type (solid state vs. liquid phase). Maximum conductivities for the best electrolytes from each of these groups are in the range of 10^{-2} S/cm for the halogen stabilized and the halogen semi/metal co-doped Argyrodites, while they are at least an order of magnitude less for exclusively semi/metal-doped electrolytes. An evaluation of these results based on the mere numbers on conductivity

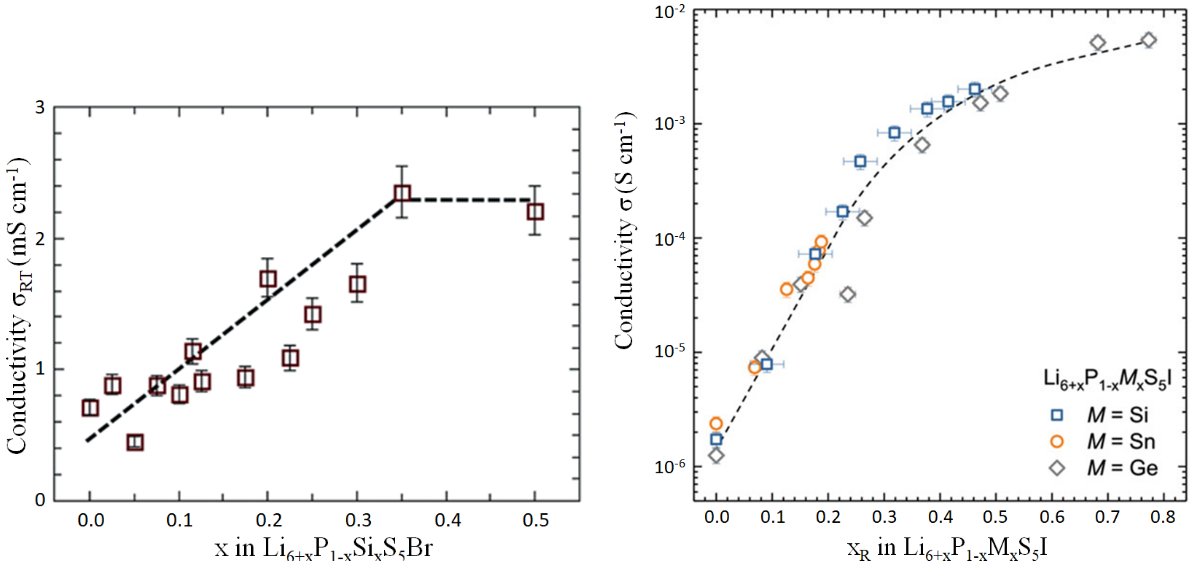

(a)

(b)

Fig. 35. (a) Ambient temperature lithium-ion conductivity of $Li_{6+x}Si_xP_{1-x}S_5Br$ depending on Si content. Reproduced from Ref. 61 with permission from the Royal Society of Chemistry © 2013. (b) Ambient temperature lithium-ion conductivity of $Li_{6+x}M_xP_{1-x}S_5I$ depending on semi/metal content M with M = Ge, Si, Sn. Reprinted with permission from Ref. 62. Copyright © 2019 American Chemical Society.

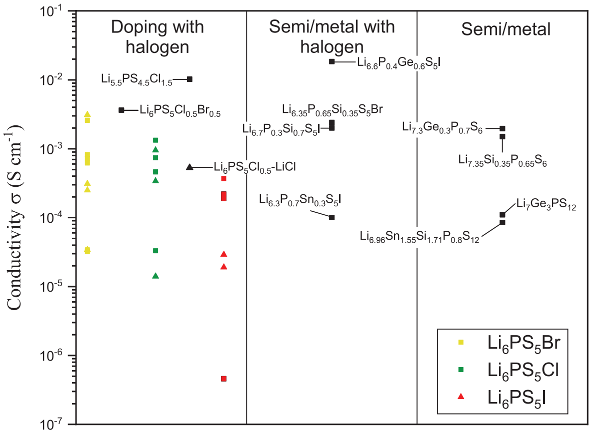

Fig. 36. Li-ion conductivities for halogen stabilized, semi/metal stabilized and the halogen-semi/metal co-doped Argyrodite electrolytes distinguishing solid-state and liquid-phase processed electrolytes. Squares are for solid-state processed, triangles for electrolytes prepared by liquid-phase synthesis. Data and references can be found in Table 5.

nevertheless seems difficult. The data on ambient temperature Li-ion conductivities for the halogen-doped electrolytes encompass the results of many different investigations and scatter over a range of approximately two orders of magnitude. In contrast, there are few works on the semi/metal doped and the co-doped Argyrodites electrolytes, which probably does include materials with lower performance nor the optimally processed variants.

In the $Li_{7-x}PS_{6-x}X_x$ series, solid-state processed as well as liquid-phase prepared materials are among the electrolytes with Li-ion conductivities in both the upper and lower parts of the ranking. When applied to materials suitable for the specific processes, the specific processing parameters seem to be at least equally important as the type of processing route. Overall, there is agreement that the processing is one of the main determinants of Li-ion conductivity. The physical state of the sample used for the measurements is supposedly to be a further major factor of influence on the Li-ion conductivity. Specifically, for $Li_{6.6}Ge_{0.8}P_{0.4}S_5I$, an enhancement of the Li-ion conductivity from 5.4×10^{-3} S/cm for the pressed pellet to 18.4×10^{-3} S/cm for a sample sintered at 975°C for 10 min was reported.[60] However, with an inter-comparisons of different reports, systematic differences between pressed powders vs. sintered ceramic pellets could not be identified, therefore, the data evaluated in Table 5 do not allow for a generalization of this trend. Eliminating the aforementioned issues and focusing on the specific type of sample preparation, measurement and evaluation procedures, a comprehensive Round Robin study has been carried out for $Li_{6.6}P_{0.4}Ge_{0.6}S_5I$, Li_6PS_5Cl, $Li_6PS_5Br_{0.75}I_{0.25}$, $Li_6PS_5Br_{0.25}I_{0.75}$ and Li_6PS_5I.[89] Measurements were carried out by all participating workgroups on materials from a single powder batch, where samples for the measurements were prepared, measured and evaluated according to the specific procedures of the respective group. Typically, the results on Li-ion conductivity were scattering by half an order of magnitude approximately, in some cases even more. No clear influence of pelletizing pressure and contacting material could be detected, while a weak trend with relative densities was found only for part of the materials.[62] Thus, the study documents in depth the difficulty of comparing and evaluating the results on Li-ion conductivity measurements from different research groups.

Table 5. Li-ion conductivity and activation energies of Argyrodite structures at ambient temperature unless otherwise stated. (lq) denotes samples synthesized via a liquid route.

Stoichiometry	σ (S/cm)	E_a (eV)	Ref.
Li_6PS_5Br	2.58×10^{-3}	0.255	84
Li_6PS_5Br	6.2×10^{-4}	0.41	85
Li_6PS_5Br	8.2×10^{-4}	0.228	73
Li_6PS_5Br	7.2×10^{-4}	0.17	80
Li_6PS_5Br	3.2×10^{-5}	0.32	86
Li_6PS_5Br (lq)	3.1×10^{-3}	0.302	87
Li_6PS_5Br (lq)	3.1×10^{-4}	0.419	81
Li_6PS_5Br (lq)	2.5×10^{-4}	0.311	73
Li_6PS_5Br (lq)	3.4×10^{-5}	—	75
$Li_6PS_5Cl_{0.5}Br_{0.5}$	3.63×10^{-3} (32°C)	0.31	88
$Li_{5.5}PS_{4.5}Cl_{1.5}$	1.02×10^{-2}	0.27	59
Li_6PS_5Cl	1.33×10^{-3}	0.33	85
Li_6PS_5Cl	9.5×10^{-4}	—	73
Li_6PS_5Cl	7.4×10^{-4}	0.11	80
Li_6PS_5Cl	4.6×10^{-4}	0.33	85
Li_6PS_5Cl	3.3×10^{-5}	0.38	86
Li_6PS_5Cl (lq)	3.4×10^{-4}	0.399	81
Li_6PS_5Cl (lq)	1.4×10^{-5}	—	73
Li_6PS_5Cl-LiCl (lq)	5.3×10^{-4}	0.29	81
Li_6PS_5I	3.7×10^{-4}	—	73
Li_6PS_5I	2.2×10^{-4}	0.26	86
Li_6PS_5I	1.9×10^{-4}	0.35	85
Li_6PS_5I	4.6×10^{-7}	0.25	80
Li_6PS_5I (lq)	2.9×10^{-5}	0.419	81
Li_6PS_5I (lq)	1.9×10^{-5}	—	73
LT-Li_7PS_6	1.6×10^{-6}	0.16	56
$Li_{6.6}P_{0.4}Ge_{0.6}S_5I$	1.84×10^{-2}	0.16	60
$Li_{6.35}P_{0.65}Si_{0.35}S_5Br$	2.4×10^{-3}	0.14	61
$Li_{6.7}P_{0.3}Si_{0.7}S_5I$	2.0×10^{-3}	—	62
$Li_{6.3}P_{0.7}Sn_{0.3}S_5I$	1.0×10^{-4}	—	62
$Li_{7.3}Ge_{0.3}P_{0.7}S_6$	1.96×10^{-3}	0.197	65
$Li_{7.35}Si_{0.35}P_{0.65}S_6$	1.5×10^{-3}	—	65
$Li_7Ge_3PS_{12}$	1.1×10^{-4}	0.259	63
$Li_{6.96}Sn_{1.55}Si_{1.71}P_{0.8}S_{12}$	8.5×10^{-5}	0.352	29

Summarizing Li-ion conductivity measurements, one may note, within a series of materials prepared, measured and evaluated by the same group of scientists yielded quite subtle differences in conductivity that also correlate to defect chemical and structural characteristics which can be elaborated. In contrast, inter-group comparison of results on Li-ion conductivity has to consider the complete processing, sample preparation and measurement procedures in detail, and to take into account the specific conditions in order to come to a well-balanced evaluation of the performance.

4. Overall Survey and Trends

Regarding properties of the electrolytes, for more than a decade, the focus of research was mainly on Li-ion conductivity. Along with the far-reaching improvements with respect to this property, the integration of solid-state electrolytes have become more realistic and as a consequence new challenges, related to how to integrate the new electrolytes into a battery, such as compatibility of electrolytes with other components and processing emerged. In this context, the stability of the interfaces is the issue of major concern. This summarizing section will be organized covering three subtopics (i) a brief discussion on issues on conductivity with a comparison of high performance electrolytes from each of the four major types, (ii) an analysis of the phosphosulfide electrolytes with respect to their stability in a battery environment focusing on the interface to the Li-metal anode and (iii) perspectives for further development of phosphosulfide electrolytes.

4.1. *Discussion and summary on Li-ion conductivities*

Detailed discussion on Li-ion conductivity in this review is limited to the consideration of macroscopic conductivity at ambient temperature. The scope of the issues related to Li-ion conductivity is of course much wider than this. In particular, for a compound treatment, on an atomistic scale the relations between structure and conductivity of the individual electrolytes must be considered. Regarding application-oriented features, the temperature behavior of the Li-ion conductivity and the dependence on processing on the macroscopic scale have to be reflected. Thus, before summarizing the analysis on the ambient temperature conductivities basic aspects emerging from these issues will be briefly addressed.

4.1.1. *Relations between structure, processing and conductivity*

The structure of phosphosulfide electrolytes consists of an anion framework formed by building blocks of tetrahedra consisting of phosphorus and/or semi/metals, in some cases additional free sulfur anions are present which can be modified by dopants such as halogens or oxygen. The arrangement of the framework structure largely governs the symmetry of the structure and therewith the isotropic vs. anisotropic or 1D, 2D and 3D conductivity behavior. The interspaces of this anion framework are considered to be channels for the lithium transport.

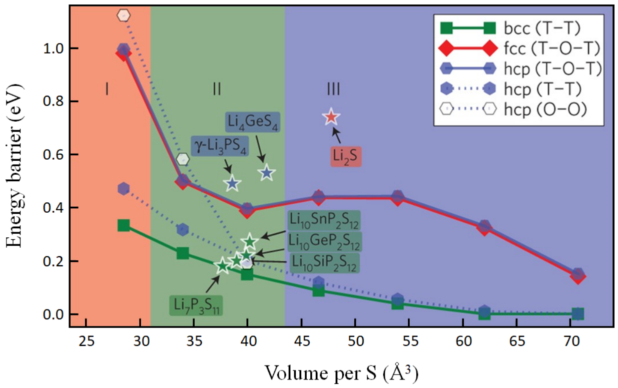

Fig. 37. Energy barrier change according to volume and structure of various sulfur-based solid electrolytes. Reproduced from Ref. 90 © 2015 Springer Nature.

Li-ion mobility is determined by the binding energies to their sites and the activation energy barriers to move to neighboring sites. In order to consider the specific conditions for an individual electrolyte both the binding energies and the energy barriers for potential transition paths have to be evaluated. This typically requires advanced computational methods combined with detailed structural information as obtained by neutron diffraction and NMR. Loosely speaking, the channels for the Li-ion transport have to be sufficiently wide and free of bottlenecks. To some extent, for a given structure, the energy barriers correlate with the lattice volumes normalized to the amount of sulfur (Fig. 37), but there are also limits to this correlation.

Li-ion mobility on a more extended scale is addressed by the analysis of the total energy landscape. Emphasis of the analysis shifts from consideration of the energy of the atoms in the immediate neighborhood of the location close to the hopping event to description by larger scale energy profiles in the lattice which are substantially influenced by disorder and distortion in the lattice.[62]

Recent approaches emphasizes the important roles of phonon dynamics, according to which the soft vibration or polarized anion framework has been identified as basic descriptor for the design of superionic conductors.[17,22,91–97]

4.1.2. *Activation energies and temperature dependence of conductivities*

The changes of the conductivity along with operating temperature within a certain range are related to the ambient temperature conductivity by the Arrhenius relation, where σ_T, σ_o, T, k and E_a denote the Li-ion conductivity, pre-exponential factor temperature (in Kelvins), Boltzmann constant and activation energy, respectively, according to

$$\sigma_T \cdot T = \sigma_o \exp\left(\frac{-E_a}{kT}\right).$$

The activation energy is the energy required for Li-ion migration. A low activation energy indicates the ease of migration and a low sensitivity of the Li-ion conductivity toward temperature changes and vice versa.

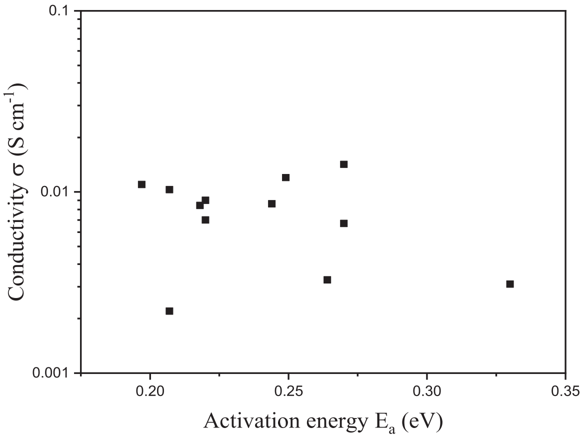

Fig. 38. Li-ion conductivities vs. activation energies for LGPS-type electrolytes. Data and references can be found in Table 2.

Inspection of the tables on conductivities and activation energies for the four types of electrolytes and the individual materials listed therein (Tables 4 and 5 of Part I[98] and Tables 2 and 5 of this paper), does not show correlations between ambient temperature Li-ion conductivity σ_t and activation energy E_a. In these tables, the individual materials are arranged according to decreasing Li-ion conductivity, the activation energies do not show a corresponding increase.

Evaluating the compilation of data on LGPS types electrolytes (Table 2), even when restricting the selection to those electrolytes for which the activation energies were determined based on data in a comparable temperature range, a clear trend is visible neither (Fig. 38).

Results on Li-ion conductivities and activation energies for Li_6PS_5X type Argyrodites with X = Cl, Br, I and combinations of at 1M total halogen content in the Argyrodites even show decreasing trends for both, σ_t and E_a, when considering the sequence of materials according to their increasing lattice parameters from Li_6PS_5Cl via Li_6PS_5Br to Li_6PS_5I.[55]

The wide scope of Li-ion conductivities reported even for the nominally same materials, microstructure and preparation of samples used for the conductivity measurements may be part of the reasons for the lack of correlation, as not only the conditions in the bulk, but also the conductivities and activation energies at the interface sum up to the overall values for σ_t and E_a.

However, analysis during the past decades pointed out that considerable influence on the Li-ion conductivity might be attributed to the pre-exponential factor σ_o in the Arrhenius relation. The pre-exponential factor, $\sigma_o = \sigma_{oo}\exp(S_m/k)$ depends on jump frequency, mobile lithium-ion concentration σ_{oo} and most important on the entropy of activation S_m. The values for the pre-factor σ_o and the activation energy E_a can be correlated via the entropy. Decreasing activation energies E_a correlating to decreasing prefactors σ_o of the Arrhenius relation are discussed under the label "Meyer–Neldel rule".[96,99]

Early work on $Li_{2+2x}Zn_{1-x}GeO_4$ oxygen LiSICon solid solutions found a decrease in pre-exponential factor σ_o by 6 orders of magnitude along with the decrease of the activation energy from 1.0 eV to 0.6 eV.[100] Correlations between the prefactor and activation energy for phosphosulfides that indicate the decrease of both σ_o and E_a along with enhanced disorder of the X^-/S^{2-} site disorder were established for the Argyrodite electrolytes. The correlations apply to a series of Argyrodites doped with different halogens as well as to comparisons between nominally the same materials subject to different processing.[55,71]

Disorder with respect to the X^-/S^{2-} sites in halogen-doped phosphosulfide Argyrodites can be controlled by the thermal process applied for synthesis or thermal post-treatment. Synthesizing Li_6PS_5Br along with low cooling rates Li_6PS_5Br results in mostly ordered materials with only small degree of site disorder, whereas quenching from high temperature induces increasing disorder along with an increase in Li-ion conductivity. Comparing Li_6PS_5Br electrolytes synthesized at different processing conditions by analyzing the factors governing Li-ionic conductivities yields a positive sloped and almost linear correlation between the log-Arrhenius prefactor and the activation energy, implying that a lower activation energy E_a is related to a lower prefactor σ_o (Fig. 39).

Regarding a comparison of phosphosulfide Argyrodites $Li_6PS_5Cl_xBr_{1-x}$ and $Li_6PS_5Br_xI_{1-x}$ results in corresponding decrease of σ_o and E_a for the Cl–Br dopant combinations, whereas for the Br–I combinations, E_a increases while σ_o remains almost constant along with higher iodine content (Fig. 40).

A Meyer–Neldel plot encompassing results on Li-ion conductivity, prefactor in terms of $\log(\sigma_o \cdot T)$ and activation energies E_a for high performance electrolytes encompassing phosphosulfide and garnet electrolytes indicates

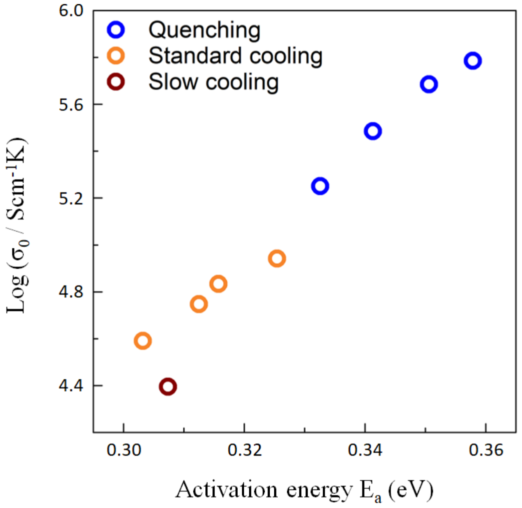

Fig. 39. Activation energy E_a vs. prefactor σ_o for Li_6PS_5Br electrolytes with varying X-/S2-site disorder prepared by different thermal procedures. Reprinted with permission from Ref. 71. Copyright © 2019 American Chemical Society.

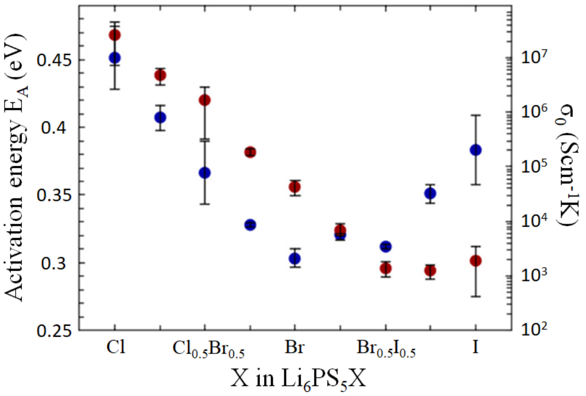

Fig. 40. Activation energy E_a and prefactor σ_o for halogen-doped Argyrodite electrolytes. Reprinted with permission from Ref. 52. Copyright © 2017 American Chemical Society.

correlations between the prefactor and the activation energy with log($\sigma_o \cdot T$) vs. E_a following mostly a linear relationship.[17] In particular for the LGPS type electrolytes, the correlation is quite close when considering the temperature range below 350 K (Fig. 41). Toward this low temperature range, the activation energies are between 0.25 eV and 0.35 eV, while the corresponding prefactors ($\sigma_o \cdot T$) range from 10^5 K S/cm to 10^7 K S/cm. Along with elevated temperatures, both E_a and $\sigma_o \cdot T$ decrease substantially to 0.15–0.2 eV and 10^3–10^4 K S/cm, respectively.[17] Within these data for the Argyrodites, correlations can be observed for some subgroups while for thio-LiSICon, the correlation is still visible but more scatted.

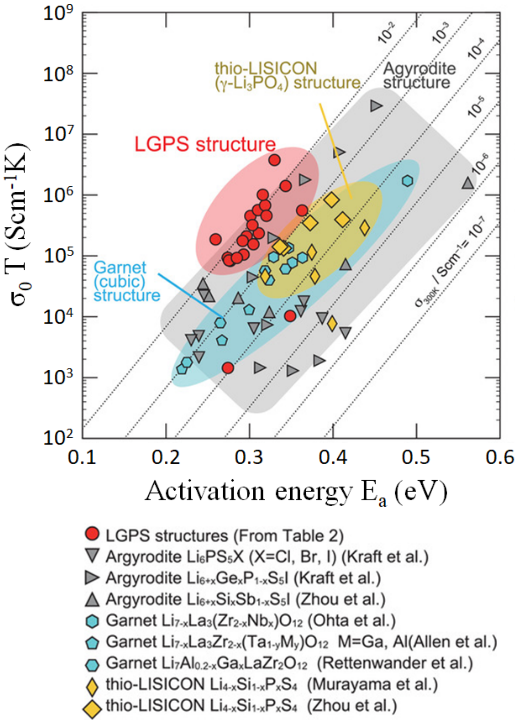

Fig. 41. Meyer–Neldel plot of various types of electrolytes. Table 2 mentioned in the figure can be found in the original text and is not provided in this paper. Reprinted with permission from Kato *et al*. © 2020 Wiley-VCH GmbH.[17]

Summarizing the analysis of determinants for the Li-ion conductivities based on the parameters in the Arrhenius relation, it can be concluded that there is in many cases substantial influence from the entropy contribution to Li-ion conductivity via the prefactor σ_o, which may be even more important than the effects from activation energy on the migration barriers. The material design pointing to high conductivity phosphosulfides, therefore, has to take both, the migration barrier and the entropy, into account. Development of electrolytes toward optimizing the Li-ion conductivity via low activation energies (and low prefactors) vs. high prefactors (and corresponding high activation energies may provide the same ambient temperature conductivity, but may result in different conditions for the temperature stability, as the influence of the prefactor on the conductivity is linear, whereas the activation energy is exponential. If this difference is technically relevant, it will depend on the specific parameters, the temperature range under consideration. It also has to be taken into account that the temperature range, for which the specific Arrhenius parametrization by σ_0 and E_a holds, is in many cases limited.

With respect to the physical meaning, a lower activation energy provides easier conditions for hopping and this mobility of the Li-ions. At a given conductivity, the activation energies are lowest for LGPS followed by Argyrodites and then thio-LiSICons (Fig. 41). From a technical point of view, a lower activation energy indicates less sensitivity of the Li-ion conductivity to temperature variations and thus more stable temperature behavior of the electrolyte.

Recalling the results on synthesis methods for phosphosulfide electrolytes, different types of processes applied with identical chemical educts yield different morphologies owing to the tendency to form glassy phase components and, most importantly, to different conditions at the grain boundaries of ceramics. Thus, comparisons based merely on compositions of electrolytes do not give a realistic picture of the capability of the materials. Fair comparisons of the performance cannot be limited to chemicals but also have to take into account the materials aspect, i.e. the microstructures. While for some of the materials a microstructure almost ideal for high Li-ion conductivity may be obtained by a one shot experiment, for others it can be very tedious to accomplish a favorable microstructure. For the phosphosulfides, there is a lot of optimization with respect to these issues still to be done.

4.1.3. *Inter-type comparison of conductivities for lithium phosphosulfide electrolytes*

The status of Li-ion conductivity at ambient temperature is summarized in an inter-type comparison for, the Li–P–S type, the LiSICon type, the LGPS type and the Argyrodite type phosphosulfide electrolytes. Within each of the phosphosulfide types, the best-performing electrolyte of their most important subgroups is considered. High Li-ion conductivity electrolytes can be identified in each of the four types of phosphosulfides with a large scope of materials with Li-ion conductivities exceeding 10^{-4} S/cm. In the Li–P–S system, $Li_7P_3S_{11}$ and $Li_{9.6}P_3S_{12}$ reach Li-ion conductivities even higher than 10^{-3} S/cm, while the conductivity for the best performing β-Li_3PS_4 is 3.3×10^{-4} S/cm.[101] The highest performance for LiSICon-type electrolytes are shown by $Li_{3.25}Ge_{0.25}P_{0.75}S_4$ and $Li_{3.4}Si_{0.4}P_{0.6}S_4$ with Li-ion conductivities of 2.2×10^{-3} S/cm and 6.4×10^{-4} S/cm, respectively.[30,102] Li-ion conductivities higher than 10^{-2} S/cm are realized by electrolytes among the Argyrodite types and in particular among the LGPS-type electrolytes.

The highly Cl-doped $Li_{5.5}PS_{4.5}Cl_{1.5}$ Argyrodite has a Li-ion conductivity of 1.02×10^{-2} S/cm,[59] while for the more moderately (1 M) halogen-doped Argyrodites, the Li-ion conductivities with 3.63×10^{-3} S/cm for $Li_6PS_4Cl_{0.5}Br_{0.5}$,[88] 2.58×10^{-3} S/cm for Li_6PS_4Br and 1.33×10^{-3} S/cm for Li_6PS_4Cl are in in the range between 10^{-3} and 10^{-2} S/cm.[84,85] So far, the highest Li-ion conductivities are provided by the electrolytes of the LGPS type. Ten years after its discovery, the Ge-based prototype $Li_{10}GeP_2S_{12}$ with its Li-ion conductivity of 1.2×10^{-3} S/cm is still among the fastest Li-ion conductors. However, the conductivities of the more resource efficient tin- and silicon-based $Li_{10.35}Si_{1.35}P_{1.65}S_{12}$ ($\sigma = 6.7 \times 10^{-3}$ S/cm)[21] and $Li_{9.81}Sn_{0.81}P_{2.19}S_{12}$ ($\sigma = 5.0 \times 10^{-3}$ S/cm)[21] variants are only half a magnitude less. The highest Li-ion conductivity among the phosphosulfide electrolytes is provided by a Cl-doped LGPS-type electrolyte $Li_{9.54}Si_{1.74}P_{1.44}S_{11.7}Cl_{0.3}$ that amounts to 2.5×10^{-2} S/cm.[9] Thus, with respect to ambient temperature Li-ion conductivity, a wide scope of phosphosulfide electrolytes is available that meets the requirements for operating an all solid-state Li-ion battery.

High Li-ion conductivity electrolytes can be identified in each of the four types of phosphosulfides. In the Li–P–S system, among the Argyrodite types and in particular among the LGPS-type electrolytes there are several with an ambient temperature Li-ion conductivities exceeding 10^{-2} S/cm (Fig. 42).

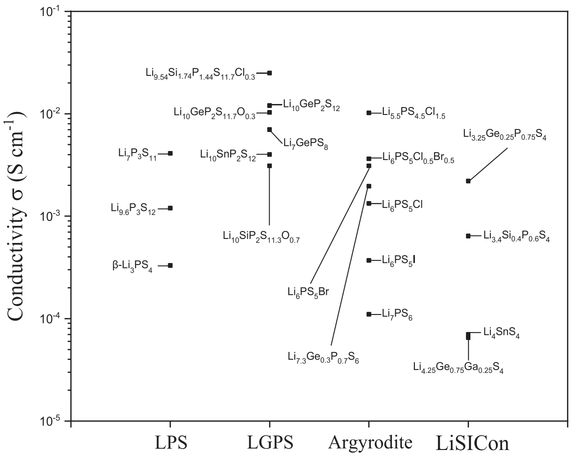

Fig. 42. Summary of Li-ion conductivities for high performance electrolytes among the Li–P–S, LGPS, Argyrodite and thio-LiSICon type phosphosulfides.

4.2. *Electrochemical stability of the lithium phosphosulfide electrolytes vs. metallic lithium*

4.2.1. *Theoretical approaches to interface stability*

From a theoretical point of view, the electrochemical stability of an electrolyte in contact with metallic lithium can be analyzed by three different concepts to determine the electrochemical stability window: the phase stability approach (sometimes termed thermodynamic approach[103]); the stoichiometry stability approach (sometimes termed topotactic approach[103]); and the band gap approach. The concepts differ with respect to the scenarios underlying the instability.

In the band gap approach, the reduction or oxidation of the electrolyte by electron transfer from or to the electrode is considered. The electrochemical stability window is calculated via the difference between the highest occupied molecular orbital (HOMO), i.e. the valence band maximum vs. the lowest unoccupied molecular orbital (LUMO), i.e. the conduction band minimum.[104] This method yields an estimate for the potential range of stability but not for the absolute position with respect to the reference electrode. Since the band gap method is exclusively charge transfer based, it provides an upper limit for the range within which the electrolyte is electrochemically stable.[104–106] In contrast, the phase stability method and the stoichiometry stability method define the electrochemical stability based on a coupled transfer of an electron and a Li-ion, which is necessary to preserve charge neutrality and to keep the reaction running. The methods differ in the decomposition scenarios upon de-/lithiation. The stoichiometry method assumes a decomposition of the electrolyte by gradual Li-transfer with solid solution behavior of the electrolyte and defines the electrochemical stability window by the Li-insertion and -extraction potentials. Contrarily, the phase stability concept is based on the thermodynamic decomposition of the electrolyte into different product phases and determines the electrochemical stability by evaluating the grand canonical phase diagram. Both the stoichiometric and the phase stability concepts yield the electrochemical stability window in terms of absolute potentials.[104]

Calculations of the grand canonical potential yield, for all types of phosphosulfide electrolytes, reduction potentials of

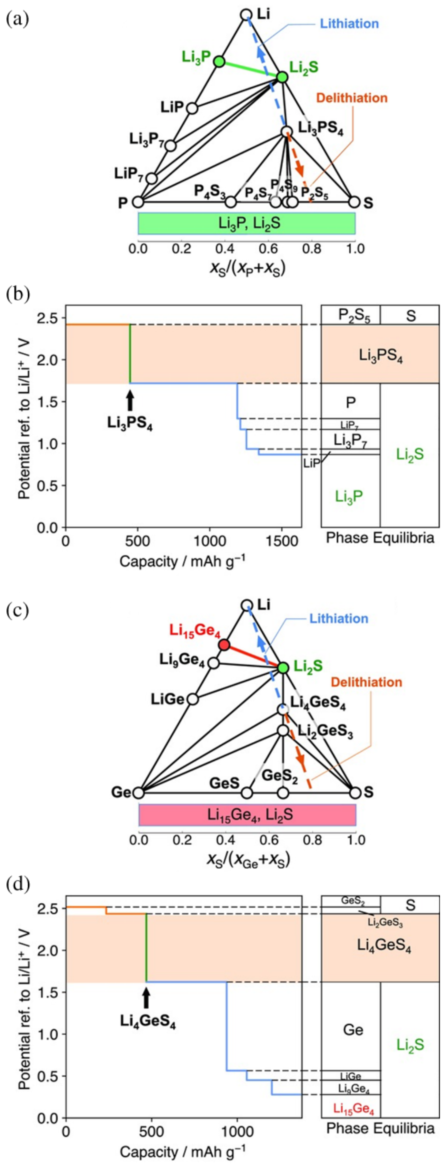

Fig. 43. Phase diagrams of (a) Li–P–S and (c) Li–Ge–S system, and the equilibrium voltage profiles and phase equilibria for lithiation and delithiation reactions of (b) Li_3PS_4 and (d) Li_4GeS_4. Li-stable phases that are electronic insulating (Li_3P and Li_2S) and that are electronic conductive ($Li_{15}Ge_4$) are colored green and red, respectively. The bottom bar in (a) and (c) represents the phase equilibria with Li metal as a function of atomic fraction xS and xM, where passivating and nonpassivating ranges are colored green and red, respectively. The lithiation and delithiation paths in (a) and (c) are marked as blue and orange dashed lines, respectively. These lines represent constant ratio of S and M atomic fraction xS to xM (M = P, Ge) but with varying Li content in the composition. Reprinted with permission from Zhu *et al*. © 2017 Wiley-VCH GmbH.[107]

around 1.7 V vs. Li/Li^+ (Figs. 43(b) and 43(d)), thus indicating that these electrolytes are not intrinsically stable in contact with metallic lithium.

Li_3PS_4 first decomposes at 1.72 V vs. Li/Li^+ to Li_2S and P, then passes several intermediate products along with reduction of the potentials, before ending up with the stable decomposition products Li_2S and Li_3P (Figs. 42(a) and 42(b)). The enthalpy of the lithiation reaction (1) is $\Delta H = -11.39$ eV (−1099 kJ/mol)

$$8\,\mathrm{Li} + \mathrm{Li_3PS_4} \rightarrow \mathrm{Li_3P} + 4\,\mathrm{Li_2S}. \qquad (1)^{107}$$

The same stable interphase constituents from Li_3P and Li_2S will also be formed for all ternary Li–P–S electrolytes after complete lithiation, as in this system Li_3P and Li_2S are the only stable phases against Li. However, the potentials at which the decomposition initiates, and consequently the electrochemical stability windows, are specific for each individual material. The reduction reaction $Li_7P_3S_{11}$ starts as early as 2.28 V vs. Li/Li^+.[108]

The prototype electrolyte of the thio-LiSICon electrolytes Li_4GeS_4 undergoes the first step of the lithiation reaction at 1.62 V, leading to the reduction toward Ge and Li_2S. Along with lowering the potential intermediate, Li–Ge alloys are formed. The decomposition ends up with $Li_{15}Ge_4$ and Li_2S as final products (Figs. 43(c) and 43(d)). The enthalpy for the complete lithiation reaction (2) is −8.04 eV (−775 kJ/mol).

$$7.75\,\mathrm{Li} + \mathrm{Li_4GeS_4} \rightarrow 0.25\mathrm{Li_{15}Ge_4} + 4\,\mathrm{Li_2S}. \qquad (2)^{107}$$

The lower bound of the electrochemical stability window for $Li_{10}GeP_2S_{12}$ is 1.71 V vs. Li/Li^+ (Fig. 44). Final decomposition products at Li-potential are $Li_{15}Ge_4$, Li_3P and Li_2S.[40,109] The decomposition energy to Li_4GeS_4 and Li_3PS_4 is 25 meV per atom. Conditions at the interface are quite similar for $Li_{10}SiP_2S_{12}$ and $Li_{10}SnP_2S_{12}$, which decompose at lithium potential to $Li_{21}Si_5$, Li_3P, Li_2S and $Li_{17}Sn_4$, Li_3P, Li_2S, respectively.

Slightly higher lower bounds of the stability window than those for the LGPS-type electrolytes were calculated for Argyrodites according to the phase stability approach. The instability for Li_6PS_5Cl starts at potentials lower than 1.7 V vs. Li/Li^+, whereby the reduction is initiated by the phosphorus P^{5+}/P^{4+} transition (Fig. 45). The results for the stability window following on the phase stability approach are based

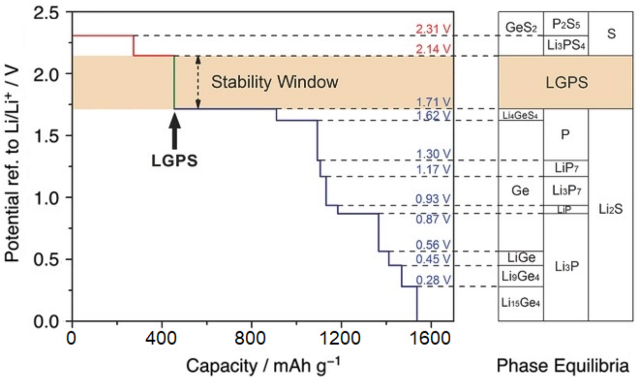

Fig. 44. Calculated phase equilibria and voltage profile for the $Li_{10}GeP_2S_{12}$ electrolyte. Reprinted with permission from Han *et al*. © 2016 Wiley-VCH GmbH.[109]

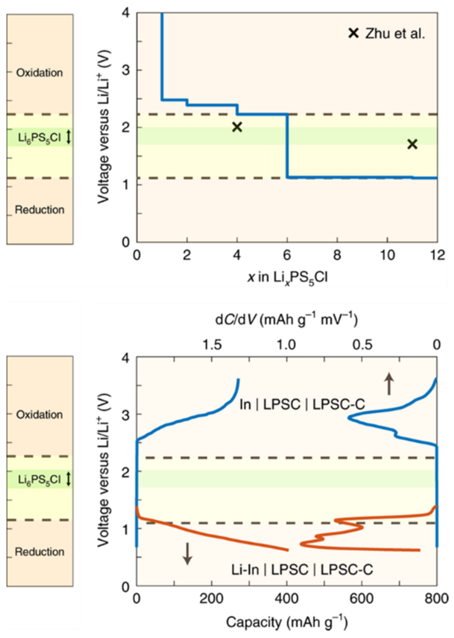

Fig. 45. Calculated phase equilibria and voltage profile for the electrolyte Li_6PS_5Cl. Reproduced from Schwietert *et al*. © 2020 Springer Nature.[110]

on an initial decomposition reaction (3).[111]

$$2\ Li_6PS_5Cl + 2\ Li \rightarrow 2\ LiCl + Li_4P_2S_6 + 4\ Li_2S. \qquad (3)$$

Final stable products for the Cl-, Br- and I-substituted Argyrodites are Li_3P, Li_2S and the lithium halide of the respective species, LiCl, LiBr or LiI.[111–113] Specifically for Li_6PS_5Cl, the relevance of the phase stability approach for the actual processes at the interface is under discussion.[110]

In case of the Argyrodite Li_6PS_5Cl, the results for the stability window following on the phase stability approach are based on an initial decomposition reaction $2\ Li_6PS_5Cl + 2\ Li \rightarrow 2\ LiCl + Li_4P_2S_6 + 4\ Li_2S$ with final products Li_2S, Li_3P and LiCl.[111] Calculations of the stability window following the stoichiometric stability approach show a substantially extended stability window for this scenario to 1.16 V compared to the 0.3 V window calculated from phase stability approach.[110] On reduction by cathodic potentials, the initial decomposition of the lithiated Li_6PS_5Cl is described by the reaction $Li_{11}PS_5Cl \rightarrow P + 5\ Li_2S + LiCl$. The calculated lower bound for the stability window of 1.08 V is substantially lower than the limit of 1.7 V vs. Li/Li⁺ resulting from the phase stability approach.[110,112]

Calculated stability windows for selected electrolytes from each type of the phosphosulfide electrolytes: Li_3PS_4 and $Li_7P_3S_{11}$ for the Li–P–S type, Li_4GeS_4 and Li_4SnS_4 for the LiSICon type, $Li_{10}GeP_2S_{12}$ and $Li_{9.75}Ge_{0.75}P_{2.25}S_{12}$ and Li_6PS_5Cl and $Li_7P_2S_8I$ for the Argyrodite type are summarized in Fig. 46.

In general, the phase stability and the stoichiometric stability follow the same trends.[104] However, since the phase stability approach doesn't consider any kinetic stabilization of the phase such as nucleation generating an overpotential, it provides the worst case scenario, i.e. a narrow stability window. In contrast, the predictions via the stoichiometry approach, which doesn't involve any kinetic limitations of the single Li-ion transfer, result in more favorable results, e.g. wider stability windows.[103]

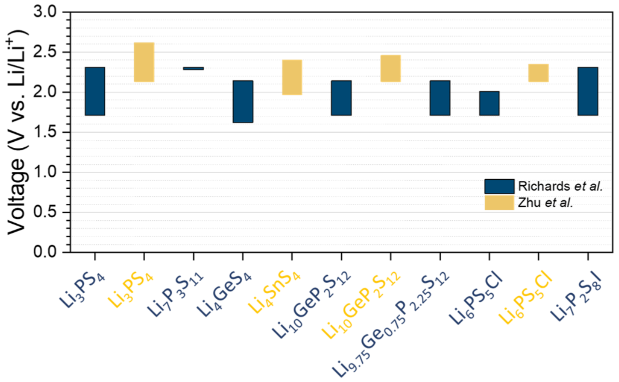

Fig. 46. Calculated stability windows for Li–P–S type, LiSICon-type, LGPS-type and Argyrodite-type phosphosulfide electrolytes according to calculations from Zhu *et al*.[114] (yellow) and Richards *et al*.[111] (blue).

As the band gap approach considers only the transfer of electrons, but not the Li-exchange, this approach describes the upper limit for the electrochemical stability window. Nevertheless, this approach is closely related to the stoichiometric stability method and in most cases provides similar results.[106]

All these concepts for the stability windows indicate in principle intrinsic properties of the bulk and entirely ignore kinetic effects. Based on the argument that the reaction energies are quite large, the effect of interfacial energies is mostly neglected. The electrochemical decomposition of the electrolyte typically occurs at the interface where an electron source is available.

Explicit interface calculations that directly consider the energetics of species with structural relaxations at the interface in DFT supercells have been examined for Li_3PS_4/Li[115] and $Li_{10}GeP_2S_{12}$/Li[116] interfaces. Heat of formation is modified for Li_3PS_4 slab surfaces vs. vacuum by surface energies amounting to 0.012–0.020 eV/Å² thus from 8.2 eV for the bulk up to 7.7 eV depending on the number of unit cell layers in the slab.[115] The presence of lithium substantially alters the arrangement of the atoms in the surface near region compared to the structures calculated for vacuum. These results indicate that metallic lithium will react with the Li_3PS_4 electrolyte. Stabilization of the Li_3PS_4 surface structures and the interphase is obtained, when a two layer thin film of Li_2S is added.[115] $Li_{10}GeP_2S_{12}$ interfaces were investigated for [001] surfaces with both, PS_4- and GeS_4-termination. Calculation of the partial densities of states (PDOS) at the interface indicates that the conduction band minima shifts to a lower energy and the band gaps are slightly reduced compared to the bulk. In contact with lithium, the band gaps at the interfaces layers vanish and interfaces have metallic character.[116]

In order to capture kinetic effects, explicit dynamic models of the processes at the interfaces with *ab initio* molecular dynamics were carried out for the interfaces $Li_7P_3S_{11}$/Li, $Li_{10}GeP_2S_{12}$/Li, β-Li_3PS_4/Li focusing on their low index facets (001) and (100) matched to (100)-Li surface.[117] In general, the dynamics of interface systems can be described only at elevated temperatures and very small time scales (<1 ns) by molecular dynamics, nevertheless the pronounced driving force to form the reaction products Li_xS, Li_yP and Li_zGe in the phosphosulfide electrolytes makes them appear in *ab initio* molecular dynamics simulations of crystalline Li–P–S compounds or LGPS in contact with Li metal. The calculations indicate a sequential decomposition of the PS_4 groups and, in case of LGPS, the GeS_4 groups along with breaking the P–S or Ge–S bonds, respectively. The formation of Li_xS, Li_yP and Li_zGe species is indicated by the lithium coordination numbers of sulfur, phosphorus and germanium at the end of the simulation even within 20 ps at 300 K.[117]

Reactivity at the interface between Li-metal and Li_6PS_5Cl investigated by *ab initio* molecular dynamics revealed similar mechanisms, progressive breaking of P–S bonds, for the reactions of these interfaces.[118] The main decomposition products are Li_2S, Li_3P, LiCl and LiP.[119] Comparing alternative combinations of the surface orientations at the interface, Li(110)/Li_6PS_5Cl(110) and Li(111)/Li_6PS_5Cl(111) showed faster interface degradation vs. Li(100)/Li_6PS_5Cl(100) and Li(221)/Li_6PS_5Cl(100), as concluded from their higher coordination numbers for P and S in Li environment.[118]

Recent developments in the area of machine learning interatomic potentials make larger length and time scales for molecular dynamics simulations feasible. Furthermore, they allow the simulation of amorphous glass-ceramic systems with near DFT accuracy but reasonable computational effort. First machine learning potentials for $Li_{10}GeP_2S_{12}$[120,121] and the Li–P–S type electrolytes[122] have extended the scope of molecular dynamics simulations to several nanoseconds and thousands of atoms spanning different phases, stoichiometries and morphologies. Machine learning interatomic potentials are also advancing molecular dynamics simulations of solid electrolyte/Li interfaces.[123]

While there is general agreement that interphases are formed on contact of phosphosulfide electrolytes with metallic lithium, two aspects, the reversibility and the conductivity properties of the interphases, come in the focus of research interest. The interphases Li_3P, Li_2S and the Li-halides LiCl, LiBr and LiI are stable in contact with metallic lithium.[108] Other intermediate reaction products in the interphase, such as LiP_7, Li_3P_7, LiP, metallic Ge, Ge–Li alloys LiGe and Li_9Ge_4 are not stable at low potentials.

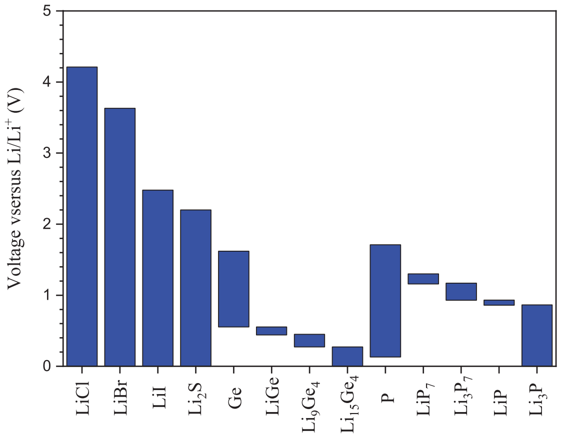

Fig. 47. Stability windows for interphase products and their intermediates at interfaces formed between phosphosulfide electrolytes and metallic lithium.[107–109]

Moreover, for all interphase components, the upper bound of the stability window is limited (Fig. 47). Therefore, electrochemical reactions involving these materials may occur during cycling that contributes to the capacities of the cells at specific potentials. Investigations on Li_6PS_5Cl indicate that the reversibility of the reactions and their manifestation in additional capacity depend on the cycling range.[112]

Most important with respect to the evolution and the properties of the interface, three different types of interfaces, depending on the electrochemical stability and, in case of nonstable interfaces, the conductivity properties of interphase material may form. Thus, three types of interphases (i) thermodynamically stable interfaces without reactions, (ii) nonstable interfaces forming nonpassivating interphases with both electronic and Li-ion conductivity (mixed conducting interphase or MCI) and (iii) nonstable interfaces resulting in a passivating interphase (solid electrolyte interphase or SEI) with negligible electronic conductivity have to be distinguished.[124]

While a thermodynamically stable interface (type i) might be the ideal case, avoiding side reactions, additional resistances and promoting charge transfer across the interface, this type does not apply to phosphosulfide materials vs. metallic lithium. In all these electrolytes, lack of thermodynamic stability implies that an interphase is formed. The extent to what it grows and the consequent interphase resistance depend on the transport properties of the materials formed in the interphase.

In the case of an electronically insulating layer (type iii), the supply of electrons required to keep the electrolyte decomposition reaction ongoing is not sustained. Thus, the reaction stops after an interphase thickness that is high enough to prevent the transport of electrons is reached. As long as sufficient Li-ion conductivity is still provided by the interphase, stable cell performance can be expected, however,

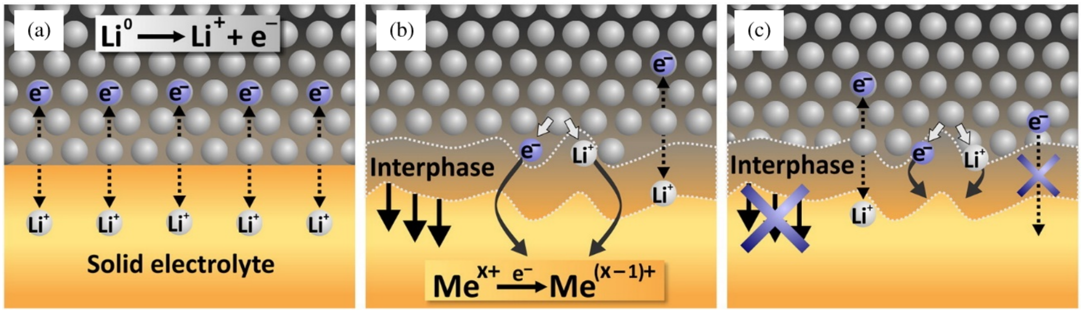

Fig. 48. Types of interfaces between lithium metal and a solid lithium ion conductor. (a) Nonreactive and thermodynamically stable interface; (b) reactive and mixed conducting interphase (MCI); (c) reactive and metastable solid-electrolyte interphase (SEI). Reprinted with permission from Wenzel *et al.* © 2015 Elsevier B.V.[125]

along with reduced performance due to additional resistance caused by the interphase. In contrast, along with a formation of a Li-ion and electronically conducting interphase (MCI) (type ii), a continued decomposition reaction of the electrolyte will be supported, which leads to ongoing growth of the interphase layer, consequent increase of the resistance and nonstable operation of the cell (Fig. 48).[125]

4.2.2. *Experimental work on interface stability — Electrochemical methods*

Scrutinizing differing results on the electrochemical stability from early experimental works vs. the results from theory resulted in pointing out different concepts underlying the evaluation of the electrochemical stability of electrolytes vs. metallic lithium. Limited electrochemical stability as calculated from theoretical approaches stood in contrast with the wide stability range that appeared to be indicated from cyclic voltammetry (CV) and cycling experiments. This led to detailed investigations of overpotentials, and, most importantly, of the role of interphase formation. Insight is gained from the research clarified and promoted concepts for intrinsic vs. kinetic stability of the interface.

The most important techniques used to investigate the stability of electrolytes vs. metallic lithium by electrochemical methods are CV measurements and long-term cycling experiment of Li/electrolyte/Li samples. CVs are in principle designed to determine the thermodynamic and topotactic stabilities at the lower bound of the stability window providing experimental evidence for the results from theory while long-term cycling experiments supply information on the kinetic stability of the interface growth upon contact of the electrolytes to metallic lithium under specific current conditions.

Cycling experiments are not very sensitive and moreover decomposition products may emerge right on mere contact between the metallic lithium and the electrolyte. Thus, evidence on the presence or absence of small interface reactions in the first cycles is in general not possible. Along with long-term cycling, however, changes in the stripping and plating potentials may indicate electrochemical instability. For example, other processes like dendrite growth or changes in contact between the lithium electrodes and the electrolytes during long run cycling are also possible sources of variations in potentials. Nevertheless, cycling experiments are the standard method for evaluating the kinetic stability of the interfaces between electrolytes and metallic lithium. Experimental work demonstrates that plating-stripping cycles of symmetric Li/electrolyte/Li samples for Li_3PS_4 and Argyrodites as Li_6PS_5Cl or $Li_{5.5}PS_{4.5}Br_{1.5}$ (Fig. 49(a)) can be conducted along with stable potentials for many cycles,[126] whereas the same configuration with LGPS electrolyte without further precautions is subject to substantial increase in overpotentials along with high cycle numbers (Fig. 49(b)).[127]

Cycling experiments of Li/electrolyte/Li samples give an assessment on the interface stability of the electrolytes vs. metallic lithium from a technical point of view. Stable stripping and plating potentials when cycling at a given current density indicate the kinetic electrochemical stability at the specific conditions. While this approach proves stability in a technical sense at the specific potentials resulting from the experiments, thus providing a lower limit for the kinetic potential stability range, it does not deliver explicit values for the stability limiting potential.

Experimental identification of the lower bound of the electrochemical stability window by CVs is very challenging. In case of passivating products from the decomposition reaction, a precondition for detecting electrochemical decomposition at the interface between electrolytes and metallic lithium via CV is that the extent of the reaction is high enough to result in measurable current (or current increase). In case a mixed Li-ion electronic conducting interphase forms, its growth kinetics have to be fast enough to provide sufficiently pronounced impact on the CV profile. Spotting the currents resulting from the formation of interphase layers with thickness of several nanometers at standard sweep rates requires highly sensitive current measurements.

Moreover, the careful choice of appropriate reference electrode setup is required. Consequently, reports

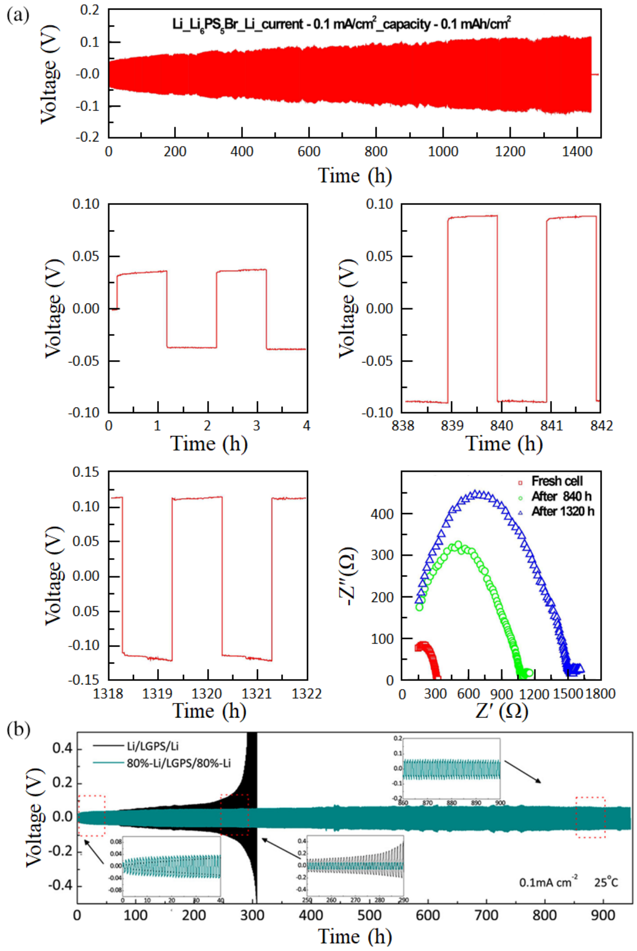

Fig. 49. (a) Li/ Li5.5PS4.5Br1.5/Li cycling showing stable potentials over many cycles. Reprinted with permission from Yu *et al.* © 2020 Elsevier.[126] (b) Li/LGPS/Li cycling showing substantial increase in overpotentials. Reprinted with permission from Ref. 127. Copyright © 2018 American Chemical Society.

on electrochemical stability for the same type of materials derived from analysis of CVs vary over a wide range of potentials, frequently overestimating the stability window. An approach to improve the conditions to capture the onset potentials for the decomposition redox reactions correctly is to admix conductive carbon particles to the solid electrolyte working electrode in CV measurements, which results in enhanced currents. Another method to identify the onset potentials for the decomposition is to perform stepwise cyclic voltammetry experiments.[128]

When analyzing CVs, the cathodic scan may not exclusively detect reduction reactions of the electrolyte, but, depending on the previous cycling range and profile, also decomposition products emerging during eventual precedent anodic scans. Re-reduction of the corresponding oxidation products have to be taken into account when evaluating the CVs. Meanwhile, there is an evidence for reduction reactions of decomposition products after preceding anodic scans caused by oxidation of $S_x \rightarrow S_x^{2-}$, that also point out the relation of the reduction reactions on the upper potential limits of the anodic scans for β-Li$_3$PS$_4$, LGPS and Argyrodites.[109,110,113,128,129] In contrast, the reduction currents for initial anodic sweeps starting from OCV are very small, so a precise identification of the stability of the neat electrolyte remains challenging.[109,129]

4.2.3. *Experimental work on interface stability — Spectroscopic methods*

Experimental results based on spectroscopy techniques provide results that are in general in agreement with the theoretical predictions. Owing to the specific characteristics and limitations of the individual methods, combined application of several spectroscopy methods is useful. X-ray photoelectron spectroscopy (XPS) and Raman spectroscopy allow for the identification of decomposition products, but require an optical access to the surfaces, thus limiting the analysis to model-type setups, whereas impedance spectroscopy is applicable to more realistic cell configurations, but does not deliver information on the chemistry.

In β-Li$_3$PS$_4$, the conversion of the PS_4^{3-} to $P_2S_6^{4-}$ and Li_2S at a β-Li$_3$PS$_4$/gold interface upon Li deposition, has been detected by Raman spectroscopy.[130] The presence of the $P_2S_6^{4-}$ indicates $Li_4P_2S_6$ formation which occurs along with the onset of the electrolyte reduction according to theory. The reactions were found to be partially reversible. Li_3P and Li_2S were identified from XPS P2p and S2p peaks on $Li_7P_3S_{11}$ surfaces while sputtering thin Li-layers thereupon.[125] On analyzing the surface evolution for $Li_{10}GeP_2S_{12}$ with the same setup, in addition to the presence of Li_3P and Li_2S formation of $Ge^{(4-x)+}$ and Ge^0 was indicated from the analysis of Ge3d peaks while sputtering 32 nm Li-films at film −80°C.[131] The presence of the intermediate decomposition product Ge was ascribed to the slow kinetics due to the low temperatures during the experiment required to prevent from sulfur evaporation along with the high vacuum conditions in XPS. Li_3P and Li_2S were also detected in an analogous experiment for Argyrodite Li_6PS_5Cl electrolyte, while the identification of the third decomposition product predicted from theory, LiCl, was not unambiguously possible due to only small differences in the binding energies for Cl^- in LiCl vs. Li_6PS_5Cl and the consequent overlapping of the Cl 2p signals (Fig. 50).[132] Concomitant results from impedance spectroscopy revealed the increase of the resistance due to the interphase layer growth.

Evaluating these data based on a model for diffusion-driven growth of a mixed conducting phase (Wagner tarnishing model), yields a linear dependence of layer thickness and interface resistance vs. the square root of time.[132] Approximating the Li-ion conductivity of the interphases with that of Li_2S and extrapolating the data in accordance with the model indicate that for $Li_7P_3S_{11}$ and the Li_6PS_5Cl

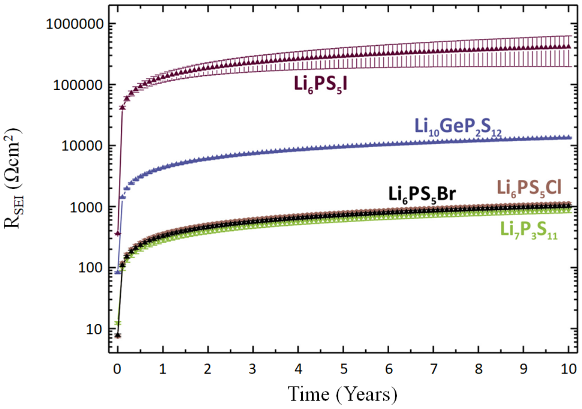

Fig. 50. Simulated SEI resistance for Li_6PS_5I, $Li_{10}GeP_2S_{12}$, Li_6PS_5Cl, Li_6PS_5Br and $Li_7P_3S_{11}$ over a period of 10 years. Reprinted with permission from Wenzel *et al*. © 2018 Elsevier.[132]

and Li_6PS_5Br Argyrodites are relatively stable and long-term resistance and performance might be expected, whereas for $Li_{10}GeP_2S_{12}$ a much more pronounced increase of the interface resistance with time may occur (Fig. 47).[132]

One of the most advanced spectroscopic techniques to analyze the interphase formation and Li-plating is in-operando XPS mimicking the operation of a cell by means of a virtual electrode. A flux of electrons to the electrolyte surface is provided by an electron gun and builds up a charge on the surface, thus generating potential gradient crossways the cell. Along with a counter electrode capable to supply Li-ions (e.g. lithiated LTO), the Li-ions move to the virtual electrode and react combined with the electrons there. While in the first stages of the experiment, SEI species are formed as the reduction products, after building up the SEI applying a sufficient amount of charge the process eventually turns to plating of metallic Li.[133] During buildup of the interphase layer components, Li_2S, Li_3P, Li_xP, and in case of LGPS, Li-Ge alloy were identified, while in case of Li_6PS_5Cl, no significant change of the Cl environment was detected. The difference between the electronically insulating interphase layers formed on Li_6PS_5Cl vs. the conductive one on $Li_{10}GeP_2S_{12}$ manifests in the overall evolution of the experiment. In case of Li_6PS_5Cl, after built-up of a sufficiently thick electronically insulating SEI, the transport of electrons through the interphase to the electrolyte surface is no longer sustained, thus, there is no further growth of the interphase layer. The lithium ions move to the (free outer) surface of the interphase layer and are reduced there to metallic lithium — lithium plating starts after ca. 20 min. In contrast, the electronically conductive interphase on $Li_{10}GeP_2S_{12}$ allows for electron transfer to the (inner) surface of the interphase at the electrolyte interface, thus propagating the reduction reaction further toward the bulk of the electrolyte. Consequently, no lithium plating is detected on the (outer free) surface.

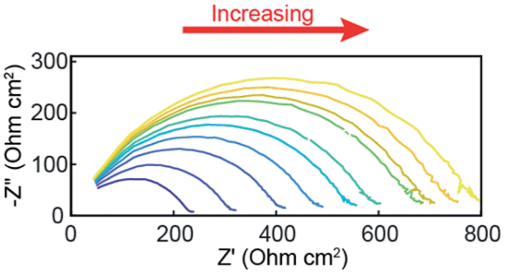

Fig. 51. EIS measurement of impedance of uncoated LGPS. Reproduced from Ref. 134 with permission from the Royal Society of Chemistry © 2013.

While the *in-operando*, XPS experiments provide a high-end tool to analyze the interphase evolution and Li-plating, the impedance spectroscopy is one of the "working horses" for the analysis of interface stability. Applied to symmetric $Li/Li_{10}GeP_2S_{12}/Li$ cells subject to cycling, the growth of an interphase layer manifests with an increase in the impedance (Fig. 51) along with increasing cycle number. Within a time span between 20 h and 110 h, the real part of the area-specific impedance increases from 200 Ω/cm^2 to 800 Ω/cm^2 owing to the growth of the interphase layer.[134]

Time-dependent increases in resistivity due to interphase formation were also reported for interfaces of silicon- and tin-based LGPS-type electrolytes with metallic lithium. While Li-ion conductivities of the MCI layers were determined and estimated in the range of 10^{-7} to 10^{-6} S/cm, the impedance analysis also indicated high electronic conductivity of 10^{-7} to 10^{-5} S/cm for $Li_{10}GeP_2S_{12}$, $Li_{10}SiP_2S_{12}$ and $Li_{10}Si_{0.3}Sn_{0.7}P_2S_{12}$.[47]

Reactions at the electrode/electrolyte interface are quite sensitive to the individual compositions of the materials.[135] The evolution of interface resistances varies substantially with stoichiometry according to analysis of impedance measurements for LGPS-type electrolytes using Li–Sn and Li–Si alloy electrodes.

Comparison of results for $Li_{9.75}Ge_{0.75}P_{2.25}S_{12}$, $Li_{10.05}Ge_{1.05}$-$P_{1.95}S_{12}$ and $Li_{10.5}Ge_{1.5}P_{1.5}S_{12}$ LGPS-type electrolytes (denoted $Li_{3.25}Ge_{0.25}P_{0.75}S_4$, $Li_{3.35}Ge_{0.35}P_{0.65}S_4$ and $Li_{3.5}Ge_{0.5}P_{0.5}S_4$ in the original paper) indicates that for the $Li_{9.75}Ge_{0.75}P_{2.25}S_{12}$ electrolyte with low germanium and high phosphorus content, there is only moderate increase in the resistance along with the cycle number. In contrast, high Ge-content, $Li_{10.5}Ge_{1.5}P_{1.5}S_{12}$, leads to an increase of the resistance of more than one order of magnitude within 20 cycles (Fig. 52).[135] Although not obtained for metallic lithium, but for Li–Si and Li–Sn alloy electrodes at potentials higher than those required for Li-, the results qualitatively demonstrate the pronounced influence of the specific stoichiometry of the phosphosulfide electrolytes.

Consequences on the state of the Li-metal-phosphosulfide interface other than the direct ones, that result in the build-up of an interlayer that is resistive to Li-ion conductivity, are detected, when combining analysis by spectroscopy with

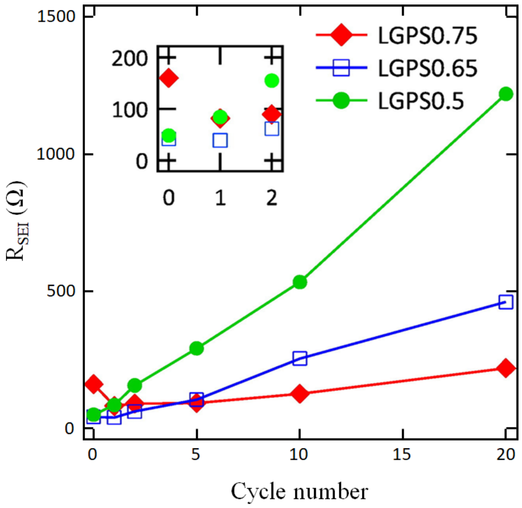

Fig. 52. Evolution of interphase resistance in $Li_{9.75}Ge_{0.75}P_{2.25}S_{12}$, $Li_{10.05}Ge_{1.05}P_{1.95}S_{12}$ and $Li_{10.5}Ge_{1.5}P_{1.5}S_{12}$ (denoted as $Li_{3.25}Ge_{0.25}P_{0.75}S_4$ – $LGPS_{0.75}$, $Li_{3.35}Ge_{0.35}P_{0.65}S_4$ – $LGPS_{0.65}$ and $Li_{3.5}Ge_{0.5}P_{0.5}S_4$ – $LGPS_{0.5}$ in the original paper) along with cycle number. Reprinted with permission from Sakuma *et al.* © 2016 Elsevier.[135]

microscopy or tomography.[133,134,136] The decomposition of the phosphosulfide electrolytes via reduction to Li_2S, Li_3P and lithium-halides or Li–Ge alloys imply a substantial volume expansion that may lead to cracks at the interface. The cracks will cause contact losses, lead to void formation on lithium deposition and result in inhomogeneous current distribution, which may give rise to the formation of zones with dead lithium and promote dendrite formation and growth, that can be considered indirect consequences of electrochemical instability. Thus, the design of an electrochemically stable interface is of utmost importance for long run stable operation of all solid-state batteries with Li-metal anode.

4.2.4. *Interface design approaches*

The interface resistance emerging from the formation of the interphase between Li-anodes and phosphosulfide electrolytes and the degradation of the battery performance manifesting in increasing overpotentials resulting from its eventual growth motivate intensive investigations in interphase formation and design. The objective of the research is to develop an interphase that is stable along with electrochemical cycling by providing additional interlayers or modifying the interlayer formation between Li-metal anode and phosphosulfide electrolyte to overcome these challenges.[137–139]

In order to promote low resistance and long-term stable battery operation, the interlayers between Li-metal and electrolytes have to be electrochemically stable vs. Li/Li^+, highly conductive for Li-ions, while at the same time being insulating with respect to electrons to avoid proceeding reduction reactions of the phosphosulfide electrolyte at the interface.[140] However, the interlayer has not only to account for these issues, but also to provide and maintain good contact between the electrolyte and the Li-metal anode, to ensure favorable conditions for deposition and dissolution of lithium during plating and stripping and to establish sufficient resistance against dendrite growth. Moreover, facile processing and the need to establish homogeneous layers along with scalability of the interlayer area have to be met for large-scale implementation in batteries. Many of the development approaches to design the interphase try to cover these issues simultaneously.

Considering the electrochemical stability issue, research is focusing on interphase layers built up by inorganic and polymeric Li-conductive electronical insulators and organic/inorganic composites, but also metallic coatings were subject to investigations. Insulators, inorganic Li-compounds, polymers and composites thereof are the materials of choice to establish suitable interlayers. Concepts for the design of the interlayers encompass, on the one hand, protective layers that are *a priori* stable with metallic lithium as well as with the phosphosulfide electrolyte. On the other hand, artificial SEI layers formed *in situ* by reaction of SEI forming agents with the surfaces of either the Li-metal anode or the phosphosulfide electrolyte are applied.[139]

(1) Interlayers of metals and metal alloys

In spite of high electronic conductivity, metal coatings of the electrolytes have been used as interlayers between Li-metal and phosphosulfide electrolytes. Although such layers have stabilizing effects when compared to designs with direct contact between Li-metal and phosphosulfide electrolytes, they do not meet the challenge of electrochemical stabilization of a Li-metal vs. phosphosulfide interface at Li/Li+ redox potential.[141,142] Upon cycling, alloying and eventually de-alloying between the metals and lithium is induced. While cycling in this stage, the plating and stripping of lithium takes place in or from the alloy which results in an increase of the anode potential and a decrease in battery voltage, so actually the cells do not have the characteristics of cells with Li-metal, but with alloy electrode. When saturated with lithium, as it occurs along with applying very thin metallic layers, the Li-alloy interphase is conductive. As the potential of a Li-electrode with Li-saturated alloy, interphase will rise back close to the Li-metal potential, the Li-ions at the electrolyte interface face almost the same conditions as in case of direct contact to metallic lithium.

(2) Coating by inert insulators

Al_2O_3 layers with 20 nm thickness on $Li_{10}SnP_2S_{12}$ were prepared by atomic layer deposition (ALD).[134] While the ALD coating improves cyclability compared to coating free $Li/Li_{10}SnP_2S_{12}/Li$ symmetric cells, *in-operando* XPS demonstrated, that upon cycling Li_xAl_yO was formed. Owing to the volume expansion of the interphase layer concomitant to this reaction, cracks in the interlayer appeared that give way to contact of the $Li_{10}SnP_2S_{12}$ to metallic lithium resulting in the reduction of the $Li_{10}SnP_2S_{12}$, as indicated by the presence of Li_2S close to the interface.[134] Organic interlayers, specifically plastic crystal electrolyte (PCE) based on succinonitrile (SN) with lithium bis(trifluoromethanesulfonyl) imide (LiTFSI) may also stabilize the Li-metal vs. phosphosulfide electrolyte interface. The chemical compatibility between SN-PCE and $Li_{10}SnP_2S_{12}$ was evidenced by Raman spectroscopy. Forming pellets by heating SN/LITFSI liquid-like solution and infiltrating in PCE in glass fiber network with subsequent assembly of Li/SN/$Li_{10}SnP_2S_{12}$/SN/Li symmetric cell demonstrated the cycling stability of this type of setup.[143] A modified version of this approach establishing an inorganic/organic composite layer by adding $LiNO_3$ to the SN provides stable protective interlayers as well.[143]

(3) In situ interphase layers — Artificial SEI

Recent approaches are mainly concerned with binary lithium compounds that are formed from precursors *in situ*. Thereby, stabilizing effects are in particular expected from Li-salts that are electrochemically stable vs. Li/Li^+ while at the same time being conductive for Li-ions and insulating for electrons. A survey of the stability windows and the conductivities for Li-ions and electrons of the Li-salts is summarized in Fig. 47.

All Li-halogen salts as well as Li_3N, Li_3P and LiO_2 are stable vs. metallic lithium.[114] Thus, these materials are used as the main components of the stabilizing interphase layers. Among them, LiF is the salt with the widest electrochemical window making it also suitable for implementing high voltage cathodes. Li_3N has the highest Li-ion conductivities up to 10^{-3} S/cm compared to other binary Li-compounds and quite low electronic conductivity.[144] Requirements to improve the contact between Li-metal or formation of by-products of the processing procedures in many of the approaches result in the presence of an additional polymeric component in the final interphase.

Following these lines, three different *in situ* approaches can be distinguished with respect to processing and reaction sequences.

(a) Application of interlayer precursors to Li-metal surface induces a reaction between the precursor and the Li-metal and forms the interlayer before the subsequent joining of electrode and electrolyte (Fig. 53(a)). A specific variant of this approach is a process, according to which the interlayer is formed from products that result from the electrochemical reduction of the liquid electrolyte in an electrochemical cell (Fig. 53(b)).

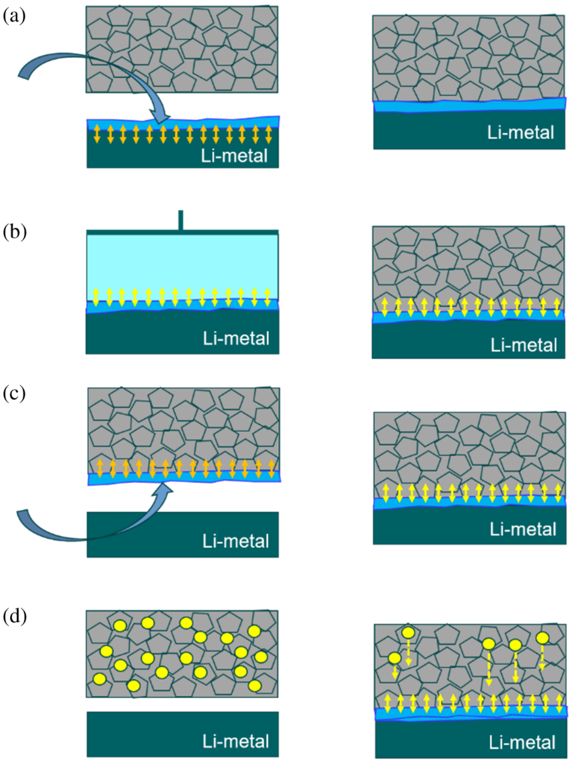

Fig. 53. Types of artificial *in situ* interphase layers. (a) Application of interlayer precursors to Li-metal surface. (b) Variant approach of electrochemical layer deposition from liquid electrolyte on lithium metal surface. (c) Deposition or infiltration of the interlayer precursors to the phosphosulfide electrolyte surface. (d) Modification of the phosphosulfide with subsequent reaction after joining the Li-metal electrode.

(b) Deposition or infiltration of the interlayer precursors to the phosphosulfide electrolyte surfaces results in a reaction between the interlayer precursor and the phosphosulfide in which the interlayer is formed followed by joining of electrode and electrolyte (Fig. 53(c)).

(c) Modification of the phosphosulfide with subsequent joining to the Li-metal electrode after which the reactions to form the final interlayer take place along with electrochemical cycling of the cell (Fig. 53(d)).

(3a) In situ interphase layers applied to Li-metal electrode

There are numerous approaches to design stabilizing interphase layers on Li-metal surfaces:

(i) *In situ* generation of binary halogen-salt layers on Li-foil via exposure of the lithium to evaporating iodine I_2 gas at 150°C/6 h results in 1.08 μm LiI film formation on the surface.[145] Applying a similar process using vapor from HFE, micron-scaled LiF films can be grown.[145] Both approaches provide interphase layers, which show enhanced cycling stability when cycled in symmetric cells with $Li_7P_3S_{11}$ glass ceramic electrolyte.

(ii) Following an ambient temperature process by spin coating H_2PO_4 in THF solution on the Li-metal surface results in a $LiHPO_4$ layer on the surface of Li-foil and improved cycling using $Li_{10}GeP_2S_{12}$ electrolyte.[127]

(iii) Li_2SiS_3 top layers on Li-metal surfaces can be implemented via a two-step process. Dip coating of Li-metal in Li_2S_8 dissolved in THF results in a uniform Li_2S_x layer. Subsequent addition of $SiCl_4$ and application to the Li-metal provides LiCl and Li_xSiS_y. Wash out of the LiCl using THF results in Li_xSiS_y layers that proved stable when cycling with Li_3PS_4.[146]

(iv) Composite layers including Li-salts can be established by decomposition of PTFE under pressure 150 MPa on metallic Li-surfaces. Partial defluorination reaction of PTFE establishes a three-component layer encompassing LiF, carbon particles and a C–F bond top layer.[147] The coated Li-anodes were stable upon cycling with $Li_{10}GeP_2S_{12}$ electrolyte.

(v) Polyacrylonitrile (PAN)/fluoroethylene-carbonate (FEC) dissolved in GBL (gamma-butyrolactone) applied by spin coating to Li-metal surfaces after drying at 60°C result in organic–inorganic composite layers of Li_3N, LiF embedded in an organic matrix with these components emerging from PAN, FEC and GBL reactions, respectively.[148] These coatings improve the cycling performance of symmetric cells with Li_6PS_5Cl electrolyte.

(vi) Interphase layers formed via electrochemical deposition of reduction products of 1M LiTFSI in dioxalane (DOL)/1,2-dioxymethane (DME) liquid electrolyte on Li-metal consist of organic/anorganic Li-salts as components. Specifically, the nanocomposite layers are built up by elastomeric organic Li-salt LiO-$(CH_2O)_2$-Li and inorganic LiF, -NSO_2-Li and Li_2O nanoparticles.[149] These layers applied on Li metal anodes efficiently stabilize the interface to $Li_{10}GeP_2S_{12}$ electrolyte and enable high cycle numbers with little increase in voltage.

(3b) In situ interphase layers generated on phosphosulfide electrolytes

The reaction conditions, sequence of the reactions and the products on formation of the interphase layers on the phosphosulfide electrolytes depend not only on the precursors used for the interlayer formation, but also on the specific phosphosulfide electrolyte. Via coating or infiltration of precursor solutions, such as ionic liquids, organic liquid electrolytes or polymers on or in the phosphosulfide electrolyte pellets, stable interphase layers can be formed along with contact of the ionic liquid (IL) with the electrolyte or by subsequent electrochemical cycling.

When applied to $Li_{10}SnP_2S_{12}$ surfaces LiTFSI/Pyr_{13}, LiF and CF_3 are identified as reaction and decomposition products of IL on $Li_{10}SnP_2S_{12}$ surface. Formation of a thin LiF layer occurs already in contact of IL with Li-metal, but cycling the layer is enhanced.[150]

In contrast, applying ionic liquid LiG(4)TFSI tetraethylen glycol dimethyl ether (G4), there is no reaction with Li_6PS_5Cl contact. In this process, the SEI consisting of components LiO-CH_2O_n-Li and Li_3N and LiF is formed via the electrochemical reduction of the Li(G4)TFSI electrolyte during cycling.[151] Organic electrolytes with Li-salt, specifically lithium bis(fluorosulfonyl)imide (LiFSI) dissolved in DME were also used for infiltration of phosphosulfide electrolytes to generate LiF coatings. After applying the LFSI/DME to Li_3PS_4 electrolyte and vacuum drying at 120°C, on contact with metallic lithium, a LiF-rich layer forms at the interface and provides stable cycling performance.[152]

(3c) Electrochemical in situ interphase layers by reacting modified phosphosulfide electrolytes

An alternative strategy to induce protective layers on contact to or cycling of the interface to metallic lithium is to modify the phosphosulfide electrolyte instead of applying precursor layers. Research work following this approach encompasses experiments with fluorinated and nitridated Argyrodites.[144,153] Fluorination of Cl-based Argyrodite electrolyte according to $Li_6PSCl_{0.3}F_{0.7}$ upon electrochemical cycling with metallic Li electrodes leads to an interphase with high LiF content in addition to Li_3PS_4 and Li_2S.[153] XPS depth profiling shows a gradient in the composition of the electrolyte according to which the presence of LiF is most pronounced close to the interface enabling highly stable cycling of symmetric Li/$Li_6PSCl_{0.3}F_{0.7}$/Li cells.

Among nitridated Argyrodites $Li_{6+x}PS_{5-x}N_xCl$, the composition with $x = 0.25$ proved most useful for the formation of a Li_3N-rich artificial SEI close to the Li-metal interface enabling long-term cycling of the electrolyte vs. metallic lithium.[144] The Li-ion conductivities are only slightly reduced by the fluorine and nitride modification of the Argyrodites. Moderately high Cl-doped Argyrodite $Li_{5.7}PSCl_{1.3}$ along with slow cooling after high temperature synthesis shows microstructures in which LiCl nanoparticles on the surfaces of the Argyrodite particles form an interconnecting LiCl framework. After cycling, from this network, a 55-μm LiCl interphase layer in the neighborhood of the Li-metal electrode is formed which substantially diminishes the degradation during cycling of Li/$Li_{5.7}PSCl_{1.3}$/Li symmetric cells.[154]

(4) Evaluation of interphase designs

Analytical tools to evaluate the electrochemical stability are in particular surface analyzing spectroscopy techniques XPS and Raman, which are sensitive enough to detect even small amounts of decomposition products. Ideal setups for the investigations of the interlayers are *in situ* XPS and *in-operando* XPS.[131,133,134] Electrochemical stability tests in the investigations are commonly evaluated by comparing the evolution of the overpotentials of symmetric Li/electrolyte/Li

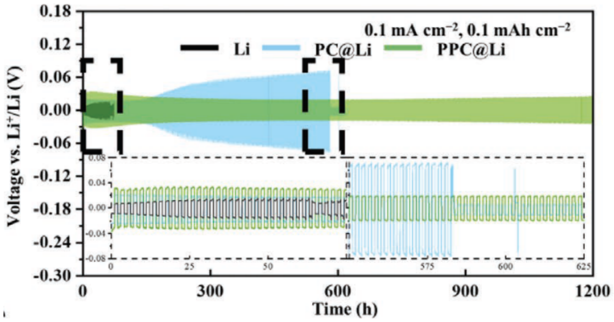

Fig. 54. Galvanostatic discharge/charge voltage profiles of Li/LPSC/Li (Li), PC @ Li/LPSC/PC @ Li (PC @ Li), and PPC @ Li/LPSC/PPC @ Li (PPC @ Li) symmetric cells with current densities of 0.1 mA cm^{-2} at room temperature. Reprinted with permission from Kato *et al*. © 2020 Wiley-VCH GmbH.[155]

cells with vs. without protective interlayer (Fig. 54). Thereby, cycling at relatively low currents, typically 0.1 mA/cm^2, is useful to detect electrochemical instabilities, as along with high current also other degradation mechanisms like dendrite growth may arise and cover the effects from interphase formation and growth.

The inter-experimental comparison between different electrolytes, however, has to consider also the contribution of the bulk electrolyte to the overpotentials which depends on the Li-ion conductivity of the electrolyte and the sample geometry. While for cycling of electrolytes with Li-conductivities higher than 5×10^{-3} S/cm at 0.1 mA/cm^2 using typical sample geometries, the impact of the bulk electrolyte resistance on the total overpotential is almost negligible, cycling at higher currents or using more resistive sample dimensions the effects have to be taken into account (Fig. 55).

In some approaches, deeper insight in the mechanisms was achieved from electrochemical impedance spectroscopy (EIS), following the evolution of the spectra with cycle numbers. State-of-the-art interfaces provide total overpotentials at 0.1 mA/cm^2 between 20 mV and 100 mV in symmetric cell setups.

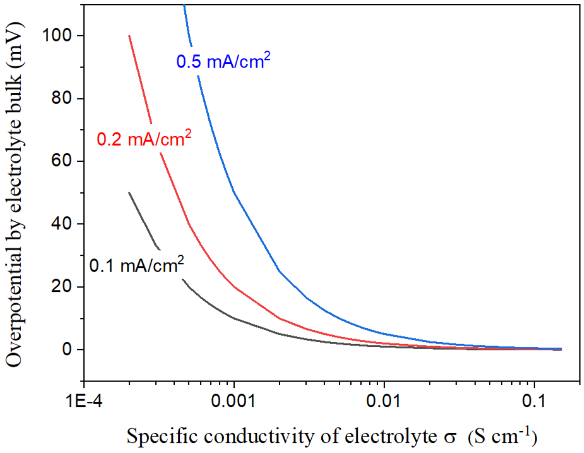

Fig. 55. Overpotentials resulting from electrolyte layer depending on the Li-ion conductivity of the electrolyte for current densities, of 0.1 mA/cm^2, 0.2 mA/cm^2 and 0.5 mA/cm^2.

5. Conclusions and Prospects

Part II of this review on phosphosulfides contains a thorough discussion of LGPS-type and Argyrodite-type electrolytes, before turning to an allover inter-type comparison of Li–P–S-type, LiSICon-type, LGPS-type and Argyrodite-type electrolytes with respect to Li-ion conductivity and electrochemical stability vs. metallic lithium. The current material development of the LGPS-type and Argyrodite-type phosphosulfides tends to explore a wide scope of substitution and doping partially replacing the characteristic elements used in the prototype materials, while maintaining the constitutive structural characteristics, space groups *P4$_2$/nmc* for LGPS-type and *F-43m* for Argyrodite-type electrolytes. Liquid-phase processes replacing the conventional solid-state processing routes are under investigation. Enhancement of Li-ion conductivities to a level surmounting 10^{-3} S/cm, while at the same time using resource efficient components underlines the successful research work on these electrolytes.

Based on the treatise on the Li–P–S type and the LiSICon type in part I, and the LGPS-type and the Argyrodite-type electrolytes in part II, where their chemistry, structure, processing and Li-ion conductivities were discussed in detail, an inter-type comparison with respect to two main features for the application of electrolytes in all solid-state batteries, the Li-ion conductivities and the electrochemical stability vs. metallic lithium, was addressed.

The primary objective of the research during the past decades, to synthesize materials with high Li-ion conductivities, has been largely achieved. In this first phase of the phosphosulfide electrolyte development, the focus was on high Li-ion conductivity and resulting in materials with high Li-transport performance based on resource efficient materials. High Li-ion conductivities are reported for materials within each of the phosphosulfide electrolyte types.

Li-ion conductivities of the thio-LiSICon Li-ion conductors $Li_{3.25}Ge_{0.25}P_{0.75}S_4$ (2.2 mS/cm) exceed 10^{-3} S/cm.[30] Materials surmounting the 10^{-2} S/cm threshold, reaching the conductivities of liquid electrolytes, can be found in the LGPS system: with Ge-based $Li_{10}GeP_2S_{12}$ (12 mS/cm)[7]; Si/Sn-based $Li_{10.35}Sn_{0.27}Si_{1.08}P_{1.65}S_{12}$ (11 mS/cm)[23]; Si-based chlorine co-doped $Li_{9.54}Si_{1.74}P_{1.44}S_{11.7}Cl_{0.3}$ (25.3 mS/cm at 90% pellet density and 14.0 mS/cm at 75% dense powder compact).[9] In the Argyrodite system, there are high Li-ion conductivities for high Cl-doped $Li_{5.5}PS_{4.5}Cl_{1.5}$ (10.2 mS/cm).[59] The Li-ion conductivity for Li–P–S-type $Li_7P_3S_{11}$ glass-ceramic amounts up to (17 mS/cm).[156]

In the past few years, the focus of research has shifted toward the investigations of the electrolytes with respect to electrochemical stability under operation conditions for batteries with Li-metallic anodes. The results of the studies concluded that along with contact to lithium metallic anodes the phosphosulfide electrolytes tend to decompose. Effects of decomposition products are substantially different for phosphosulfide electrolytes that contain semi/metal components vs. the semi/metal free and halogen-based phosphosulfides. While the decomposition products of the former ones are electronically conductive and form interphase layers tending to propagate into the electrolyte, the decomposition of the latter ones results in insulating layers at the interface, preventing further decomposition and leads to largely stable operation conditions.

While these issues were discussed in detail in the review, processing and engineering issues that will enable large-scale production and facile integration of the electrolytes in the cell environment and the batteries emerge as the upcoming topics for future research and development work.[16,138,157–167] Thereby, while phosphosulfide electrolytes seem to be a viable approach for the realization of all solid-state lithium ion batteries with metallic lithium anodes, they have to compete in particular with polymer-ceramic hybrid electrolyte ASSB design.[168–175]

Key challenges for the phosphosulfide electrolytes, therefore, will be the development of liquid-phase processing that makes them appropriate for fabrication of thin electrolyte layers and coatings, techniques for the cell assembly that provide stable mechanical interfaces, contact and favorable deposition conditions for lithium on charging, and processing approaches that enable handling of the phosphosulfides by reducing their sensitivity to oxygen and moisture making phosphosulfide processing and battery assembly suitable for mass production framework.

Acknowledgment

Support for the work was provided by the project "High Performance Solid-State Batteries" (HIPSTER) from the "Ministerium für Kultur und Wissenschaft des Landes Nordrhein-Westfalen" which is gratefully acknowledged.

References

1. M. Tachez *et al.*, *Solid State Ion.* **14**, 181 (1984).
2. R. Mercier *et al.*, *J. Solid State Chem.* **43**, 151 (1982).
3. J. F. Brice, *C R Acad. Sci. C Chim.* **283**, 581 (1976).
4. H. Y. P. Hong, *Mater. Res. Bull.* **13**, 117 (1978).
5. P. G. Bruce and A. R. West, *Mater. Res. Bull.* **15**, 379 (1980).
6. H. J. Deiseroth *et al.*, *Angew. Chem. Int. Ed.* **47**, 755 (2008).
7. N. Kamaya *et al.*, *Nat. Mater.* **10**, 682 (2011).
8. K. Homma *et al.*, *Solid State Ion.* **182**, 53 (2011).
9. Y. Kato *et al.*, *Nat. Energy*, **1**, 16030 (2016).
10. S. T. Kong *et al.*, *Chem.-Eur. J.* **16**, 5138 (2010).
11. J. H. Wu *et al.*, *Adv. Mater.* **33**, 2000751 (2021)
12. Q. Zhang *et al.*, *Adv. Mater.* **31**, 1901131 (2019).
13. T. Yu *et al.*, *Mater. Chem. Front.* **5**, 4892 (2021).
14. O. U. Kudu *et al.*, *J. Power Sources* **407**, 31 (2018).
15. J. Xu *et al.*, *Mater Today Nano* **8**, 100048 (2019).
16. A. Miura *et al.*, *Nat. Rev. Chem.* **3**, 189 (2019).
17. Y. Kato *et al.*, *Adv. Energy Mater.* **10**, 2002153 (2020).
18. O. Kwon *et al.*, *J. Mater. Chem. A* **3**, 438 (2015).
19. S. Hori *et al.*, *J. Am. Ceram. Soc.* **98**, 3352 (2015).
20. P. Bron *et al.*, *J. Am. Chem. Soc.* **135**, 15694 (2013).
21. S. Hori *et al.*, *Faraday Discuss.* **176**, 83 (2014).
22. Y. Kato *et al.*, *J. Power Sources* **271**, 60 (2014).
23. Y. L. Sun *et al.*, *Chem. Mater.* **29**, 5858 (2017).
24. M. Murayama *et al.*, *Solid State Ion.* **170**, 173 (2004).
25. Y. L. Sun *et al.*, *J. Power Sources* **324**, 798 (2016).
26. S. Hori *et al.*, *Front Energy Res.* **4**, 38 (2016).
27. K. H. Kim and S. W. Martin, *Chem. Mater.* **31**, 3984 (2019).
28. K. Suzuki *et al.*, *Solid State Ion.* **288**, 229 (2016).
29. M. Xu *et al.*, *Solid State Ion.* **356**, 115458 (2020).
30. R. Kanno and M. Maruyama, *J. Electrochem. Soc.* **148**, A742 (2001).
31. A. Kuhn *et al.*, *Energ Environ. Sci.*, **6**, 3548 (2013).
32. Y. Bai *et al.*, *ACS Sustain. Chem. Eng.* **7**, 12930 (2019).
33. Z. Jiang *et al.*, *ACS Appl. Mater. Interfaces* **13**, 30739 (2021).
34. S. B. Song *et al.*, *Chem. Mater.* **34**, 8237 (2022).
35. Y. X. Li *et al.*, *Chem. Mater.* **32**, 8860 (2020).
36. M. Xu *et al.*, *Inorg. Chem.* **61**, 52 (2022)
37. J. Hassoun *et al.*, *J. Power Sources* **229**, 117 (2013).
38. S. Hori *et al.*, *Acta Crystallogr. B* **71**, 727 (2015).
39. Y. M. Wang *et al.*, *J. Power Sources* **224**, 225 (2013).
40. S. P. Ong *et al.*, *Energy Environ. Sci.* **6**, 148 (2013).
41. R. Kanno *et al.*, *Solid State Ion.* **130**, 97 (2000).
42. Q. Zhang *et al.*, *Mater. Lett.* **248**, 153 (2019).
43. J. G. Yi *et al.*, *ACS Appl. Mater. Interfaces* **11**, 36774 (2019).
44. W. Z. Huang *et al.*, *J. Solid State Chem.* **270**, 487 (2019).
45. H. Eckert *et al.*, *Chem. Mater.* **2**, 273 (1990).
46. H. M. Chen *et al.*, *Phys. Chem. Chem. Phys.* **17**, 16494 (2015).
47. P. Bron *et al.*, *J. Power Sources* **352**, 127 (2017).
48. D. A. Weber *et al.*, *Chem. Mater.* **28**, 5905 (2016).
49. Y. Fei *et al.*, *IOP Conf. Ser.: Mater. Sci. Eng.* **394**, 022038 (2018).
50. A. Kuhn *et al.*, *Phys. Chem. Chem. Phys.* **16**, 14669 (2014).
51. L. D. Zhou *et al.*, *ACS Energy Lett*. **4**, 265 (2019).
52. Z. Y. Zhu *et al.*, *Chem. Mater.* **29**, 2474 (2017).
53. A. W. Eissenbach, *Neues Jahrb. Geol. Paläontol*. **2**, 67 (1886).
54. I. Hanghofer *et al.*, *Phys. Chem. Chem. Phys.* **21**, 8489 (2019).
55. M. A. Kraft *et al.*, *J. Am. Chem. Soc.* **139**, 10909 (2017).
56. H. J. Deiseroth *et al.*, *Z. Anorg. Allg. Chem.* **637**, 1287 (2011).
57. P. Adeli *et al.*, *Angew. Chem. Int. Ed.* **58**, 8681 (2019).
58. C. Yu *et al.*, *Nano Energy* **69**, 104396 (2020).
59. W. D. Jung *et al.*, *Nano Lett*. **20**, 2303 (2020).
60. M. A. Kraft *et al.*, *J. Am. Chem. Soc.* **140**, 16330 (2018).
61. N. Minafra *et al.*, *J. Mater. Chem. A* **6**, 645 (2018).
62. S. Ohno *et al.*, *Chem. Mater.* **31**, 4936 (2019).
63. Y. Inoue *et al.*, *J. Solid State Chem.* **246**, 334 (2017).
64. Z. T. Liu *et al.*, *Inorg. Chem.* **59**, 226 (2020).
65. Z. R. Zhang *et al.*, *J. Mater. Chem. A* **7**, 2717 (2019).
66. H. Schneider *et al.*, *J. Power Sources* **366**, 151 (2017).

67. I. Seo and S. W. Martin, *Acta Mater.* **59**, 1839 (2011).
68. H. Schneider *et al.*, *ChemistrySelect* **4**, 3351 (2019).
69. I. Hanghofer *et al.*, *Chem. Mater.* **31**, 4591 (2019).
70. C. Yu *et al.*, *ACS Appl. Mater. Interfaces* **10**, 33296 (2018).
71. A. Gautam *et al.*, *Chem. Mater.* **31**, 10178 (2019).
72. A. Gautam *et al.*, *Adv. Energy Mater.* **11**, 2003369 (2021).
73. S. Yubuchi *et al.*, *ACS Appl. Energy Mater.* **1**, 3622 (2018).
74. S. Choi *et al.*, *J. Electrochem. Soc.* **166**, A5193 (2018).
75. S. Chida *et al.*, *Ceram. Int.* **44**, 742 (2018).
76. N. J. J. de Klerk *et al.*, *Chem. Mater.* **28**, 7955 (2016).
77. N. Minafra *et al.*, *Inorg. Chem.* **59**, 11009 (2020).
78. B. J. Morgan, *Chem. Mater.* **33**, 2004 (2021).
79. Z. X. Zhang *et al.*, *J. Alloy. Compd.* **747**, 227 (2018).
80. P. R. Rayavarapu *et al.*, *J. Solid State Electrochem.* **16**, 1807 (2012).
81. W. Arnold *et al.*, *J. Power Sources* **464**, 228158 (2020).
82. R. P. Rao *et al.*, *Chem. Mater.* **31**, 8649 (2019).
83. M. Brinek *et al.*, *Chem. Mater.* **32**, 4754 (2020).
84. C. Yu *et al.*, *J. Mater. Chem. A* **7**, 10412 (2019).
85. S. Boulineau *et al.*, *Solid State Ion.* **221**, 1 (2012).
86. R. P. Rao and S. Adams, *Phys. Status Solidi A* **208**, 1804 (2011).
87. S. Yubuchi *et al.*, *J. Mater. Chem. A* **7**, 558 (2019).
88. H. Wang *et al.*, *J. Power Sources* **412**, 29 (2019).
89. S. Ohno *et al.*, *ACS Energy Lett.* **5**, 910 (2020).
90. Y. Wang *et al.*, *Nat. Mater.* **14**, 1026 (2015).
91. T. Krauskopf *et al.*, *Chem. Mater.* **30**, 1791 (2018).
92. S. Adams and R. P. Rao, *J. Mater. Chem*. **22**, 7687 (2012).
93. M. Aniya and K. Wakamura, *Physica B* **219–220**, 463 (1996).
94. K. Wakamura, *Phys. Rev. B* **56**, 11593 (1997).
95. J. C. Bachman *et al.*, *Chem. Rev.* **116**, 140 (2016).
96. S. Muy *et al.*, *Energy Environ. Sci.* **11**, 850 (2018).
97. L. Kahle *et al.*, *Phys. Rev. Mater.* **2**, 065405 (2018).
98. X. Lu *et al.*, *Funct. Mater. Lett.* **15**, 26 (2022).
99. R. Paul and V. Thangadurai, *Ionics* **27**, 4917 (2021).
100. D. P. Almond and A. R. West, *Solid State Ion.* **23**, 27 (1987).
101. N. H. H. Phuc *et al.*, *Solid State Ion.* **288**, 240 (2016).
102. M. Murayama *et al.*, *J. Solid State Chem.* **168**, 140 (2002).
103. Y. H. Xiao *et al.*, *Nat. Rev. Mater.* **5**, 105 (2020).
104. T. Binninger *et al.*, *J. Mater. Chem. A* **8**, 1347 (2020).
105. Y. F. Mo *et al.*, *Chem. Mater.* **24**, 15 (2012).
106. H. Park *et al.*, *ACS Energy Lett.* **6**, 150 (2021).
107. Y. Z. Zhu *et al.*, *Adv. Sci.* **4**, 1600517 (2017).
108. Y. Z. Zhu *et al.*, *ACS Appl. Mater. Interfaces* **7**, 23685 (2015).
109. F. D. Han *et al.*, *Adv. Energy Mater.* **6**, 1501590 (2016).
110. T. K. Schwietert *et al.*, *Nat. Mater.* **19**, 428 (2020).
111. W. D. Richards *et al.*, *Chem. Mater.* **28**, 266 (2016).
112. A. Banerjee *et al.*, *Chem. Rev.* **120**, 6878 (2020).
113. D. H. S. Tan *et al.*, *ACS Energy Lett.* **4**, 2418 (2019).
114. Y. Z. Zhu *et al.*, *J. Mater. Chem. A* **4**, 3253 (2016).
115. N. D. Lepley *et al.*, *Phys. Rev. B* **88**, 104103 (2013).
116. B. B. Chen *et al.*, *Phys. Chem. Chem. Phys.* **19**, 31436 (2017).
117. L. E. Camacho-Forero and P. B. Balbuena, *J. Power Sources* **396**, 782 (2018).
118. A. Golov and J. Carrasco, *ACS Appl. Mater. Interfaces* **13**, 43734 (2021).
119. T. Cheng *et al.*, *ACS Energy Lett*. **2**, 1454 (2017).
120. J. X. Huang *et al.*, *J. Chem. Phys.* **154**, 094703 (2021).
121. A. Marcolongo *et al.*, *ChemSystemsChem* **2**, e1900031 (2020).
122. C. G. Staacke *et al.*, *Nanomaterials (Basel)* **12**, 2950 (2022).
123. Y. Q. Shao *et al.*, *Batteries Supercaps* **4**, 585 (2021).
124. S. Wenzel *et al.*, *Solid State Ion.* **278**, 98 (2015).
125. S. Wenzel *et al.*, *Solid State Ion.* **286**, 24 (2016).
126. C. Yu *et al.*, *Energy Storage Mater.* **30**, 238 (2020).
127. Z. H. Zhang *et al.*, *ACS Appl. Mater. Interfaces* **10**, 2556 (2018).
128. G. F. Dewald *et al.*, *Chem. Mater.* **31**, 8328 (2019).
129. T. Swamy *et al.*, *Chem. Mater.* **31**, 707 (2019).
130. L. Z. Sang *et al.*, *Chem. Mater.* **29**, 3029 (2017).
131. S. Wenzel *et al.*, *Chem. Mater.* **28**, 2400 (2016).
132. S. Wenzel *et al.*, *Solid State Ion.* **318**, 102 (2018).
133. A. L. Davis *et al.*, *J. Electrochem. Soc.* **168**, 070557 (2021).
134. A. L. Davis *et al.*, *J. Mater. Chem. A* **8**, 6291 (2020).
135. M. Sakuma *et al.*, *Solid State Ion.* **285**, 101 (2016).
136. J. A. Lewis *et al.*, *Nat. Mater.* **20**, 503 (2021).
137. P. Oh *et al.*, *Angew. Chem. Int. Ed.* **61**, e202201249 (2022).
138. C. H. Wang *et al.*, *Energy Environ. Sci.* **14**, 2577 (2021).
139. Y. H. Liang *et al.*, *InfoMat* **4**, e12292 (2022).
140. S. M. Li *et al.*, *Nano Energy* **102**, 107640 (2022).
141. A. Kato *et al.*, *Solid State Ion.* **322**, 1 (2018).
142. L. Z. Sang *et al.*, *Chem. Mater.* **30**, 8747 (2018).
143. C. H. Wang *et al.*, *Adv. Funct. Mater.* **29**, 1900392 (2019).
144. Y. Liu *et al.*, *J. Mater. Chem. A* **9**, 13531 (2021).
145. R. C. Xu *et al.*, *Nano Energy* **53**, 958 (2018).
146. J. W. Liang *et al.*, *Adv. Energy Mater.* **9**, 1902125 (2019).
147. L. Shen *et al.*, *Adv. Mater. Interfaces* **9**, 2200822 (2022).
148. C. Wang *et al.*, *Adv. Mater. Interfaces* **8**, 2001698 (2021).
149. Y. Gao *et al.*, *Angew. Chem. Int. Ed.* **57**, 13608 (2018).
150. B. Z. Zheng *et al.*, *ACS Appl. Mater. Interfaces* **10**, 25473 (2018).
151. C. F. Zou *et al.*, *ACS Appl. Energy Mater*. **5**, 8428 (2022).
152. X. L. Fan *et al.*, *Sci. Adv.* **4**, eaau9245 (2018).
153. F. P. Zhao *et al.*, *ACS Energy Lett.* **5**, 1035 (2020).
154. D. W. Zeng *et al.*, *Nat. Commun.* **13**, 1909 (2022).
155. Y. Chen *et al.*, *Adv. Energy Mater.* **11**, 2002545 (2021).
156. Y. Seino *et al.*, *Energy Environ. Sci.* **7**, 627 (2014).
157. X. Lu *et al.*, *Electrochem. Sci. Adv.* e2100208 (2022), https://doi.org/10.1002/elsa.202100208
158. T. Ates *et al.*, *Energy Storage Mater.* **17**, 204 (2019).
159. T. A. Yersak *et al.*, *J. Electrochem. Soc.* **166**, A1535 (2019).
160. M. Ghidiu *et al.*, *J. Mater. Chem. A* **7**, 17735 (2019).
161. D. H. Kim *et al.*, *Nano Lett.* **17**, 3013 (2017).
162. S. J. Choi *et al.*, *ACS Appl. Mater. Interfaces* **10**, 31404 (2018).
163. A. Banik *et al.*, *Chem. Sci.* **12**, 6238 (2021).
164. J. Schnell *et al.*, *J. Power Sources* **382**, 160 (2018).
165. Y. Nikodimos *et al.*, *Energy Environ. Sci.* **15**, 991 (2022).
166. X. G. Miao *et al.*, *Energy Environ. Sci.* **13**, 3780 (2020).
167. Y. T. Chen *et al.*, *J. Mater. Chem. A* **10**, 7155 (2022).
168. M. Keller *et al.*, *J. Power Sources* **392**, 206 (2018).
169. L. Chen *et al.*, *Nano Energy* **46**, 176 (2018).
170. Y. F. Zhai *et al.*, *Adv. Mater.* **34**, 2205560 (2022).
171. L. Zhang *et al.*, *ChemElectroChem* **9**, e202200641 (2022).
172. M. R. Li *et al.*, *ACS Sustain. Chem. Eng.* **9**, 11314 (2021).
173. M. Wirtz *et al.*, *Electrochem. Sci. Adv.* **1**, e2000029 (2021).
174. Y. R. Zhao *et al.*, *J. Power Sources* **301**, 47 (2016).
175. K. Fu *et al.*, *Proc. Natl. Acad. Sci. USA* **113**, 7094 (2016).